UNIVERSITÀ DEGLI STUDI DI TRIESTE

XXX CICLO DEL DOTTORATO DI RICERCA IN NANOTECNOLOGIE

Tuning cellular functionality and mechanobiology via carbon nanotubes based scaffolds

Settore scientifico-disciplinare: BIO/09

DOTTORANDA
Ilaria, Carmela Rago

COORDINATORE
PROF. Lucia Pasquato

SUPERVISORE DI TESI
Dr. Denis Scaini

CO-SUPERVISORE DI TESI
Dr. Loredana Casalis

ANNO ACCADEMICO 2016/2017

Abstract

Natural tissue self-regeneration, occurring at the onset of injury or disease through the self-organization of cells into organs/tissues, is strongly impaired by mechanical and biochemical cues from the damaged extracellular environment, which finally impact cell fate. In order to drive tissue self-renewal ability, artificial biomaterials mimicking the complex architecture of the physiological cell microenvironment are highly desired. The natural extracellular matrix (ECM), however, is a highly dynamic 3D structure which displays an intricate network of nanoscale structures, whose morphology adapts to cell input, providing in turn mechanical cues to the surrounding cells which activate the biochemical and mechano-transduction pathways necessary for the modulation of their functions. Since cells normally interact with typical nanometer-scale elements present in their environment, nanoscale features are the first essential requirement for the design of biomimetic scaffolds. In this context, it is not surprising that carbon nanotubes (CNTs), owning various similarities with the native ECM in terms of micro- and nano-morphology, physico-chemical and mechanical properties, have captured increased attention. Various works have been carried out to study the interaction between CNTs and different cell types such as cardiomyocytes and neurons, supporting their use as scaffolds to promote cellular growth and development. CNTs unequivocally demonstrated their ability to perturb/potentiate electrical activity of neuronal cells cultured on them, assuming a potential role in neuroscience. In previous studies, cell cultures were grown on purified, commercial multi-walled carbon nanotubes (MWCNTs) deposited on supporting surfaces via drop casting or mechanical entrapment techniques, highlighting the effect of CNTs on modulating cellular behavior. Here, for the first time, we demonstrate that CNTs directly grown on a supporting silicon surface by catalytic chemical vapor deposition (CCVD) technique bear the same potentiating effect, with the added value of easy modulation of the CNT matrix properties. In our approach we developed a novel and well-controllable synthesis method leading to the realization of various CNTs-based architectures which could be employed as-produced, without the necessity of any chemical purification or functionalization in liquid-phase, thus significantly simplifying their use. We prove that primary dissociated neuronal cells from rat hippocampus, cultured on such CNTs mat, develop a healthy and functional network and, moreover, that the resulting neuronal network shows a potentiated electrical activity when compared to a control network developed on flat glass surfaces. Additionally, the high versatility of our synthesis method enables the realization of patterned

CNTs featuring potentially any arbitrary shape, useful to drive cell growth in specific directions, and otherwise extremely difficult to fabricate with the other available approaches.

In order to further exploit the potential of our CNTs mats as artificial biomaterial for tissue regeneration, experimental results from complementary techniques are required. Our CNTs substrates grown on silicon surfaces, however, lack of optical transparency, primarily due to the opacity of silicon wafers. This prevents the exploitation/use of such nanostructured substrates with all the investigation techniques requiring to optically visualize cells 'through' the specimens as, for example, electrophysiology and bright field microscopy. To this aim, we developed a novel strategy to fabricate transparent carbon nanotubes substrates (tCNTs) by synthesizing these carbon nanostructure via CCVD directly on a transparent substrate (i.e. fused silica) and finely controlling their length in order to maintain such value not larger than 10-15 times the wavelength of visible light. We demonstrated that this original fabrication "recipe" gives rise to CNT carpet able to induce the same synaptic potentiation in hippocampal cells we observed in the case of opaque CNT films and drop-casted layers. We further investigated the ability of tCNTs to support the growth of complex neuronal tissues as intact and lesioned Entorhinal-Hippocampal slice cultures (EHCs). In lesioned EHCs cultures, tCNTs have revealed their unusual ability to significantly increase the signal synchronization and fiber sprouting between the cortex and the hippocampus with respect to glass controls. Accordingly, we demonstrated for the first time that our nanomaterial can help in promoting a successful reconnection and functional cross talk between the two slices after the lesion.

CNTs-based scaffolds can be exploited not only to instruct the organization and functionality of neural networks, but also to improve the standard strategies adopted for the treatments of cardiovascular diseases (CVD) which currently do not lead to a long-term solution. In this context, the employment of functional engineered scaffolds able to restore heart functionality may represent a promising strategy to overcome such limitations. In particular, our interest has been directed towards calcific aortic valve diseases (CAVD), strongly related to significant changes in ECM organization, composition and mechanical properties. Therefore, based on the crucial role that ECM properties have on the progression of this disease and considering also the peculiar CNTs ability to structurally emulate the native ECM, we interfaced our novel tCNTs scaffold with porcine valve interstitial cells (pVICs), the predominant constituent of aortic valve, governing ECM structure and composition, in both physiological and pathological conditions. By exploiting the optical transparency of tCNT

substrates, we had the chance, for the first time, to simultaneously perform an immunofluorescence assay, in order to characterize VICs morphology and phenotype, and AFM force spectroscopy analysis, to determine the stiffness of pVICs cultured onto these carbon-based substrates. Starting from the previously reported hypothesis that the ECM morphology could affect the pro-pathologic variation in pVICs (from fibroblasts to myofibroblasts) occurring at the onset of the CAVD, we evaluated if and how our nanomaterial, mimicking the real ECM, influences the morphology and phenotype of the pVICs. Overall, we demonstrated that tCNTs substrates can provide a physiological environment for VICs development in which the amount of myofibroblasts is similar to that characterizing healthy valves. However, bi-dimensional (2D) culture systems fail in reproducing the complex and dynamic environment of native tissues. To overcome this limit three-dimensional (3D) scaffolds have to be developed and used as matrices providing, in this way, structural, chemical and signaling cues closer to the natural ECM. We realized various 3D bio-constructs made of different materials, including carbon nanotubes (i.e. CNTs-decorated iron foam) and polymers (i.e. porous polydimethylsiloxane (PDMS) scaffolds) in order to investigate material/cell interaction and biological responses in a three-dimensional frame.

1. Engineered bio(nano)-scaffolds might tune Cell Behavior and Tissue Engineering

2. Carbon Nanotubes: structure, properties and synthesis

3. Experimental

4. Results and Discussion

1. Engineered bio(nano)-scaffolds might tune Cell Behavior and Tissue Engineering

1.1 Introduction

The self-organization of cells into organs and complex tissues during the natural tissue regeneration following tissue damage or lost is highly regulated by mechanical and biochemical events determining cell behavior and destiny [1]. In particular, cells, due to their exceptional capability to convert mechanical stimuli into biochemical signals and *vice versa*, direct this natural reorganization process. In this framework, the extracellular matrix (ECM) plays a key role by providing the bioactive cues required to modulate cellular functions and interactions [2]. Natural tissue regeneration capabilities can be altered by external chemical factors, diseases and aging [3], thus necessitating an external and artificial help by medical devices. Among them, biomaterials have been used since antiquity to restore, maintain or improve defective tissues functions [4]. In ancient times, natural materials selected based on availability, such as wood, were employed in this context as pointed out by the naïve example in Figure 1.

Figure 1. Prosthetic to replace an amputated toe derived from natural wood (1065–740 bc circa) identified in an anthropological excavation of the Thebes West tombs, Egypt. (Image courtesy of J. Finch, KNH Centre for Biomedical Egyptology, University of Manchester, UK, and The Egyptian Museum, Cairo) (Image from [4]).

In the early 20th century, these biomaterials were complemented by synthetic polymers, ceramics and metal alloys gaining a better efficacy as prosthetic devices (i.e. artificial hips, vascular stents, dental restoratives). However, all the initial efforts with such novel materials were put in guaranteeing the same inertness of biomaterials, required to avoid the biological rejection from the host organism, paying almost no attention at providing sufficient bioactive cues to tune host cell properties and functions, necessary for tissue engineering [5]. In

particular, such artificial scaffolds were initially designed to mimic the replacing part at a macroscopic level, totally disregarding the nanoscale elements present in native tissues. The extra-cellular matrix (ECM), which is surrounding cells in the human body and governing their behavior, shows in fact a natural and intricate network of nanoscale structures; consequently, cells normally interact with typical nanometer-scale elements present in their environment. For that reason, nanoscale features are crucial in the attempt to realize artificial bio-instructive scaffolds characterized by regenerative ability through a biomimetic design that emulates the natural components of the human body. To this aim, the fundamental basic principles of how cells and tissues are organized and work as hierarchical ensemble from nano-to macroscopic length scale must first be understood. This requires an understanding of the ECM constituents produced by cells, as well as their organization into a functional and structural three-dimensional meshwork.

1.2 Key ECM constituents

A tissue consists not only of cells, but also of a complex and intricate network of macromolecules assembled to constitute the extracellular matrix [6], a highly heterogenic three-dimensional structure characterized by a cell/tissue-dependent composition surrounding and supporting cells within tissues. ECM is mainly composed of water, proteins and polysaccharides linked together to form a structurally organized matrix in close and continuous communication with cells [2]. Initially, ECM was considered to have just a structural role, but today it is well known its key role in cell signaling and tissue morphogenesis, differentiation and homeostasis. Moreover, variations in ECM composition, together with how specific ECM macromolecules are assembled, determine cell phenotype specificity and localization depending on the functional requirements of each particular tissue. For instance, in the case of the hard structures of bone or teeth the ECM is calcified, while in the case of the cornea it forms a transparent matrix. Such tissue specificity is given by an active and incessant communication between various cells inside each tissue (e.g. epithelial, fibroblast, endothelial elements) and the surrounding microenvironment. ECM comprises an intricate array of extracellular macromolecules classified as *glycosaminoglycans* (GAGs), unbranched polysaccharide chains consisting of repeating disaccharide units, usually attached to a protein core in the form of *proteoglycans* (PGs) and fibrous proteins of two functional types: structural (i.e. collagen and elastin) and adhesive (i.e. fibronectin and laminin) [7]. Among the fibrous proteins the most abundant in mammals (about 30% of the total protein

mass) is *collagen*, existing in over 25 types [8]. It plays a structural role inside the ECM environment by influencing the architecture and mechanical properties of the tissues as the tensile strength in skin and resistance to traction in ligaments. The hierarchical organization of collagen fibers composing molecules (about 300 nm in length and 1.5 nm in diameter), fibrils (20-100 nm in diameter) and fibers (0.5-20 μm in diameter) leads cells to sense collagen environment through different length scale.

Elastin, another structural protein generally present in "stretchable" tissues such as skin, bladder and blood vessel, provides tissues deformation and recoil capabilities in response to a mechanical stretch. This elastic function is crucially related to that of collagen fibers which, as described before, offer rigidity and tensile strength.

Beside collagen and elastin, PGs are also key players in ECM biomechanics. PGs biological function here derives from the biochemical ability of GAG components to sequester water and growth factors, thereby acting as a sort of hydrated gel in the extracellular interstitial space capable of providing hydration and compressive resistance. Therefore, glycosaminoglycan and proteoglycan are assembled to form an extremely hydrated gel in which fibrous proteins are embedded; while such gel-based structure provides compressive resistance to the matrix, the collagen fibers contributes to its tensile strength. Thanks to the remarkable hydration of the ECM gel-like network a rapid diffusion of nutrients, hormones and metabolites between blood and tissue is permitted [9]. Collagen and proteoglycans are the major structural constituents within the ECM offering a biomechanical scaffold where other ECM elements and cells can interact. Such structural molecules are linked to each other through additional ECM glycoproteins, such as *laminin* or *fibronectin* (also known as adhesive proteins), thus reinforcing this complex and creating an intricate extracellular network within which ECM is connected to cells and to soluble factors.

These adhesive proteins are involved not only in the organization of the interstitial ECM, but also in the regulation of cell adhesion, migration and differentiation. For instance, in connective tissues, fibronectin helps the attachment of fibroblasts and other cell types to the ECM, instead laminin supports the adhesion of epithelial cells to the basal lamina, separating the epithelium from the underlying layers of connective and muscle tissues.

1.3 Role of the ECM in mechanobiology

As discussed above, the ECM is not simply an ensemble of proteins, but it significantly influences cell behavior and tissue development by performing tissue-specific functions through its constituents and its organization that are unique for each tissue. Various signaling transduction pathways, dictated by the biochemical and biophysical properties of the ECM, are followed by cells to interact with the extracellular environment. A large body of research suggests that cells exert traction forces thanks to their interactions with the ECM, inducing, in turn, variations in cell morphology and related signaling cascades that, in turn, influence gene expression and ultimately cell functions (e.g., cell migration, differentiation, proliferation, and apoptosis) [10]. The ability of cells to sense and react to various ECM features, including the composition, mechanical stiffness, and topology, is mediated by *integrins*: cell membrane receptors connecting ECM proteins to the cell cytoskeleton [9-10]. Integrins behave like free diffusive elements within the cell membrane until they recognize an available binding domain in the ECM (e.g., laminins, collagens, fibronectin). At this point, integrins start to bind to ECM proteins and physically cluster together leading to the association with two types of cytoplasmic proteins: (i) those responsible of the biomechanical connection between the integrins and the cytoskeleton (e.g. talin) and (ii) those that biochemically give rise to intracellular signaling pathways (e.g. vinculin). Such association with various intracellular proteins generates a focal complex that growing leads to the formation of nanoscale (<200 nm), disc-shaped, protein complexes called *focal adhesions* (FA) that offer a physical and biochemical link to transduce mechano-chemical cues from the ECM to the cell (and *vice-a-versa*), thereby influencing cell properties (i.e. migration, proliferation and differentiation). FA can be considered as sensors of the ECM environment thanks to their ability to sense both mechanical and biochemical changes within the ECM. Although integrin binding to ECM is crucial for signaling, it is not sufficient. In fact, integrins clustering and the development of mechanical tension, are both mandatory conditions for the maturation of focal complexes into larger complexes, such as focal adhesions, and for the subsequent induction of intracellular signaling. Therefore, beside the biochemical composition of the ECM, the formation of FA and the subsequent cellular response appears strongly determined by the mechanical properties of ECM and by the mechanical forces transmitted through it in many cell types [11].

Another structural component that must be taken into account in this context is the intracellular *cytoskeleton*. It is a natural web of protein filaments by which cells preserve their shape and mechanical properties (i.e. strenght) [12]. The three protein filaments constituting the *cytoskeleton* (i.e. actin, microtubules and intermediate filaments) can be considered as semi-flexible polymers, contributing to cell stiffness and resistance to compression forces [13]. In response to mechanical stimuli, the network made of actin and intermediate filaments potentiate its stiffness, inducing cells to increase the rigidity of their actin cytoskeleton when interfaced with stiff substrates via myosin motors-induced contraction [14].Focal adhesions as well as cytoskeleton are highly dynamic structures; processes of polymerization and de-polymerization of the actin filaments determine changes in cytoskeleton configuration and FA positioning in the cellular membrane, thus enabling cells to exert forces, change shape and react to external stimuli [15]. Finally, the nucleus has recently emerged as an important element of cell mechanosensing, due to its intimate contact with the cytoskeleton via the LINC complex [15]. Mechanical stimuli can not only modify the binding of proteins in FA, but also induce the formation of stress fibers in the cell which ultimately can induce nuclear ion channels opening, thus permitting the translocation into the nucleus of mechanosensitive transcription factors, as YAP (yes-associated protein), which provoke changes in cell morphology (Figure 2).

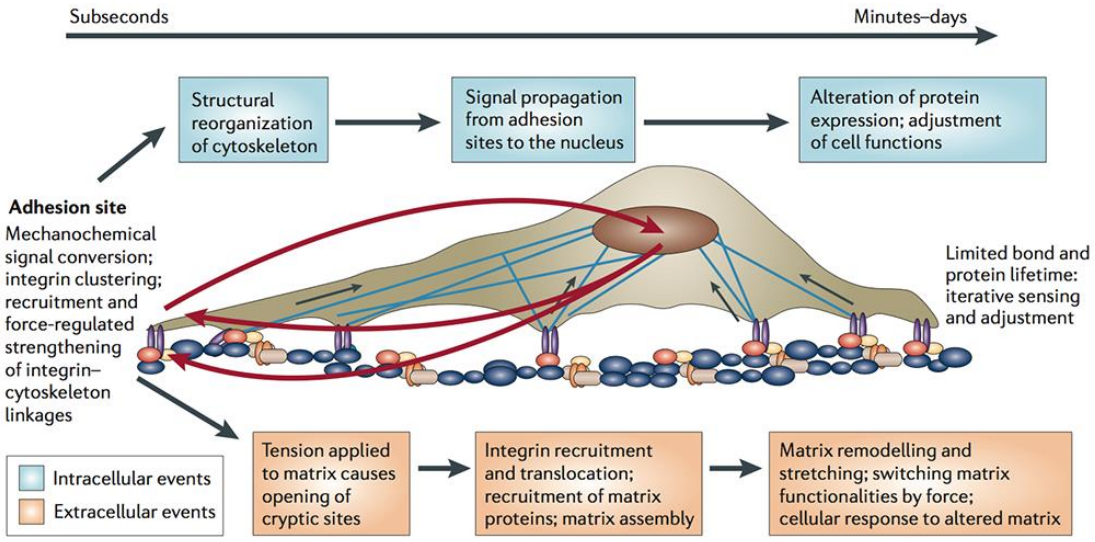

Figure 2 Cellular processes of mechanosensing and responses. Initially cells sense physical and mechanical properties of their environment, then the ECM undergoes modification and new intracellular signals are generated which in turn alter cells expression pattern and, over time, the cellular forces and shape. During any stage, extracellular signals (i.e. hormones or external mechanical stimuli) can provoke significant modifications that will lead to further ECM and cells variations. (Image from [16]).

The process, through which mechanical forces acting on the cell membrane are translated in cytoskeleton rearrangement and in conformational changes of adhesion sites integrin complexes, involves signaling pathways and gene expression and is called *mechanotransduction*. Summarizing, matrix stiffness influences the integrin clustering and a downstream signaling is sent to activate cell mechano-response. In this way, a bidirectional interaction takes palace: the ECM exerts mechanical action on the cell through integrins and, in turn, the cell reacts modulating its cytoskeleton arrangement, to resist to the external force. The stiffness of materials is often measured in terms of Young's modulus (E) and expressed in units of Pascal (Pa). In the human body are present soft and hard tissues characterized by elastic moduli ranging from hundreds of Pa (e.g., the brain nervous tissue) to GPa (e.g., skeletal bones) as pointed out in Figure 3. Cells sense and react to ECM mechanical stiffness mainly via the above described mechanotransduction for the regulation of cell behaviors, disease development, and embryonic morphogenesis.

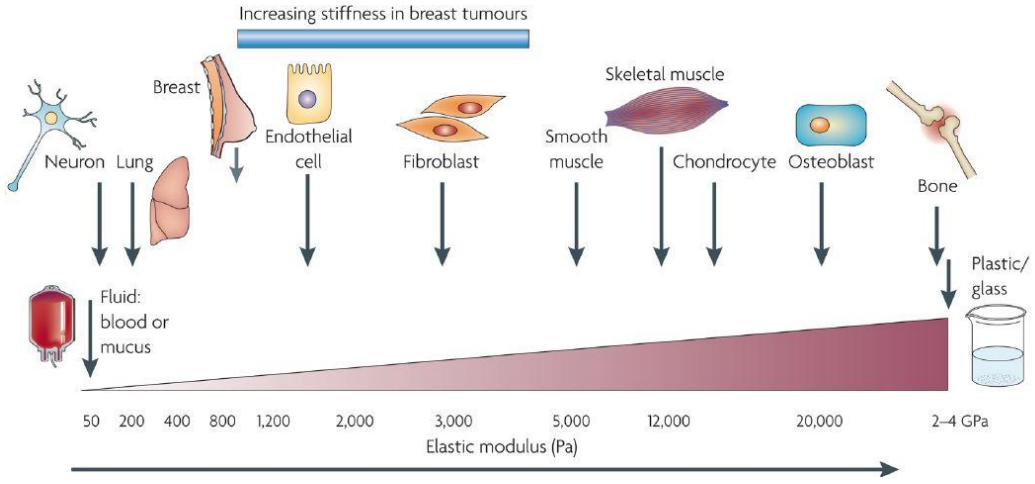

Figure 3 Cellular elasticity range in the human body (Image from [17]).

Abnormal variation in ECM stiffness contributes to the progression of various diseases, such as cancer [17]. In fact, it is reported that cancer tissues can be up to 10-fold stiffer than healthy tissues. This is primarily due to collagen deposition and proteins crosslinking within the tumor tissue leading, through mechanotransduction pathways, to phenotypic changes in cells determining in turn an increase in their proliferation and migration rate. In this perspective, mechanical properties of the surrounding ECM critically influence cellular behavior and therefore tissue growth, homeostasis and healing.

1.4 Micro- and nano-topography provide structural basis for the adjustment of cell properties

Beside biochemical and biomechanical cues, ECM also provides topographic stimuli primarily from the reach micro- and nanometer-scale elements (see paragraph 1.2) present in the matrix which mediate cell-matrix signaling. Contact guidance, a naturally occurring phenomenon by which cells interact with these native ECM topographical structures, assumes a crucial role in regulating cell behavior, such as adhesion, morphology, migration and differentiation [18]. Moreover, cells sense and react to the different length scales (from the nano- to the microscale) of ECM physical stimuli in a different manner [19]. At the nano level, ECM topography influences forces involved in cytoskeletal formation and directs the arrangement of cell adhesion molecule receptors, thus affecting the intracellular signaling [20]. At the microscale, ECM affects cellular (and supra-cellular) characteristics such as cell morphology, migration and tissue organization. However, it is still not completely clear how the physical environment of cells can perturb their behavior. In order to understand these interactions, micro and nano- fabrication techniques have been exploited to realize substrate with a desired micro- and/or nano-topography. In doing so, various studies have demonstrated the important influence of topographical features in terms of size, shape, and geometric constrains on cell responses, including adhesion, migration, alignment, and differentiation [21]. Among the aforementioned features, the size of topographical elements (e.g., width, spacing and depth of features) was found to be an essential player in modulating cell properties in a cell type-dependent manner, as verified for several cell types [22].

.

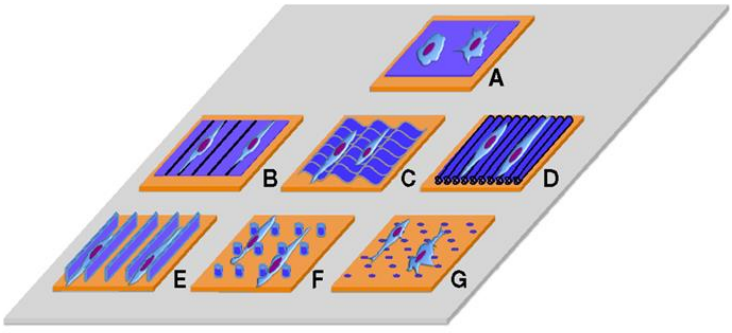

Figure 4. Traditional surfaces used to culture cells on 2D without/with nano/micro topographic cues. (A) Flat surface, (B) contact guidance lines, (C) grooves, (D) aligned fibers, (E) 2D confined environments, (F) nano/micro pillars (G) nano/micro pits (Image from [23]).

Additionally, nanotopography turned out as a crucial element in the adjustment of cell adhesion which in turn is vital for the subsequent cell growth and proliferation on a substrate. It has been reported that nanofibrous substrates regulate the expression of integrins, promoting cell adhesions, more efficiently than flat substrates [24]. From the comparison between cells grown on grooved surfaces featuring pitches of 400−1200 nm and > 1600 nm, respectively, it was found that smaller pitches (400−1200 nm) lead to higher adhesive interactions, both with respect to larger pitches (>1600 nm) and to flat surfaces [25]. Interestingly, a critical size range in which cell properties are significantly improved was found. In fact, it has been observed that cells cultured on substrates characterized by a spacing width of the adhesive ligands (cyclic RGD (arginine–glycine–aspatate) peptides) below 60 nm, displayed a more pronounced adhesive behaviors than cells grown on substrates with larger spacing width (74 or 120 nm). This critical size, while being strongly related to the cell type, substrate material and topography, seems in fact to strictly match the dimensions of cellular sensing elements as the integrins clusters [26]. Moreover, since many biological interfaces and tissues are characterized by a hierarchical organization from nano- to micrometric scale, it is clear that both scale sizes, nano and micro, are fundamental in regulating their structure and functions. As a consequence, a synergistic combination of nano and microscale topography has to be preferentially adopted for the growth of various cell types in order to gain better performances in guiding cell properties [27]. As an example, it was demonstrated that bi-scale topographic cues (micrograting substrates with nanofibrous matrices deposited on top of them) in the scaffold positively influence endothelial cells behavior in terms of elongation, shaping and spreading as compared to unpatterned nanofibers [28]. In the case of neuronal cells, for instance, it was reported that complex geometries characterized by a combination of microwells (~18 μm in diameter) connected by grooves (~5 μm width) on nanofiber mats (~440 nm in diameter) determined an improvement in cell attachment, confinement and neurite growth [29]. Accordingly, hierarchical structures including both micro- and nanoscale patterns, have been used as powerful tools/cues to regulate many cell process starting from the adhesion and up to longer time processes such as differentiation [30] and subtype specification [31]. Such evidences regarding the strategic role of topographical size could be exploited for designing smart materials for tissue engineering and regenerative medicine applications.

1.5 Engineering the ECM through nanotechnology to obtain a desirable scaffold

As described above, a key player in tissue regeneration is the ECM that, by providing fundamental biochemical and biophysical cues, induces a cascade of events associated to each other which are decisive for cell fate and tissue development. That is why biocompatible materials possessing appropriate mechanical, chemical and biological properties are employed to re-create the natural environment in which such events (i.e. opportune cellular adhesion, migration, proliferation, cell growth and functions) can occur, thus promoting tissue regeneration and/or functional restoration. In this framework, a critical step is the design of suitable scaffolds tuned to mimic as close as possible the complex extracellular and physiological environment of the tissue areas where they are programmed to be place: thus to generate proper habitat in which cell performances are identical or similar to native tissues before injury. The scaffold must be biocompatible, and could be biodegradable and bio-absorbable or not, if any inflammatory or adverse effect is induced. In order to mimic the natural organic ECM, it is indispensable that the scaffold shows high porosity, great surface–volume ratio, and significant degree of interconnection between the pores as well as appropriate pore size and geometry. Importantly, it must also provide physical and mechanical support to guarantee proper cell organization and cell-to-cell interaction, even with the synthetized ECM. The scaffold, characterized by the aforementioned peculiarities, could be implanted and colonized by cells into the tissue to be repaired or alternatively it might be seeded with cells realizing an *in vitro* culture in order to obtain a regenerated tissue before implantation.

In the last decade, nanostructured materials received increased attention thanks to their similarities with the natural ECM assuming an intriguing potential in regenerative medicine and tissue engineering application [32-33]. At the nanoscale, their large surface area to volume ratio, leads to outstanding physical, chemical and mechanical properties which enable the possibility to control and influence cellular behaviors [34]. By taking into account not only nanomaterial peculiar properties, but also simply the fact that cells in their natural environment interact with several nanoscale elements, it is not surprising that nanostructured materials are considered as a breakthrough for the development of tissue engineered scaffolds able to interact at the subcellular level [35]. Among them, nanofibers can be adopted as potential bio-scaffolds thanks to their highly interconnected porous geometry that promote cell colonization combined with the right exchange of nutrients and metabolic waste between

scaffold and the external environment. In the perspective to realize scaffolds resembling the ECM features, 3D nanofibrous-based structures represent potential candidate. Nanofibers can be produced starting from synthetic and natural materials (or, alternatively, a combination of them) and with different techniques: *phase separation*, *self-assembly*, *electrospinning*, *bacterial cellulose*, *templating*, *drawing*, *extraction*, *vapour-phase polymerization* and other techniques, which are described in a comprehensive review [36]. As an example, a 3D sponge-like structure is obtained by employing phase separation method. The most common material adopted in this case is the synthetic poly (L-lactic acid) (PLLA), at times combined with collagen [37]. It was reported that the resulting scaffold is characterized by a high degree of porosity which can be suitable to promote cell migration and nutrient supply as well as the removal of metabolic wastes throughout the scaffold. Remarkably, this 3D-scaffold presents a nanometric structure similar to that of natural ECM. However, although the phase separation process is an easy and low cost method, it does not permit the control of micro- and nano-fibers orientation, a parameter that has been shown to be crucial in regulating cell shape and functions [37].

Electrospinning is the most widely adopted procedure for the production of micro- and nano-fiber decorated surfaces or three-dimensional scaffolds. It consists of a relatively simple fabrication process characterized by a great versatility of the adopted material combined with the possibility to control scaffold geometry (i.e. fibers orientation) [38]. Briefly, an electrostatic field was exploited to produce fibers of modifiable diameter [39] from both synthetic (i.e. ploycaprolactone, PLLA) and natural polymers, such as collagen, forcing them to flow through a calibrated ejection nozzle. The electrospinning set-up is usually characterized by: (i) a capillary through which a high voltage is applied to the polymer solution to be "electrospun"; (ii) a high-voltage source which transfer charge to the liquid; (iii) a grounded collector (Figure 5). The resulting scaffold consists of closely packed nanofibers showing fibers diameters ranging from few nanometers to few micrometers. In one of the many studies conducted on electrospun scaffolds, for example, it was demonstrated that aligned PLLA/collagen-I/collagen-III nanofibrous scaffolds (average diameter of aligned fibers 253 ± 102 nm) better promote neurites elongation and directional outgrowth, following fiber direction, in neuronal cell lines developed above it, when compared to randomly oriented nanofibrous scaffolds [40]. Therefore, they highlighted the central role of both orientation and composition, influencing in turn mechanical stiffness, in engineering a suitable scaffold for peripheral nerve regeneration. Although the important advantages,

electrospinning technique presents various drawbacks, such as inefficient cellular infiltration, possible toxicity from chemical residues, inadequate mechanical strength for load-bearing applications, slow production rate, to mention some [36].

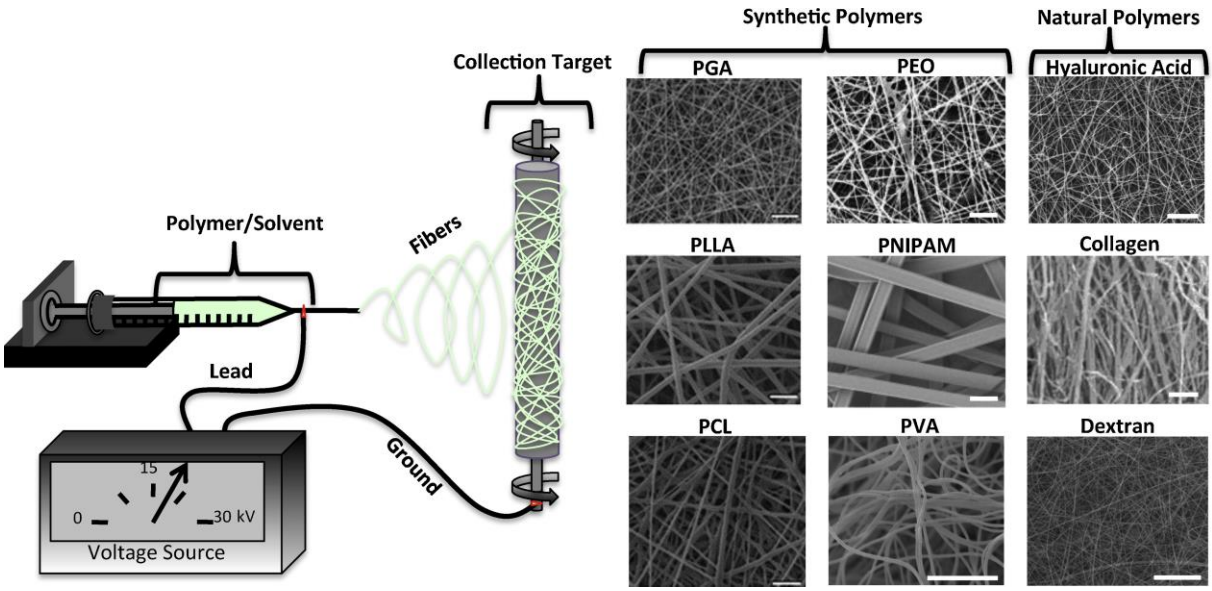

Figure 5. Schematic illustration of the electrospinning setup and SEM images of fibers from different synthetic and natural polymers produced by electrospinning. Scale bar: 10 µm. A syringe is filled with a polymer solution that is then placed on a syringe pump and connected with a blunt needle. An electric field is applied between the needle tip and the grounded collector by a high voltage supply. The solution is then "electrospun" consistently and stretched into fibers. The fibers are obtained from the grounded collector (Image from [41]).

It is worth recalling that an essential requirement for a tissue-engineering scaffold is that it must emulate as much as possible the native ECM, thus offering a (temporary) substitute capable of supporting cells during the development of new endogenous ECM. None of the aforementioned methods (i.e. phase separation, self-assembly, electrospinning, etc.) represents, singularly, the best strategy to realize the ideal ECM-mimicking scaffold. Therefore, in order to better emulate the 'natural' structure and composition of ECM –thus favoring, through the plasma membrane, cell-matrix interactions– such methods are often combined to exploit all the required characteristics for a specific tissue construct [42-43].As an example, Gelain and colleagues have reported a combination of electrospinning and self-assembly techniques to attach self-assembled peptides (SAPeptides) onto fibrous scaffold (randomly-oriented fibers characterized by a diameter ranging from 200 to 1000 nm) made of poly-(e-caprolactone) (PCL)- poly(lactic-co-glycolic acid)(PLGA) demonstrating an exceptional adhesion and viability of neural stem cell (NSC) [44]. Moreover, in order to better

mimic the natural ECM, a long motif of laminin, CQIK (CQAASIKVAV) was added [45]. Such laminin-based fibrous construct has led to a high viability of neuroblastoma cells, suggesting a promising application of this scaffold for the recovery of spinal cord injury with an increased neurogenesis and a decreased astrogliosis.

1.6 Carbon nanotubes: general properties and similarities with ECM

Within the class of nanofibers, carbon nanotubes (CNTs) represent a promising option in the perspective to create a reliable approach to tune cell properties. CNTs in fact show outstanding mechanical and electrical properties, on which I will focus in the next chapter. Here, I would like to anticipate that CNTs possess various similarities with the native ECM in terms of micro- and nano-morphology: both will in short appear fundamental attributes in the present context.

Briefly, CNTs can be thought as sheets of graphite rolled into seamless cylindrical tubes. They can be classified into: single-walled carbon nanotubes (SWNTs) and multi-walled carbon nanotubes (MWNTs) depending on the number of graphite sheets constituting their walls. While MWNTs have diameters ranging from few to hundreds of nanometers, SWNT diameters range between 0.8 to 2 nm. Both of them show outstanding mechanical properties (i.e. elastic modulus and tensile strength) and very high electrical and thermal conductivities. These peculiar properties are strongly related to their structure, and in particular to their ordered and flexible hexagonal network of carbon atoms linked via strong sp^2 bonds [46-47]. Besides nanotubes' flexibility and elasticity, also the high degree of porosity characterizing CNT agglomerations [48] is comparable with that of endogenous ECM [49], posing them as suitable materials to be adopted as cellular scaffold components. Another important CNTs peculiarity, apart from their fractal-like organization mimicking natural ECM morphology, is represented by their very large exposed surface area, increasing their effectiveness in interacting with biological tissues, and the final surface roughness, when decorating a surface, similar to the one characterizing a portion of native collagen fibers of the ECM. All these peculiar characteristics allow them to impressively affect cell adhesion, proliferation and differentiation [50].

However, several studies reported free-floating CNTs possible toxicity for living organisms owing to their asbestos-like pathogenicity aside from a not bio-friendly semblance [51-53]. It is worth pointing out here that a different effect on biological sample was observed for CNTs

immobilized on a substrate respect to the unbound form (e.g. a CNTs-based liquid suspensions or aerosol). In the case of neural network, no toxic effect was detected on both primary and organotypic cultures if CNTs were deposited/attached to an underlying substrate [54-55]. A completely different situation compared to CNTs suspensions that have provoked asbestos-like pathologies, such as granulomas, DNA damage, altered expression of inflammatory genes, oxidative stress and atherosclerotic lesions [53]. It was reported that their size or the impurities such as metallic and, in general, synthetic residual could determine CNTs toxicity [56]. Such possible reasons of CNTs negative effect on cell survival were confirmed when a significant reduction of CNTs toxicity was observed, as a result of an appropriate CNT purification, functionalization or adequate size selection [57-58]. Indeed, CNTs may be functionalized with various functional groups making them soluble in aqueous solution and organic solvents, and more easily to handle. In addition, the possibility to functionalize CNTs can modify some of their properties and functions [59], thus generating novel and promising therapeutic strategies [55].

With the final purpose to emulate as much as possible the native ECM, CNTs can be decorated also with carbohydrate molecules [60] or peptides [61]. Moreover, it was also reported CNTs ability to interact with ECM macromolecules promoting, in this way, natural cellular functions in damaged tissues [62]. In fact, effective ECM proteins recruitment favors the formation of tight and intimate contacts between CNTs and cell membranes. This reflects in correct cell adhesion, proliferation and differentiation resulting, at the end, in a cellular organization closer to the one observed in native tissues [63]. Since collagen is the most abundant ECM proteins, and based on the fact that cells present specific protein receptors on their membranes, Tosun and McFetridge, in 2010, started to employ collagen as support matrix. In particular, it was reported that a hybrid construct, based on CNTs embedded in a collagen gel, is effectively capable of promoting cells adhesion on scaffold surface, supporting them in a correct 3D environment in which they can proliferate and start the differentiation process. Despite the risk of toxicity connected to CNTs leak from the collagen framework, this combination represents a powerful strategy, not only because it emulates the 3D organization of ECM, but also because exploited collagen biocompatibility and biodegradability [64], opening to the use of these scaffolds as potential regeneration materials able to restore tissue structure and functionality. Moreover, in another experimental model, it was revealed the ability of such bio-hybrid system (CNTs/collagen) to “encourage” hydroxyapatite deposition that can be exploited in bone-fracture regeneration field [65]. As to

be noted that fibronectin, when immobilized on CNTs network, has promoted a great adhesion and proliferation rate of stem cells over the scaffold, thus highlighting again the key role of the interaction between ECM proteins and CNTs on cell physiological functions [66].

1.7 A brief overview of neural network and basic principles of neurotransmission

Among all tissues where three-dimensional scaffolds were exploited for regenerative purposes, the nervous system is, of course, the most challenging. The nervous system is a complex network of billions of specialized cells called *neurons* capable of controlling and regulating many aspects of body homeostasis such as blood pressure and pH, temperature, respiratory and sleep/wake cycle [67]. Moreover, it has a prominent role in directing our perception and experience of the world as well as our personality, learning, memory and voluntary movement. The nervous system can be divided into the *central nervous system* (CNS), made up of the brain and spinal cord, and the *peripheral nervous system* (PNS), composed by the cranial and spinal sensory and motor systems. An efficient communication between neurons is essential for the normal functioning of these two parts constituting the entire nervous systems. One tenth of the entire nervous system consists of neuronal cells (excitable cells) while the remaining cells are mainly neuroglial cells (having a supportive role). Within the CNS more than 100 billion neurons can be found which physically and functionally interact with each other via dendrites and axons.

Neuronal cells are characterized by three parts: the central *cell body* (or *soma*), in which most of the cell biosynthetic processes arise; the *dendrites* and the *axon*, carrying the electrical signals to and away from the cell body, respectively (Figure 6). In particular, the cell body represents the substantial part of a neuron with a diameter ranging between 5 to 100 μm; it is constituted by its nucleus, cytoplasm, neuronal membrane and cytoskeleton. Most of the metabolic activity of the neuron is conducted in the cell body thanks to its ability to maintain neuron cytoplasmic volume and to provide all necessary proteins. Such activity is detectable in the organelles within the soma cytoplasm: ribosomes and rough endoplasmic reticulum which are involved in the synthesis of proteins and a large number of mitochondria, essential for various cellular processes (i.e. ATP production, intracellular Ca^{2+} signaling and generation of reactive oxygen species). The cytoskeleton shows a high concentration of intermediate filaments wrapped together giving rise to the so-called *neurofibrils* which offer a structural support to the cell up to dendrites and axon; in addition, in the cytoskeleton are present also

microtubules that act not only as structural support but also as tools for transporting chemicals between soma and axon.

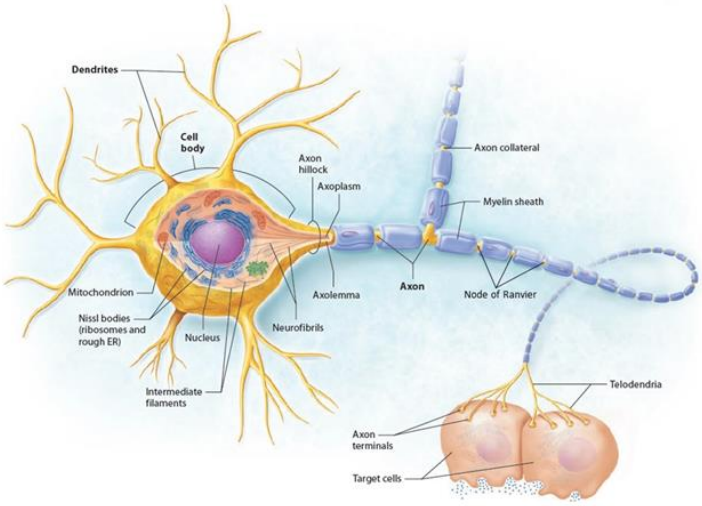

Figure 6. Typical neuron structure (Image from [67]).

The dendrites act as receptor sites for information sent from other neurons. Therefore, once received input from other neurons, transmit such signals as electrical impulses toward the soma. In their cytoplasm are present the same organelles of the cell body (i.e. mitochondria, ribosomes, and smooth endoplasmic reticulum). Due to the presence of dendrites, neurons possess a remarkable surface area. Notably, during the individual's lifetime they undergo a structural change consisting of a sort of "pruning" of the branches.

A neuron may have various branched dendrites, but usually presents only one axon **(**also called a *nerve fiber*), a specialized extension from the soma that carries the signal, generally, away from the cell body; however, there exist also neurons in which the axons can transport a signal both toward and away from the cell body. In this perspective, they can be described as processes capable of generating and conduit action potentials. Each axon originates in a zone of the soma known as *axon hillock* and, depending on the type of neuron, presents length ranging from few hundred of micrometers in some nerve cells (i.e. hippocampal neurons), to over a meter in others (i.e. motoneurons). The axon is capable of conducting action potentials at high speed and for long distances. Therefore, the insulating myelin sheet, which often encloses axons, is essential to avoid loss of information in terms of ionic currents. Along the axon, such myelin sheath is not continuous and the zones of discontinuity are called *Nodes of Ranvier*. It is important to highlight that neurons are capable of creating links with many other

neurons within the CNS, thus creating connections (referred as *synapses*) with other neuronal cells bodies or processes but also with non-neuronal cells such as receptors or muscles. In summary, signal transmission causes a chain reaction starting from the soma: if the dendrites receive an appropriate input from one or more neighboring neuronal cells, the neuron resting electrical membrane potential changes giving rise, due to the selective opening of specific ion channels, to an electrical signal which propagates along the axon. This *depolarization* wave is defined as *action potential* (for a detailed description about signal propagation in neurons refer to [68].

To better understand signal transmission mechanism in neurons, it is important to stress that while electrical signals in modern electronics rely on electron currents, neural currents are characterized by ionic physical displacement within the two sides of neuronal membranes and that, in this framework, neural membrane properties and channels represent a key element. Firstly, its hydrophobicity does not allow ion flows through it; however, the perfect synergy between *leak* and *gated* channels generates an ion concentration gradient. In particular, the first type of channel (leak) is always open thus enabling ions to move in accordance with their concentration gradient into or out of the cell. On the other hand, gated channels open only if receive precise stimuli and can be classified in: *ligand-*, *voltage-* and *mechanically-gated* channels if the stimulus is: a chemical bonding to the channel, a change in voltage across the membrane or a mechanical trigger (i.e. stretch, pressure, and vibration), respectively. The most important ions in this context are potassium, sodium, chlorine and calcium. ATP-consuming K+/Na+ pumps maintain the concentration gradients of sodium and potassium ions across the plasma membrane (high concentration of K^+ inside the cell and a high concentration of Na^+ ions outside the cells membrane). Such gradients determine a diffusion of potassium ions out of the cell while sodium ions tend to flow into the cell. Variations of these relative diffusion rates provoke changes in membrane potential (electrical gradient across the cell membrane). As mentioned above, an excited neuron transfers information to other neurons through the generation of signals (action potentials) which travel along neuron's axon and are transformed to chemical signals in presence of synapses. When the cell is at rest (not being stimulated), its external membrane is characterized by an electrical potential difference of about –70 mV (the inner surface is negative respect to the outer surface). In such condition, the membrane permeability to potassium ions is higher than that related to sodium ions; on the other hand, the permeability to sodium increases if the neuron is excited, provoking an influx of positive charges that in turn determine a temporary

inversion of the membrane potential (Figure 7). The transient phase is called *depolarization*. After about 1 ms the sodium permeability decays leading to an increase in potassium conductance (*repolarisation* phase) and finally the value of the resting membrane potential is restored (–70 mV).

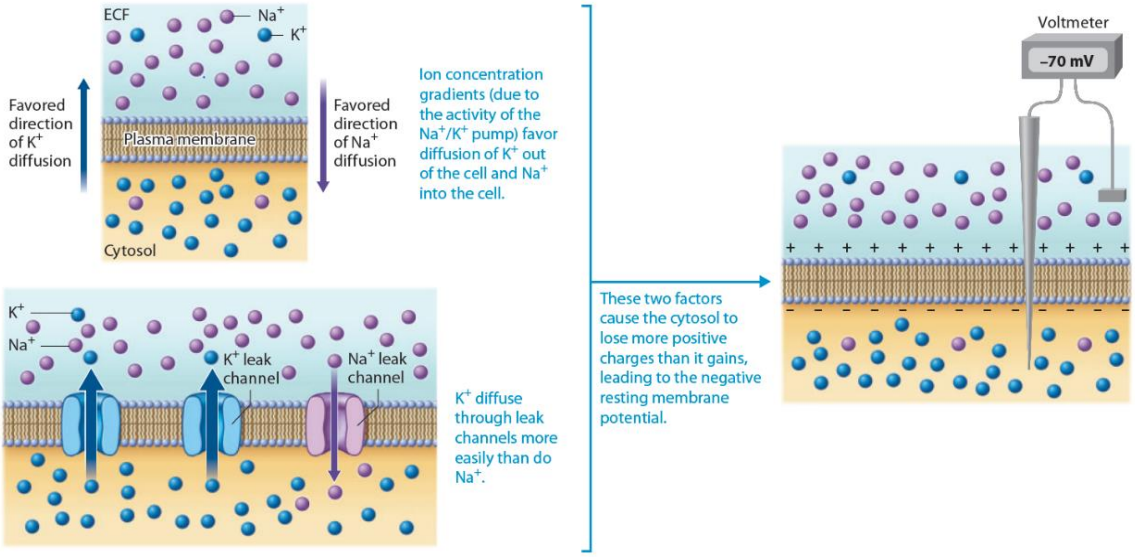

Figure 7. Generation of the resting membrane potential (Image from [67])

But how electrical signals are transmitted between neurons? Beside 100 billion neurons present in human brain, there are also 100.000 billion *synapses*. Most synapses connect the axon of one cell to the soma or dendrites of a second one. When neurons transmit information towards synapses are *presynaptic*; on the other hand, those conducting signals away are *postsynaptic*, each of which shows several synaptic connections on its dendrites or cell body.

Synapses can be classified in electrical and chemical. In the first type, signal transmission takes place via the ion flow through gap junctions, linking pre- and post-synaptic cells cytoplasm. Across such electrical synapsis, the information is transmitted very quickly. In chemical synapses, conversely, neuro-transmitters act as a chemical mediator of the electrical information between neurons. The trigger for the initialization of synaptic transmission is a nervous action potential reaching the presynaptic portion of the synapse. This event causes the depolarization of the presynaptic membrane and the consequent opening of voltage gated Ca^{2+} channels, thus enabling Ca^{2+} ions flow into the axon cytosol. Such process is followed by neurotransmitter vesicle releasing into the synaptic cleft, which divides the transmitting

(presynaptic) cell from the receiving (postsynaptic) one. Released neurotransmitters, binding to specific membrane receptors on the postsynaptic portion of the synapse, generate a slight depolarization (excitatory synapses) or a slight hyperpolarization obtained by Na^+ and/or K^+ ion channels. As mentioned above, the electrical synapses are faster than the chemical ones, but latter allow for integration of signals and plastic phenomena.

1.7.1 Nanotechnology and neuroscience

In order to functionally engineer the complex brain network, a better understanding of brain cells signaling in physiological and pathological conditions becomes crucial. Such knowledge will be translated, then, into novel prosthetic implants for brain repair. Although various challenges must still be overcome to finely understand neuro-machine, it is clear the lack of self-repairing in *central nervous system* (CNS). The ideal strategies adopted in the perspective to repair CNS should make possible various processes, such as the re-growth of injured axons, plastic neural circuit reorganization and neurogenesis by employing the potential of stem cell [69]. In this scenario, in which neural regeneration strategies and tissue engineering appear strongly related, synthetic nanomaterials can be engineered to offer biocompatible and bioactive scaffolding structures capable of promoting neural development. They have received a profound interest as (bio)scaffolds for neural applications, thanks to their dimensions comparable with many elements of neurons, glial cells and ECM as well as their capability to offer an ECM-like environment, to interact with neuronal membranes at the nanoscale and to favor neural adhesion [34]. Although various studies reported that both micro- and nano-patterns influence cellular functions (see paragraph 1.4), in the case of neural network interfaced with scaffolding structures, their interactions occur mainly at the nanoscale [34]. Moreover, another important aspect to highlight is that neurons prefer to adhere on substrates characterized by a dimensionality matching the dimensions of neuronal cytoskeletal components, as in the case of CNTs carpets [70]. Therefore, nanomaterials might provide new amazing clinical perspective in this field by offering suitable bio-chemical and bio-physical platforms supporting and promoting neural regeneration [71].

It is not surprising that CNTs, thanks to their impressive electrical properties and their size comparable with many elements of neural network, have attracted increased attention as scaffolding system governing and directing neural fate. In fact, synthetic polymers, in the perspective of creating biomimetic scaffolds, could have been represented a valid alternative;

however, due to the fact they are usually insulating materials, they fail in promoting/potentiating or, at least, emulating the electrical properties of nerve tissue.

At present, CNTs applications in neuroscience include electrical interfaces for neuronal stimulation and recording (both *in vitro* and *in vivo*) [72-73] and scaffolds to support/promote neuronal survival, differentiation, growth and performance (see Paragraph 1.7.2). Neural interfaces are realized to link bi-directionally the brain and an external device, either by stimulating or by recording from neural tissue. In this framework, the major challenges are represented by the improvement of the stimuli sensitivity as well as of signals transfer efficiency from and to neural networks besides the stability in the operating conditions [74]. Such objective could be approached by developing smart nanomaterials that emulate the native ECM and remain efficient for a long period with minimal invasiveness (i.e. minimal inflammation and cell loss) [72]. In other words, it becomes decisive the ability of such nano-tools to direct an integration of the device with neuronal cells (membrane) by matching, for instance, the mechanical properties as well as the shape of the electrodes to brain or spinal cord micro- and nano-features.

The physical and chemical features of the electrode are particularly crucial in the perspective to improve neural interface performances. Not only metallic and inorganic semiconductor materials have been usually interfaced with nervous system, but also polymers and, in particular, conductive polymers [74]. Based on the limitations of polymeric scaffolds, represented mostly by the absence of electrical conductivity and the weak mechanical properties, conductive nanostructures, like CNTs, have been incorporated into these materials. In fact, it was reported that the addition of CNTs, because of their outstanding electrical properties, gives to traditional metallic electrode higher charge storage capacity and lower impedance [75-76].

Apart as device-cell integration facilitators, CNTs have received profound interest also as scaffolds to support/promote neuronal survival, differentiation, growth and electrical performances (see Paragraph 1.7.2). In this sense, the potential CNTs ability to direct neural tissue regeneration after injury [77] could provide a novel paradigm to approach CNS repair. Such finding supports the powerful strategy based on nanoscale engineering, for which physical cues alone could address various biological responses (i.e. nerve tissue reconstruction), without the use of sophisticated biomolecules selective patterning.

The current peculiar achievements in CNTs science applied to neuroscience pave the way to tune/control neural network reorganization and functionality via the use of smart nano-engineered materials showing the ability to interface, change and repair nerve tissue.

1.7.2 CNTs and neurons: a promising interaction

One of the first studies demonstrating that CNT-based substrates (MWCNTs layers coated with 4-hydroxynonenal (4-HNE)) deposited on polyethyleneimine (PEI) coated glass coverslips) are effectively capable of sustaining neuronal growth and neurite elongation in all directions, without forming branches on the CNTs, was conducted by Mattson *et al.* in 2000. Importantly, this was the first study demonstrating also the fundamental role of CNTs functionalization on neural responses [78]. In fact, by comparing 4-HNE functionalized MWNTs with pure MWNTs, they revealed that the first type of CNTs better promote processes growth and extension. Many other studies have reported the important role of CNTs surface charge in directing neurite outgrowth and branching [79]. As an example, by comparing the effect of pristine (without chemical modifications), negatively charged (carboxylated) and positively charged (ethylenediamine) CNTs on neurons, an increase in neurite branching, number of growth cones and average neurite length was observed for cells grown on positively charged MWNTs with respect to those cultured in the other two conditions [80].

Beside the CNTs surface charge, also the electrical conductivity of neuro-scaffolds has a prominent role in neurite outgrowth [81]. In fact, it was demonstrated that CNTs carpets (polyethylene glycol (PEG)-functionalized CNTs solution sprayed on glass support) with different thickness and conductivity, but same average roughness, impact differently on dissociated hippocampal neurons. In particular, the electrical conductivity has influenced the neurite length that was significantly higher for neurons grown on the scaffold with the smallest conductivity (0.3 S/cm) compared to that of neurons cultured on PEG-CNTs characterized by larger conductivities (28 and 42 S/cm) or on polyethyleneimine substrate (control). Therefore, since the surface charge and the electrical conductivity of neuro-scaffolds strongly impact on neuronal outgrowth, could be adopted as strategic parameters to tune neuronal growth itself.

Moreover, in neural regeneration the geometry of the scaffold is crucial in the optic to specifically drive axonal regrowth. In this context, micro-and nano-lithographic techniques

were exploited in order to realize patterned CNTs substrates demonstrating how neurons, by sensing the physical and chemical properties of the underlying substrate, preferentially grow on the CNT paths following these geometrical features (Figure 8) [82].

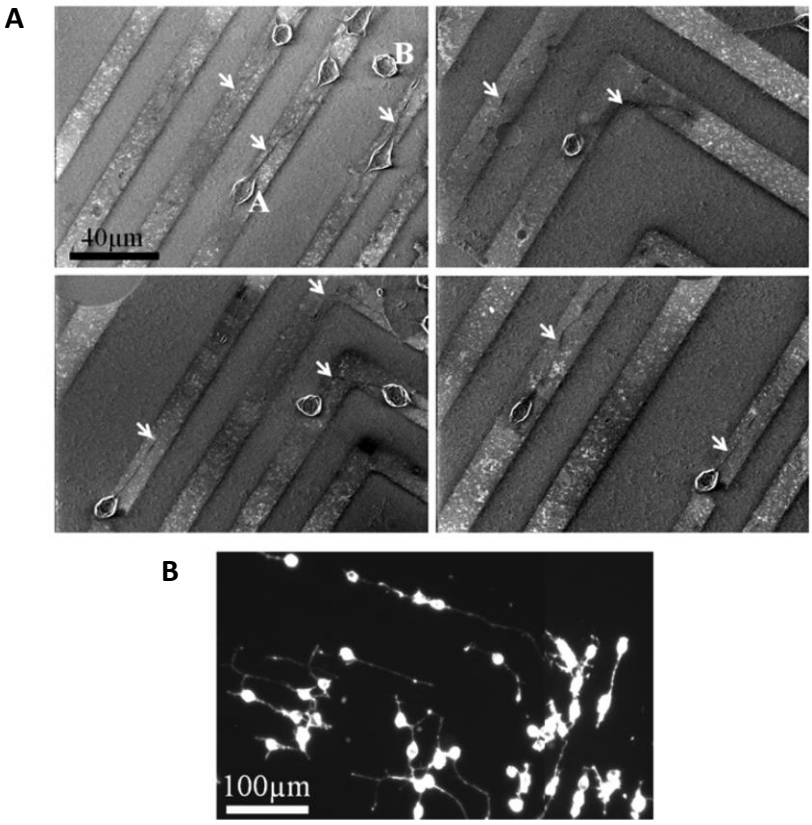

Figure 8. (A) Scanning electron microscopy (SEM) micrograph showing neuronal cells grown on patterned CNTs substrates. Arrows indicate neurite developed on CNTs micropatterns. The letter A and B point to cell body on CNTs and on SiO_2 respectively. (B) Optical fluorescence image of neural cells grown on patterned CNTs patterns. Note that neurites follow the CNT lines turning at an angle of 90°. (Image from [82])

Moreover, Galvan-Garcia and colleagues in 2007 demonstrated that neurons grown on carpets of entangled CNTs show similar neurite length to controls (neuronal cells cultured on standard polyornithine treated glass substrates), but a larger number of growth cones, characterized by larger dimension and a more branched shapes, were present, thus suggesting the possibility to employ CNTs as smart tools to enhance neurite (re)growth [83].

However, one of the most exciting CNTs ability in neuroscience has been revealed in the last decade, when, by evaluating the CNTs impact on the electrical performances of neural web, their surprising ability to deeply impact on neural electrical physiology was reported [54]. In particular, this study was focused on MWNTs initially functionalized by 1,3-dipolar

cycloaddition of azomethine ylides, in order to gain CNT purification of any heavy-metal residues and to obtain a uniform dispersion. Such purified MWNTs were then deposited on a glass coverslip and, finally, thermally de-functionalized, thus obtaining a sufficiently stable and homogeneous CNTs film on the glass substrate to allow cell culturing. In neurons grown on the as-prepared CNT mats, a boosting (about 6-fold) of the frequency of spontaneous post-synaptic currents was detected with respect to control experiments (neurons cultured on glass coverslip). Such evidence was further corroborated by revealing CNTs ability to powerfully increase the spontaneous firing frequency without affecting neuronal survival or morphology [69]. By means of single-cell electrophysiology experiments, electron microscopy analysis and theoretical modelling, it was hypothesized that carbon nanostructures can provide a sort of electronic shortcut between the proximal and distal compartments of a neuron, via a tight but discontinuous contact between neuronal membranes and CNTs [84-85] (Figure 9). However, the detailed mechanism responsible for the potentiating effect on neurotransmission in the presence of CNTs, still necessitate to be entirely clarified.

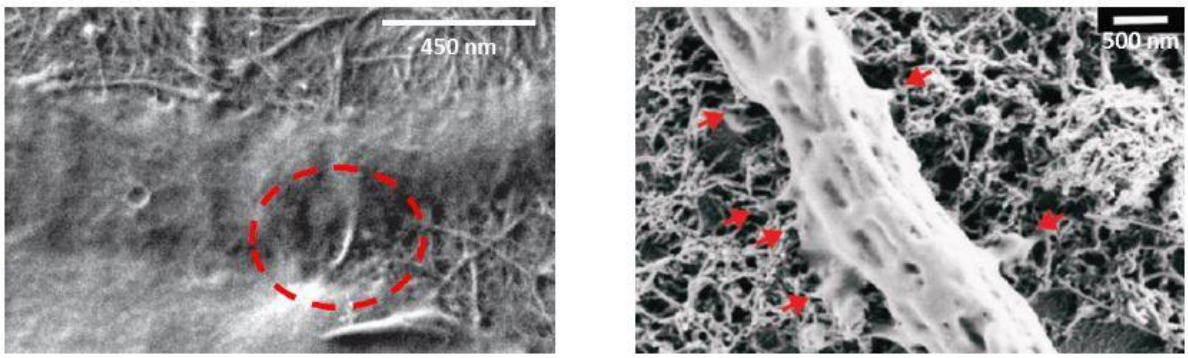

Figure 9. (left) SEM micrograph revealing CNTs meshwork establishing intimate and tight contact (highlighted by the red circle) with cultured hippocampal membrane (Image from [85]); (right) SEM image showing a peripheral neuronal fiber cultured on CNTs carpet with several and very tight contacts between CNTs and the neuronal membrane (red arrows) (Image from [55]).

Since such findings have determined a great fervor in the scientific community, the use of CNTs as neuronal growth substrates has considerably increased and further investigated. For instance, it is now clear that CNTs impact on neurons both at single cell level (CNTs promote synaptogenesis –the formation of new synaptic contacts– and modulate their plasticity) [86-87] and at the network level (i.e. embryonic spinal cord dorsal root ganglia interfaced with CNTs display increased neurite outgrowth and enhanced electrical responses) [55].

Therefore, CNTs demonstrated to possess the capability to profoundly impact neuronal processes, such as dendrite excitability, synaptic formation and plasticity. In this intriguing and promising interaction between neurons and nanotubes, some remarkable properties of CNTs, as their topographical features, mimicking cytoskeletal components, high electrical conductivity and physicochemical features, definitely play a crucial role in affecting neural formation and activity. More recently, a novel scaffold to investigate how and if a neural network grow/interact, both structurally and functionally, with CNTs in the third dimension, was developed [88]. This 3D scaffold, implemented with nanotubes, has proven to be effectively able not only to provide a real three-dimensional organization to the developed neuronal network, but to boost neural network activity in *in vitro* models. The same 3D scaffold was able to establish a functional and synchronized cross-talk between spinal organotypic co-cultures while, in *in vivo* models, induced a limited scar formation when implanted in the rat primary visual cortex in vivo [89].

1.8 CNTs and cardiac diseases: a possible therapeutic approach

CNTs-based scaffolds can be adopted not only to study cell behavior and/or instruct the growth, organization and functionality of neural networks, but also to improve the design of cardiac tissue constructs for supporting/restoring cardiac systems. Cardiovascular diseases (CVD) represent the main cause of death (one of every three adults is affected by CVD) in USA [90] and include various pathologies (i.e. heart and valve diseases, cardiac and vascular structural malformations, cardiomyopathies). Currently, the standard strategies adopted for the treatments of CVD such as angioplasty and bypass grafting, do not lead to a long-term solution and, consequently, patients are forced to undergo further interventions, thus reducing the quality of life and, at the same time, increasing costs. Therefore, the use of novel biocompatible and functional engineered constructs able to restore entirely or partially heart functionality may represent a promising strategy to overcome such limitations. Cardiovascular scaffold features and design will be different depending on the application that, in this context, is represented by the specific heart pathology [91].

Our interest has been directed towards calcific aortic valve diseases (CAVD), which comprise aortic sclerosis, determining increased echogenicity combined with leaflet thickening, and stenosis, characterized by an obstruction of left ventricular outflow [92]. Such diseases are profoundly related to remarkable variations in ECM organization, composition and mechanical properties. In order to design a scaffold owning a (nano)structure able to reduce

disease progression, replace injured tissue and/or improve internal tissue repair, it is important to highlight the structure, composition and mechanical properties of a healthy aortic valve. Briefly, aortic valves (i.e. left coronary, right coronary, and non-coronary) are composed by three leaflets which, in turn, are stratified into three layers (i.e. substantia fibrosa, spongiosa, and ventricularis) differing in terms of composition and micromechanical properties. Such compositional and mechanical layer heterogeneity affects, at macroscopic level, the mechanical behavior of leaflets that results anisotropic (more compliant in the radial direction than in the circumferential direction) [93]. The cellular phase in the aortic valve consists of valvular endothelial cells (VEC) and valvular interstitial cells (VIC), populating only the surface and all the layers of the leaflet, respectively (Figure 10). Our attention was focused mainly on VIC, the predominant constituent of valve tissue, governing ECM structure and composition, in both physiological and pathological conditions.

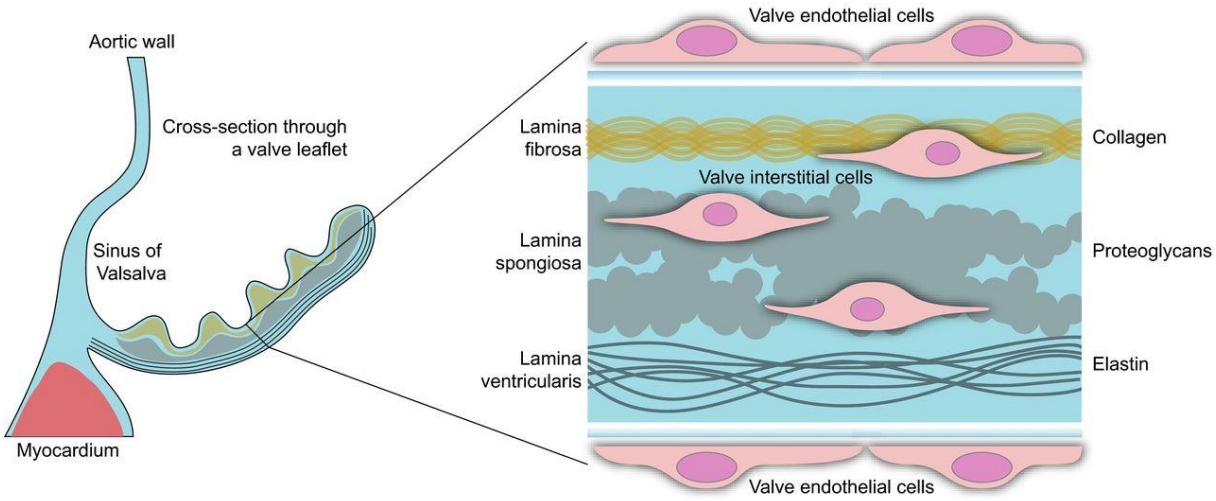

Figure 10. Simplified structure of the human aortic valve leaflet. On the left, a schematic cross section through the aortic valve leaflet. The blowup on the right shows the tri-layered organization of the extracellular matrix and the localization of the aortic valve endothelial cells (shortened throughout to VECs) and interstitial cells (VICs) (Image from [94].

They are composed, in healthy physiological conditions, by fibroblasts (Fib), myofibroblasts (Mfib) in a small percentage (<5%) and smooth muscle cells (SMc); while in a diseased tissue present a significant increase in myofibroblasts (up to 30%) and in collagen production resulting in higher ECM stiffness [92]. Moreover, while in a healthy aortic valve, ECM shows an ordered assembly of collagen fiber, under tissue damage the matrix secreted by VIC becomes disordered and devoid of any kind of alignment [95]. Various *in vivo* studies demonstrated that a disordered collagen fiber ensemble is present in many pathological

conditions occurred in different tissues. As an example, Bodi and coworkers, in 2016, have shown that in humans the outer region of the myocardial infarcted area appears more disordered and not aligned with respect to the central zone. Moreover, very recently, by observing the localization of Yes-associated protein (YAP) and alpha-smooth muscle actin (alpha-SMA), mechano-transduction and myofibroblast marker, respectively, was hypothesized that VIC phenotypic transition is influenced by the local variation of ECM mechanics, determined in turn by the deposition of collagen fibers [95]. Therefore, the variations in VIC behavior (phenotypic transition from fibroblast to myofibroblasts), occurring in pathological conditions, are strongly interconnected with ECM composition and organization (i.e. from organized to disordered).

Several remarkable issues remain to be finely addressed (i.e. molecular triggers responsible for ECM remodeling under pathological conditions, specific proteins involved in ECM dynamic change, molecular mechanism (signaling pathways) involved, ECM effects on cells other than VIC, ECM mechanics evolution over time (aging) in physiological and pathological conditions). However, it is evident that the ECM is the most important player. In this scenario, engineering artificial ECM-like (bio)materials could provide not only novel additional insights into the cells-ECM interaction in aortic valve (healthy and sick), but also offer promising strategies to slow or even prevent the progression of CAVD.

Among them, CNTs, possessing structural properties similar to those of the collagen and laminin proteins (major constituents of ECM), besides peculiar mechanical and electrical properties, represent promising tools by which approaching the described objectives.

The literature reports a general field related to carbon nanomaterials (CNM) for cardiac scaffolds, starting from 2012, in which the effect of 2D and 3D CNM-based scaffolds mainly on cardiomyocytes has been investigated [96]. A part from the lack of electrical conductivity and the weak mechanical strength, the main drawback of traditional polymeric scaffolds is that they are not properly capable of mimicking the fiber structures at sub-micron scale (10–30 nm in diameter), which are abundant in native ECM. In order to overcome the aforementioned limitations, CNM were employed ‘alone’ or added into polymeric matrices (i.e. gelatin which can be mixed with other polymers such as chitosan or poly(glycerol sebacate)) in various studies, demonstrating an enhancement of physical and physiological properties of the hybrid cardiac scaffolds (CNM-based scaffolds interfaced with cells) (Figure 11) [97-101].

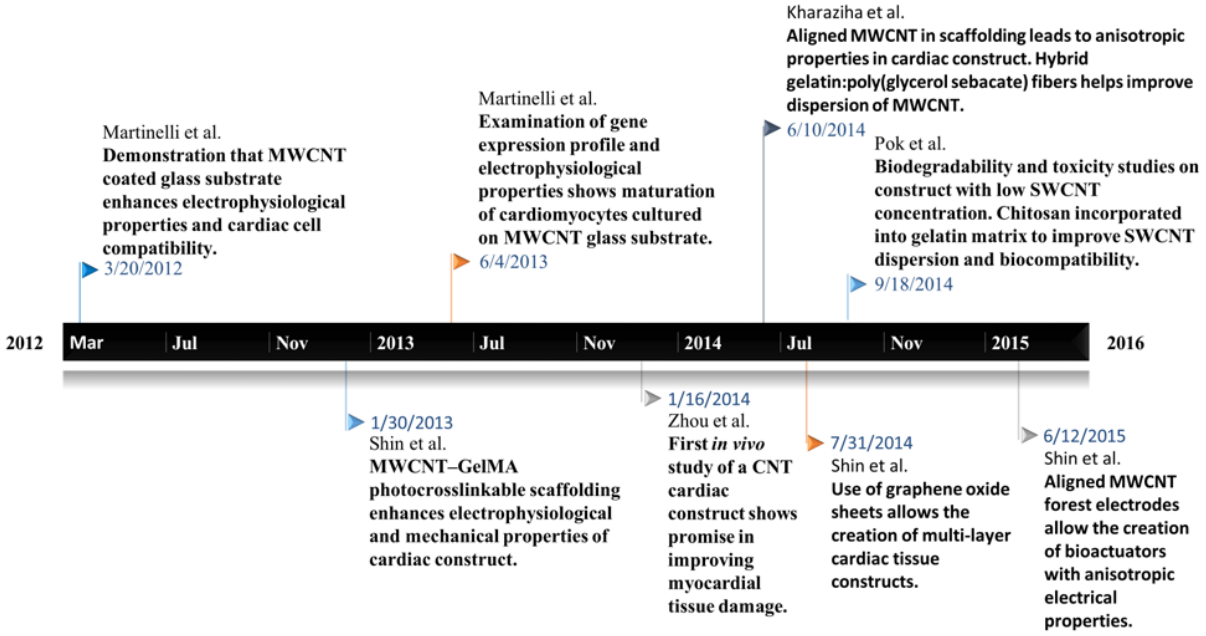

Figure 11. Timeline of major progressions in employing CNM-based materials in cardiac tissue constructs [96].

In particular, it has been reported that drop-casted MWNTs on glass substrates promoted electrophysiological performances of cardiomyocytes [97]. Moreover, a scaffolding structure, obtained by seeding neonatal rat cardiomyocytes onto carbon nanotube (CNT)-incorporated photo-cross-linkable gelatin methacrylate (GelMA) hydrogels, has shown a significant improvement in electrophysiological and mechanical properties [98]. Besides *in vitro* demonstrations, also *in vivo* it has been verified that CNTs-based cardiac scaffolds (SWCNTs incorporated into gelatin hydrogel construct) have a promising impact on damaged myocardial tissue [99]. Additionally, in a very recent study, aligned chemical vapor deposition (CVD)-grown CNTs were, first, embedded into a flexible and biocompatible hydrogel and, then, colonized by cardiomyocytes. Such bio-actuators presented a high mechanical integrity and an anisotropic electrical conductivity that is provided by the embedded CNT microelectrode arrays. Notably, anisotropic conductivity is also observed in the heart, parallel and perpendicular to the direction of cellular alignment [100].

Another aspect that must be taken into account is represented by the mechanical properties of the engineered cardiac construct. Various studies have revealed that the addition of CNM, and specifically of CNTs, into traditional scaffolds improve their ability to mimic heart mechanical properties [96]. For example, it was observed that the incorporation of

homogeneously distributed CNT meshwork into macroporous GelMA hydrogel led to an increase in compression modulus from 10 to 32 kPa [101]. Furthermore, Kharaziha and colleagues, in 2014, demonstrated that the addition of CNTs to aligned poly(glycerol sebacate):gelatin (PG) electrospun nanofibers leads to significantly enhanced toughness, tensile strength and elastic modulus of scaffolds compared to PG scaffolds [102].

Overall, CNTs-based scaffolds have displayed their ability to enhance electrical and mechanical properties of cardiac cells. While ongoing research studies are being committed to address the CNTs toxicity, further improvements, in this field, will open up a widespread exploitation of such carbon structure in all clinical and *in vitro* related applications.

References

[1] J. Foolen, T.Yamashita, P. Kollmannsberger, *Shaping Tissues by Balancing Active Forces and Geometric Constraints*. J. Phys. D: Appl. Phys., 49, 053001, 2016.

[2] C. Frantz, K. M. Stewart, V. M. Weaver, *The Extracellular Matrix at a Glance*. J. Cell Sci., 123, 4195−4200, 2010.

[3] Y. Li, Y. Xiao, C. Liu, *The Horizon of Materiobiology: A Perspective on Material-Guided Cell Behaviors and Tissue Engineering*. Chem. Rev., 117, 4376−4421, 2017.

[4] N. Huebsch, D. J. Mooney, *Inspiration and Application in the Evolution of Biomaterials*. Nature, 462(7272): 426–432, 2009.

[5] B. D. Ratner, S. J. Bryant, *Biomaterials: Where we have been and where we are Going*. Annu. Rev. Biomed. Eng., 6, 41−75, 2004.

[6] B. Alberts, A. Johnson, J. Lewis, M. Raff, K.Roberts, P. Walter. *Molecular Biology of the Cell*. 4th edition, New York: Garland Science; 2002.

[7] R. O. Hynes, A. Naba, *Overview of the matrisome— an inventory of extracellular matrix constituents and functions*. Cold Spring Harb. Perspect. Biol. 4, a004903, 2012.

[8] R. B. Sylvie, *The collagen family*. Cold Spring Harb Perspect Biol;3:a004978, 2011.

[9] J. D. Humphrey, E. R. Dufresne, M. A. Schwartz, *Mechanotransduction and extracellular matrix homeostasis*. Nat Rev Mol Cell Biol., 15(12):802-12, 2014.

[10] P. Roca-Cusachs, T. Iskratsch, M. P. Sheetz, *Finding the weakest link – exploring integrin-mediated mechanical molecular pathway*. Journal of Cell Science 125 (13), 3025–3038, 2012.

[11]S. H. Kim, J. Turnbull, S. Guimond. *Extracellular matrix and cell signalling: The dynamic cooperation of integrin, proteoglycan and growth factor receptor*. Journal of Endocrinology, 209, 2, 139–151, 2011.

[12] F. Zampieri, M. Coen, G. Gabbiani, *The prehistory of the cytoskeleton concept*. Cytoskeleton, 71, 464–471, 2014.

[13] K. A. Jansen, D. M. Donato, H. E. Balcioglu, T. Schmidt, E. H. J. Danen, G. H. Koenderink *A guide to mechanobiology: Where biology and physics meet*. Biochimica et Biophysica Acta 1853, 3043–3052, 2015.

[14] H. B. Michael Schopferer, B. Hochstein, S. Sharma, N. Mücke, H. Herrmann, N. Willenbacher, *Desmin and vimentin intermediate filament networks: their viscoelastic properties investigated by mechanical rheometry*, J. Mol. Biol. 388, 133–143, 2009.

[15] Y. Kim, H. Ko, I. K. Kwon, K. Shin. *Extracellular matrix revisited: Roles in tissue engineering*. International Neurourology Journal, 20 (2016), S23–S29, 2016.

[16] V. Vogel, M. Sheetz, *Local force and geometry sensing regulate cell functions*, Nature Reviews Molecular Cell Biology 7, 265–275, 2006.

[17] P. Lu, V.M. Weaver, Z. Werb, *The extracellular matrix: A dynamic niche in cancer progression* J. Cell Biol., 196, pp. 395-406, 2012.

[18]M. Nikkhah, F. Edalat, S. Manoucheri, A. Khademhosseini, *Engineering microscale topographies to control the cellesubstrate interface*, Biomaterials 33, 5230-5246, 2012.

[19] C. C. DuFort, M. J. Paszek, V. M. Weaver. *Balancing forces: architectural control of mechanotransduction*. Nat Rev Mol Cell Biol, 12: 308–19, 2011.

[20] M. M. Stevens, J. H. George, *Exploring and Engineering the Cell Surface Interface*. Science, 310, (5751), 1135-8, 2005.

[21] H. Jeon, C. G. Simon, G. Kim, *A mini-review: cell response to microscale, nanoscale, and hierarchical patterning of surface structure*, J. Biomed. Mater. Res. B: Appl. Biomater. 102 1580–94, 2014.

[22] W. Q. Chen, Y. Shao, X. Li, G. Zhao, J. P. Fu, *Nanotopographical Surfaces for Stem Cell Fate Control: Engineering Mechanobiology from the Bottom*. Nano Today, 9, 759−784, 2014.

[23] J. Ballester-Beltrán, M. J. P. Biggs, M. J. Dalby, M. Salmerón-Sánchez, A. Leal-Egaña, *Sensing the difference: the influence of anisotropic cues on cell behavior*, Frontiers in Materials 39, 2, 2015.

[24] J. Pelipenko, P. Kocbek, J. Kristl, *Critical Attributes of Nanofibers: Preparation, Drug Loading, and Tissue Regeneration*. Int. J. Pharm., 484, 57−74, 2015.

[25] N. W. Karuri, S. Liliensiek, A. I. Teixeira, G. Abrams, S. Campbell, P. F. Nealey, C. J. Murphy, *Biological Length Scale Topography Enhances Cell-substratum Adhesion of Human Corneal Epithelial Cells*. J. Cell Sci., 117, 3153−3164, 2004.

[26] J. A. Deeg, I. Louban, D. Aydin, C. Selhuber-Unkel, H. Kessler, J. P. Spatz, *Impact of Local versus Global Ligand Density on Cellular Adhesion*. Nano Lett., 11, 1469−1476, 2011.

[27] M. J. Lopez-Bosque, E. Tejeda-Montes, M. Cazorla, J. Linacero, Y. Atienza, K. H. Smith, Lladó A, Colombelli J, Engel E, Mata A. *Fabrication of hierarchical micro-nanotopographies for cell attachment studies* Nanotechnology 24 255305, 2013.

[28] M. Moffa, A. G. Sciancalepore, L. G. Passione, D. Pisignano, *Combined nano- and micro-scale topographic cues for engineered vascular constructs by electrospinning and imprinted micro-pattern,* Small 10 2439–50, 2014.

[29] M. Veysi, Daniel G-P, Tyler N, John J L and Derek J H, *Controlled neuronal cell patterning and guided neurite growth on micropatterned nanofiber platforms, J. Micromech. Microeng.* 25 125001, 2015.

[30] K. Yang, H. Jung , H. R. Lee, J. S. Lee, S. R. Kim, K. Y. Song, E. Cheong, J. Bang , S. G. Im, S. W. Cho, *Multiscale, hierarchically patterned topography for directing human neural stem cells into functional neurons,* ACS Nano 8 7809–22, 2014.

[31] K. K. B. Tan, J. Y. Tann, S. R. Sathe, S. H. Goh, D. Ma, E. L. K. Goh, E. K. F. Yim, *Enhanced differentiation of neural progenitor cells into neurons of the mesencephalic dopaminergic subtype on topographical patterns,* Biomaterials 43 32–43, 2015.

[32] F. Gelain, *Novel opportunities and challenges offered by nanobiomaterials in tissue engineering*. Int J Nanomedicine, 3(4): 415–424, 2008.

[33] L. Zhang, T. J. Webster, *Nanotechnology and nanomaterials: Promises for improved tissue regeneration*. 4(1), 66-80, 2009.

[34] T. Dvir, B. P. Timko, D. S. Kohane, R. Langer, *Nanotechnological strategies for engineering complex tissues,* Nat. Nanotechnol. 6, 13–22, 2011.

[35] C. P. Barnes, S. A. Sell, E. D. Boland, D. G. Simpson , G. L. Bowlin, *Nanofiber technology: Designing the next generation of tissue engineering scaffolds.* Adv Drug Deliv Rev 59(14): 1413-1433, 2007

[36] V. Beachley, X. Wen, *Polymer nanofibrous structures: fabrication, biofunctionalization, and cell interactions*. Prog Polym Sci 35: 868–892, 2010.

[37] E. Engel, A. Michiardi, M. Navarro, D. Lacroix, J. A. Planell, *Nanotechnology in regenerative medicine: The materials side*. Trends Biotechnol 26, 39–47, 2008.

[38] M. Perán, M. A. García, E. López-Ruiz, M. Bustamante, G. Jiménez, R. Madeddu J. A. Marchal, *Functionalized Nanostructures with Application in Regenerative Medicine*. Int J Mol Sci 13: 3847-3886, 2012.

[39] C. Vaquette, J. J. Cooper-White, *Increasing electrospun scaffold pore size with tailored collectors for improved cell penetration*. Acta Biomater 7: 2544–2557, 2011.

[40] E. Kijeñska, M. P. Prabhakaran, W. Swieszkowski, K. J. Kurzydlowski, S. Ramakrishna, *Electrospun bio-composite P(LLA-CL)/collagen I/collagen III scaffolds for nerve tissue engineering*. J Biomed Mater Res B Appl Biomater100(4): 1093-102, 2012.

[41] R. J. Wade, J. A.Burdick, *Advances in nanofibrous scaffolds for biomedical applications: From electrospinning to self-assembly*. Nanotoday, 9 (6), 722-742, 2014.

[42] M. A. Susano, I. B. Leonor, R. L. Reis , H. S. Azevedo, *Elastic biodegradable starch/ethylene-covinyl alcohol fibre-mesh scaffolds for tissue engineering applications*. J Appl Polym Sci 131: 1–9, 2014.

[43] L. A. Bosworth, L. A. Turner, S. H. Cartmell, *State of the art composites comprising electrospun fibres coupled with hydrogels: a review*. Nanomedicine 9: 322–335, 2013.

[44] A. Raspa, A. Marchini, R. Pugliese, M. Mauri, M. Maleki, R. Vasitad, F. Gelain, *A biocompatibility study of new nanofibrous scaffolds for nervous system regeneration*. Nanoscale 8, 253–265, 2016.

[45] S. Tavakol, R. Saber, E. Hoveizi, B. Tavakol, H. Aligholi, J. Ai, S.M. Rezayat, *Self-assembling peptide nanofiber containing long motif of laminin induces neural differentiation, tubulin polymerization, and neurogenesis: in vitro, ex vivo, and in vivo studies*. Mol. Neurobiol. 53, 5288–5299, 2016.

[46] M. F. De Volder, S. H. Tawflick, R. H. Baughman, A. J. Hart, *Carbon nanotubes: present and future commercial applications*. Science, 399(6119), 535–9, 2013.

[47] S. Iijima, C. Brabec, A. Maiti, J. Bernholc, *Structural flexibility of carbon nanotubes*. J Chem Phys,104, 2089–92, 1996.

[48] M. Jagtoyen, J. Pardue, T. Rantell, F. Derbyshire. *Porosity of carbon nanotubes*. Adsorpt Sci and Technol., 17, 289–293, 2000.

[49] I. A. A. C. Esteves, F. J. A. L. Cruz, E.A. Müller, S. Agnihotri, J.P.B. Mota. *Determination of the surface area and porosity of carbon nanotube bundles from a Langmuirian analysis of sub- and supercritical adsorption data*. *Carbon*, 47(4), 948–956, 2009.

[50] A. M. Ross, Z. Jiang, M. Bastmeyer, J. Lahann. *Physical aspects of cell culture substrates: topography, roughness, and elasticity*. Small, 8:336–55, 2012.

[51] A. Patlolla, B. Knighten, P. Tchounwou. *Multi-walled carbon nanotubes induce cytotoxicity, genotoxicity and apoptosis in normal human dermal fibroblast cells*. Ethn. Dis., 20, 1-17, 2010.

[52] C. Poland, R. Duffin, I. Kinloch, A. Maynard, W.H. Wallace, A. Seaton, V. Stone, S. Brown, W. Mac Nee, K. Donaldson. *Carbon nanotubes introduced into the abdominal cavity of mice show asbestos-like pathogenicity in a pilot study*. Nat. Nanotechnol., 3, 423 – 428, 2008.

[53] Z. Li, T. Hulderman, R. Salmen, R. Chapman, S. S. Leonard, S. H. Young, A. Shvedova, M. I. Luster, P. P. Simeonova. *Cardiovascular effects of pulmonary exposure to single-wall carbon nanotubes*. Environmental Health Perspectives, 115, 377-382, 2007.

[54] V. Lovat, D. Pantarotto, L. Lagostena, B. Cacciari, M. Grandolfo, M. Righi, G. Spalluto, M. Prato, Ballerini L. *Carbon nanotube substrates boost neuronal electrical signaling*. Nano Lett. 2005, 5, 1107 – 1110.

[55] C. Fabbro, H. Ali-Boucetta, T. Da Ros, K. Kostarelos, A. Bianco, M. Prato, *Targeting carbon nanotubes against cancer. Chem. Commun. (Cambridge, UK)*, 48, 3911 – 3926, 2012.

[56] S. Bosi, A. Fabbro, L. Ballerini, M. Prato, *Carbon nanotubes: a promise for nerve tissue engineering?* Nanotechnol Rev, 2(1): 47–57, 2013.

[57] K. T. Al-Jamal, A. Nunes, L. Methven, H. Ali-Boucetta, S. Li, F. M. Toma, M.A. Herrero, W. T. Al-Jamal, H.M. Ten Eikelder, J. Foster, S. Mather, M. Prato, A. Bianco, K. Kostarelos, *Degree of chemical functionalization of carbon nanotubes determines tissue distribution and excretion profile*. Angew Chem. Int. Ed. Engl., 51, 6389 – 6393, 2012.

[58] A. Bianco, K. Kostarelos, M. Prato, *Making carbon nanotubes biocompatible and biodegradable*. Chem. Commun. (Cambridge, UK), 47, 10182 – 10188, 2011.

[59] G. Lamanna, A. Battigelli, C. M. nard-Moyon, A. Bianco, *Multifunctionalized carbon nanotubes as advanced multimodal nanomaterials for biomedical applications*. Nanotech. Rev, 1, 17 – 29, 2012.

[60] A. K. Jain, V. Dubey, N. K. Mehra, N. Lodhi, M. Nahar, D. K. Mishra, N. K. Jain. *Carbohydrate-conjugated multiwalled carbon nanotubes: development and characterization*. Nanomedicine, 5(4):432–442, 2009.

[61] C.H. Villa, T. Dao, I. Ahearn, N. Fehrenbacher, E. Casey, D.A. Rey, T. Korontsvit, V. Zakhaleva, C.A. Batt, M.R. Philips, DA. Scheinberg, *Single-walled carbon nanotubes deliver peptide antigen into dendritic cells and enhance IgG responses to tumor-associated antigens*. ACS Nano, 5(7): 5300–5311, 2011.

[62] X. Li, H. Liu, X. Niu, B. Yu, Y. Fan, Q. Feng, F. Z. Cui, F. Watari, *The use of carbon nanotubes to induce osteogenic differentiation of human adipose-derived MSCs in vitro and ectopic bone formation in vivo*. Biomaterials, 33(19): 4818–4827, 2012.

[63] Y. Cao, Y. M. Zhou, Y. Shan, H. X. Ju , X. J. Xue , *Preparation and characterization of grafted collagen multiwalled carbon nanotubes composites.* J Nanosci Nanotechnol, 7:447–451, 2007.

[64] Z. Tosun, P. S. McFetridge, *A composite SWNT–collagen matrix: characterization and preliminary assessment as a conductive peripheral nerve regeneration matrix*. J Neural Eng. 7:31–41, 2010.

[65] E. E. Silva, H. H. M. D. Colleta, A. S. Ferlauto, R. L. Moreira, R. R. Resende, S. Oliveira, G. T. Kitten, R. G. Lacerda, L. O. Ladeira, *Nanostructured 3-D collagen/nanotube biocomposites for future bone regeneration scaffolds*. Nano Res, 2:462–473, 2009.

[66] S. Namgung, T. Kim, K. Y. Baik, M. Lee, J. M. Nam, S. Hong. *Fibronectin–carbon-nanotube hybrid nanostructures for controlled cell growth*. Small, 7(1):56–61, 2010.

[67] E. C. Amerman. *Human Anatomy & Physiology*. Ed. by Pearson, 2016.

[68] B. Hille, *Ionic Channels of Excitable Membranes*, 3*rd* ed. Sinauer, Sunderland, MA, 2001

[69] A. Fabbro, M. Prato, L. Ballerini, *Carbon nanotubes in neuroregeneration and repair,* Advanced Drug Delivery Reviews, *65* (15), 2034-2044, 2013.

[70] R. Sorkin, A. Greenbaum, M. David-Pur, S. Anava, A. Ayali, E. Ben-Jacob, Y. Hanein, *Process entanglement as a neuronal anchorage mechanism to rough surfaces,* Nanotechnology 20, 015101, 2009.

[71] G. A.Silva, *Neuroscience nanotechnology: progress, opportunities and challenges,* Nat Rev Neurosci, 7(1), 65-74, 2006.

[72] N. A. Kotov, J. O. Winter, I. P. Clements, E. Jan, B. P. Timko, S. Campidelli, S. Pathak, A. Mazzatenta, C. M. Lieber, M. Prato, R. V. Bellamkonda, G. A. Silva, N. W. S. Kam, F. Patolsky, L. Ballerini, *Nanomaterials for Neural Interfaces***,** Adv Mater, 21:3970, 2009.

[73] E. W. Keefer, B. R. Botterman, M. I. Romero, A. F. Rossi, G. W. Gross, *Carbon nanotube coating improves neuronal recordings*, Nat. Nanotechnol. 3, 434–439, 2008.

[74] P. Fattahi, G. Yang, G. Kim, M. R. Abidian**,** *A Review of Organic and Inorganic Biomaterials for Neural Interfaces*, Adv Mater, 26(12): 1846–1885, 2014.

[75] M.R Abidian, K.A Ludwig, T.C Marzullo, D.C Martin, D.R Kipke, *Interfacing Conducting Polymer Nanotubes with the Central Nervous System: Chronic Neural Recording using Poly(3,4-ethylenedioxythiophene) Nanotubes.* Adv Mater. 5; 21(37):3764-377, 2009..

[76] M. David-Pur, L. B.-Keren, G. Beit-Yaakov, D. Raz-Prag, Y. Hanein, *All-carbon-nanotube flexible multi-electrode array for neuronal recording and stimulation,* Biomed Microdevices. 16(1): 43–53, 2014.

[77] A. Fabbro, A. Villari, J. Laishram , D. Scaini, F. M. Toma, A. Turco, M. Prato, L. Ballerini, *Spinal cord explants use carbon nanotube interfaces to enhance neurite outgrowth and to fortify synaptic inputs*. ACS Nano, 6:2041–2055, 2012.

[78] M. P. Mattson, R. C. Haddon, A. R. Rao *Molecular functionalization of carbon nanotubes and use as substrates for neuronal growth*. J. Mol. Neurosci, 14, 175 – 182, 2000.

[79] J. V. Veetil, K. Ye. *Tailored carbon nanotubes for tissue engineering applications*. Biotechnol Prog, 25(3):709–721, 2009.

[80] H. Hu, Y.C Ni. , V. Montana, R. C. Haddon, V. Parpura, *Chemically functionalized carbon nanotubes as substrates for neuronal growth.* Nano Lett 4: 507–511, 2004.

[81] E. B. Malarkey, K. A. Fisher, E. Bekyarova, W. Liu, R. C. Haddon, V. Parpura, *Conductive single-walled carbon nanotube substrates modulate neuronal growth,* Nano Lett. 9, 264–268, 2009.

[82] A. Béduer, F. Seichepine, E. Flahaut, I. Loubinoux, L. Vaysse, C. Vieu, *Elucidation of the role of carbon nanotube patterns on the development of cultured neuronal cells*, Langmuir 28, 17363–17371, 2012.

[83] Galvan-Garcia P, Keefer EW, Yang F, Zhang M, Fang S, Zakhidov AA, Baughman RH, Romero MI. Robust cell migration and neuronal growth on pristine carbon nanotube sheets and yarns. J. Biomater. Sci. Polym. Ed . 2007, 18, 1245 – 1261.

[84] Cellot G, Cilia E, Cipollone S, Rancic V, Sucapane A, Giordani S, Gambazzi L, Markram H, Grandolfo M, Scaini D, Gelain F, Casalis L, Prato M, Giugliano M, Ballerini L. Carbon nanotubes might improve neuronal performance by favouring electrical shortcuts. *Nat. Nanotechnol.* 2009, 4, 126 – 133.

[85] A. Mazzatenta, M. Giugliano, S. Campidelli, L. Gambazzi, L. Businaro, H. Markram, M. Prato, L. Ballerini, *Interfacing neurons with carbon nanotubes: electrical signal transfer and synaptic stimulation in cultured brain circuits*. J. Neurosci., 27, 6931 – 6936, 2007.

[86] G. Cellot, F. M. Toma, Z. K.Varley, J. Laishram, A. Villari, M. Quintana, S. Cipollone, M. Prato, L. Ballerini . *Carbon nanotube scaffolds tune synaptic strength in cultured neural circuits: novel frontiers in nanomaterial–tissue interactions*. J Neurosci. 31(36): 12945–12953, 2011.

[87] G. Cellot, F. M. Toma, Z. K. Varley, J. Laishram, A. Villari, M. Quintana, S. Cipollone, M. Prato, L. Ballerini. *Carbon nanotube scaffolds tune synaptic strength in cultured neural circuits: novel frontiers in nanomaterial-tissue interactions*. J. Neurosci, 31, 12945 – 12953, 2011.

[88] S. Bosi, R. Rauti, J. Laishram, A. Turco, D. Lonardoni, T. Nieus, M. Prato, D. Scaini, L. Ballerini L. *From 2D to 3D: novel nanostructured scaffolds to investigate signalling in reconstructed neuronal networks.* Scientific Reports, 5, 9562, 2015.

[89] S. Usmani, E. R. Aurand, M. Medelin, A. Fabbro, D. Scaini, J. Laishram, F. B. Rosselli, A. Ansuini, D. Zoccolan, M. Scarselli, M. De Crescenzi, S. Bosi, M. Prato, L. Ballerini. *3D meshes of carbon nanotubes guide functional reconnection of segregated spinal explants*. Sci Adv, 15, 2(7), 2016.

[90] A .S. Go, D. Mozaffarian, V. L. Roger, et al. *Heart disease and stroke statistics—2014 update: A report from the American Heart Association.* Circulation, 129, e28–e292, 2014.

[91] D. A. Taylor, L. C. Sampaio, A. Gobin, *Building New Hearts: A Review of Trends in Cardiac Tissue Engineering*, American Journal of Transplantation, 14, 2448–2459, 2014.

[92] J. H. Chen, C. A. Simmons, *Cell-Matrix Interactions in the Pathobiology of Calcific Aortic Valve Disease: Critical Roles for Matricellular, Matricrine, and Matrix Mechanics Cues*. Circ. Res. *108*, 1510–1524, 2011.

[93] M. S. Sacks, W. David Merryman, D. E. Schmidt, *On the biomechanics of heart valve function*, J Biomechic, 42:1804 –1824, 2009.

[94] A. Rutkovskiy, A. Malashicheva, G. Sullivan, M. Bogdanova, A. Kostareva, K. Stensløkken, A. Fiane, J. Vaage. *Valve Interstitial Cells: The Key to Understanding the Pathophysiology of Heart Valve Calcification*, Journal of the American Heart Association, 6 (9), 1-23, 2017.

[95] H. Ma, A. R. Killaars, F. W. Del Rio, C. Yang, S. Kristi, K. S. Anseth, *Myofibroblastic activation of valvular interstitial cells is modulated by spatial variations in matrix elasticity and its organization*, Biomaterials 131, 131e144, 2017.

[96] M. D. Dozois, C. Laura. L. C. Bahlmann, Y. Zilberman, X. S. Tang, *Carbon Nanomaterial-Enhanced Scaffolds for the Creation of Cardiac Tissue Constructs: A New Frontier in Cardiac Tissue Engineering*, Carbon, 120, 338-349, 2017.

[97] V. Martinelli, G. Cellot, F. M. Toma, C. S. Long, J. H. Caldwell, L. Zentilin, M. Giacca, A. Turco, M. Prato, L. Ballerini, L. Mestroni, *Carbon nanotubes promote growth and spontaneous electrical activity in cultured cardiac myocytes*. Nano Lett. 12, 1831–1838, 2012.

[98] V. Martinelli, G. Cellot, F. M. Toma, C. S. Long, J. H. Caldwell, L. Zentilin, M. Giacca, A. Turco, M. Prato, L. Ballerini, L. Mestroni, et al., *Carbon nanotubes instruct physiological growth and functionally mature syncytia: nongenetic engineering of cardiac myocytes*. ACS Nano 7, 5746–5756, 2013.

[99] J. Zhou, J. Chen, H. Sun, X. Qiu, Y. Mou, Z. Liu, Y. Zhao, X. Li, Y. Han, C. Duan, R. Tang, C. Wang, W. Zhong, J. Liu, Y. Luo, M. M. Xing, C. Wang, *Engineering the heart: evaluation of conductive nanomaterials for improving implant integration and cardiac function*. Sci. Rep. 4, 1–11, 2014.

[100] S. R. Shin, C. Shin, A. Memic, S. Shadmehr, M. Miscuglio, H.Y. Jung, S. M. Jung, Bae H., A. Khademhosseini, X. S. Tang, M. R. Dokmeci, *.Aligned carbon nanotube–based flexible gel substrates for engineering biohybrid tissue actuators.* Adv. Funct. Mater. 25, 4486–4495, 2015.

[101] S. R. Shin, M.J. Jung, M. Zalabany, K. Keekyoung, P. Zorlutuna, S. Kim et al., *Carbon nanotube-embedded hydrogel sheets for engineering cardiac constructs and bioactuators*. ACS Nano 7, 2369–2380, 2013.

[102] M. Kharaziha, R. S. Shin, M. Nikkhaha, S. N. Topakaya, N. Masoumi, N. A., M. R. Dokmeci, A. Khademhosseini, *Tough and flexible CNT–polymeric hybrid scaffolds for engineering cardiac constructs*. Biomaterials 35, 7346–7354, 2014.

2. Carbon Nanotubes: structure, properties and synthesis

Since their discovery in 1991 [1], the enormous push for CNTs application in many research areas has been inspired by the possibility to exploit their intriguing and, somewhat, even exotic properties. This Chapter will deal with the discussion of some of such properties, which have made CNTs so appealing over the past decades. Moreover, among the various techniques developed to produce CNTs, more emphasis will be given to chemical vapor deposition (CVD), since such technique has been employed to produce CNTs discussed in this thesis.

2.1 Structure and Properties

Ideal carbon nanotube (CNT) can be described as a cylinder made of one (Single Walled Carbon Nanotubes – SWCNTs) or more (Multi Walled Carbon Nanotubes – MWCNTs) layers of graphene (one atom-thick sheet of graphite) closed at each extremity by a half fullerene molecule [2]. The structure of CNTs determines the majority of their properties. Therefore it is necessary to start from a brief description of nanotube's atomic structure. CNT conformation is defined by the *chiral vector* ($\vec{C}_h$), also known as the *roll-up vector*, defined by the relation [3]:

$$\vec{C}_h = n\vec{a}_1 + m\vec{a}_2$$

$\vec{a}_1$ and $\vec{a}_2$ are the two lattice vectors of the hexagonal structure characterized by an sp^2 bonding, where each carbon atom joined to three neighbors, as in graphite; while *n* and *m* determines the chirality of nanotube and, in turn, their mechanical and electronic properties (Figure 1). The module of the chiral vector corresponds, geometrically, to the nanotube's circumference. Perfect SWCNTs can be categorized, based on how the hexagonal sheet of graphite is 'rolled' up to form a nanotube (i.e. geometry of the carbon bonds around the nanotube's circumference) in three crystallographic configurations: *zig-zag*, *armchair* and *chiral*. When two opposite C-C bonds are parallel to the tube axis ($\theta = 0°$; (*n*, 0)), a zig-zag conformation occurs; while, the armchair conformation is characterized by the C-C bonds perpendicular to the tube axis ($\theta = 30°$; (*n*, *n*)). In all other possible cases ($0° < \theta < 30°$) the nanotubes are chiral.

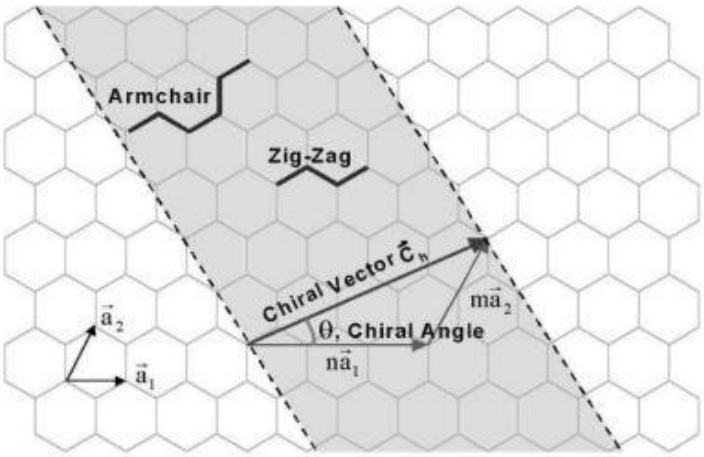

Figure 1. Schematic overview showing how a hexagonal sheet of graphite is 'rolled' to form a carbon nanotube with different chirality.

2.1.1 Electrical properties

Two bond types are found in CNTs: the σ bond, which forms the hexagonal sp^2 network making up the cylindrical walls of the nanotube, and the π bond, stemming from delocalized electrons, which lies perpendicular to the tube surface and is responsible for the weak van der Walls interaction between different tubes. Being the in-plane σ bond too far away from the Fermi level, the electron transport is dominated by π orbitals, which cross exactly at the Fermi level [4]. Interestingly, one of the most intriguing properties of CNTs relies on the possibility to be either metallic or semiconducting, depending on the tube geometry, mainly characterized by the chiral vector, as described in the previous section. Besides defining the wrapping direction and even its diameter, the chiral vector also univocally determines the electronic structure of the tube. In fact, when $n\text{-}m=3q$, being q an integer number, the single-walled CNT behaves as a metal, while for $n\text{-}m\neq3q$ it shows semiconducting properties, with an energy bandgap scaling inversely with the nanotube's diameter [5]. Nevertheless, only armchair CNTs (where $n=m$) are intrinsic metals, while for non-armchair conducting CNTs with diameters <1.5 nm, the partial σ-π re-hybridization originating from the tube curvature may open up a small gap (~0.02 eV) [6]. Accordingly, about one third of all CNTs are metallic, with the remaining two-thirds being semiconducting. Moreover, electrons can flow ballistically along CNTs, meaning that the mean free path of the charge carriers is smaller than the conductor's length and no energy is dissipated by Joule heating. As a consequence, the estimated current carrying capability (the so-called *Ampacity*) for CNTs is 10^9 A/cm^2,

outperforming copper by 1000 times (Cu will melt at 10^6 A/cm^2) [7-8]. Furthermore, quantized conductance in CNTs stems from their extremely fine-wire shape, which makes them behave as electron wave-guides. The conductance of arc-produced MWCNTs has been demonstrated, by Frank and coworkers [8], to be one unit of the conductance quantum $G_0=2e^2/h$ (=12.9 kΩ)$^{-1}$, as shown in Figure 2. In the referred work, an SPM (Scanning Probe Microscope) probe's tip was replaced by a single MWCNT, which was immersed in a liquid mercury bath in order to establish an electric contact necessary to measure the CNTs conductance, corresponding to various immersion depths, thus allowing the measurement of the conductance variation *vs* distance between the probe and the metal's surface (Figure 2).

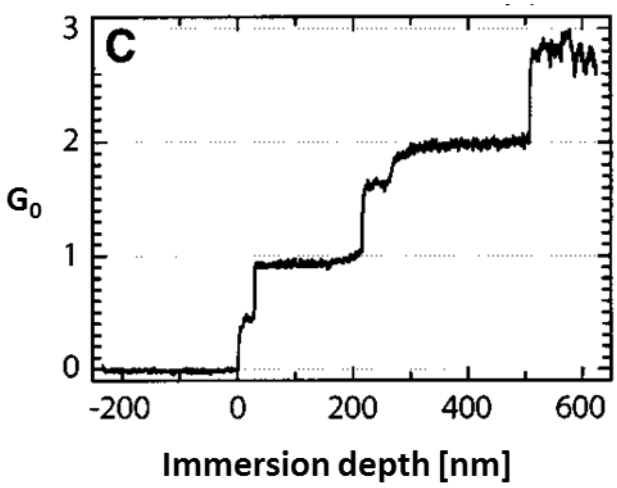

Figure 2. Measured conductance of a MWCNT attached on an STM probe, as a function of the immersion depth into a liquid Hg bath, acting as the counter electrode (re-adapted from [8]).

2.1.2 Optical properties

Because of their 1-D geometry, CNTs were expected to have strongly structured optical spectra. However, due to the marked tendency to assemble into bundles, photoluminescence from SWCNTs was not observed clearly until the pivotal work by O' Connell and colleagues [9]. In such study, the authors were able to separate such bundles into individual tubes, thus paving the way to investigate the photoluminescence and optical spectroscopy of CNTs. As already predicted by calculations, isolated CNTs have showed strong photoluminescence, with no shift between absorption and emission lines, together with very sharp and narrow

absorption lines, as shown in Figure 3, where the optical spectra in the near infrared range for tubes having diameters between 0.7 nm and 1.1 nm is reported.

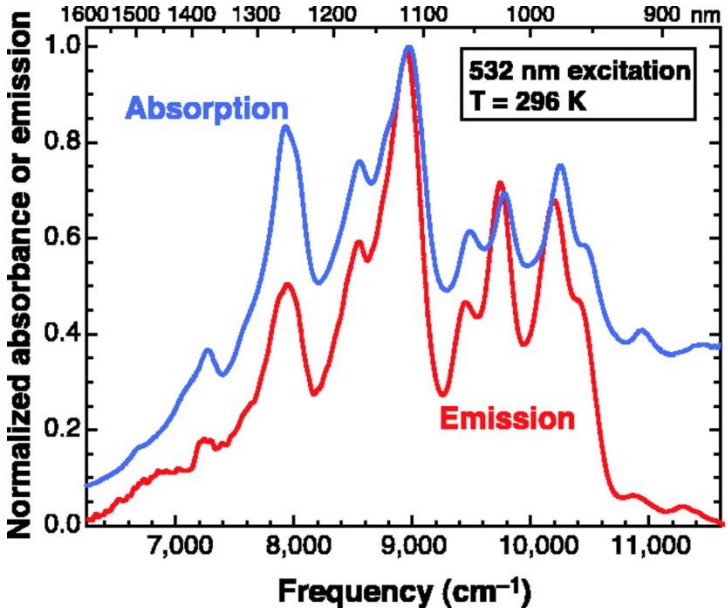

Figure 3. Emission and Absorption spectra of isolated SWCNTs, showing the appearance of a strong photoluminescence, indicated by the perfect frequency matching of the absorption and emission peaks. (Image from [9]).

Other fascinating optical properties may originate from the structural arrangement of CNTs, such as the black body-like behavior observed in SWCNTs forests. For instance, Mizuno and coworkers [10] found that a forest of vertically aligned SWCNTs is capable of absorbing most of the incident light (in the 0.2÷200 μm wavelength range), opening up the possibility to realize a black body absorber in the real world. Figure 4 shows a comparison of the emissivity spectra of various structures derived from the same SWCNT forests, indicating that the black body behavior is only partially due to the intrinsic CNTs properties, while the incredibly high emissivity observed (hence, the absorptivity, based on Kirchhoff's law) can be ascribed to the aerogel-like structure, leading to a suppression of the reflection coefficient, thanks to a refractive index close to air's value.

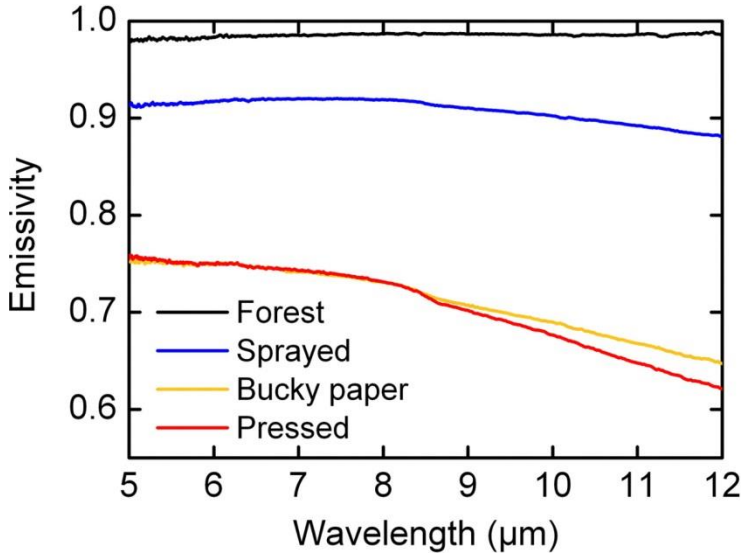

Figure 4. Comparison of spectral emissivity of different SWCNT structures. SWCNTs-based forest (black), spray-coated film (blue), filtrated bucky paper (yellow), and roll-pressed sheet (red)(Image from [10]).

2.1.3 Mechanical properties

The astonishing mechanical properties of CNTs arise mainly from the in-plane C=C σ bond, occurring all over the nanotube walls, which is known to be among the strongest bonds in nature [R. Saito 1998]. Besides the strong σ bonds, the elastic properties of CNTs are driven also by the presence of out-of-plane intra-layer π orbitals, and weak interlayer interactions [11]. Before CNTs were available in suitable amounts to perform accurate mechanical properties characterization, several theoretical studies have tried to address their elastic modulus and tensile strength: as early as 1993, Overney and colleagues [12] have used first principle calculations to predict a bending elastic modulus of 1.5 TPa for SWCNTs consisting of 100 to 400 atoms, showing also that rigidity scales inversely with the CNT diameter. Such results were partially confirmed four years later by J. P. Lu, who reported a Young's modulus of ~ 1 TPa for various types of CNTs, regardless of the nanotube's diameter and helicity, by using an empirical lattice dynamic model [13].

The first indirect experimental estimation dates back to 1996, when Treacy and coworkers [14] were able to determine the Young's moduli from the intrinsic thermal vibration of isolated CNTs inside a Transmission Electron Microscope, obtaining values in the 0.4÷4.12 TPa range.

Only a year later Wong reported the first direct measurement of the elastic modulus and bending strength of individual arc-discharge produced CNTs, by pinning the nanotubes via lithography onto a MoS_2 substrate and then probing the mechanical properties through an AFM tip. The measured average values for Young's modulus and bending strength are 1.28±0.59 TPa and 14.2±8 GPa, respectively [15]. The first stress-strain measurements over MWCNTs were performed in 2000 by Ruoff's group, by carrying out tensile load experiments directly inside a SEM chamber [16]. Using direct stress-strain experiments, the measured Young's moduli were in the 270÷950 GPa range, while the measured tensile strength was between 11 and 63 GPa, with strains at break as high as 12%. While similar mechanical properties were found for arc-discharge produced MWCNTs and highly ordered SWCNT [17], Salvetat and colleagues were the first to compare the mechanical properties of highly crystalline arc-produced MWCNTs with disordered MWCNTs, produced via catalytic CVD [18]. By suspending CNTs over anodic alumina membranes, having 200 nm pores, the authors were able to measure the elastic modulus through AFM. In doing so, they showed that as-grown "arc-discharge" MWCNTs, consisting of nested graphene layers (Figure 5) perfectly aligned with the tube axis, have an average modulus of 870 GPa, much higher than CVD-grown MWNTs, composed of a 'piled-up coffee cup structure', with an average elastic modulus of only 27 GPa, roughly 30 times lower than their crystalline counterparts.

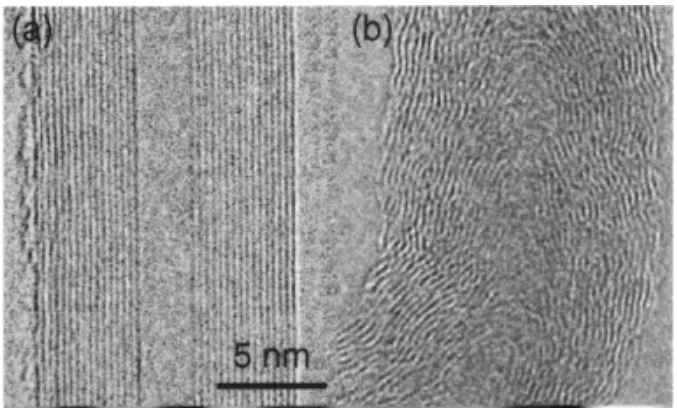

Figure 5. TEM micrographs highlighting the difference between highly crystalline arc-discharge produced (a) and disordered CVD-grown MWCNTs (b). (Image from [18]).

From the aforementioned results, it is clear the widespread dispersion of reported data, can be ascribed to differences in the type of CNTs (i.e. purity, density, type of defect and chirality),

but also to the different methods employed to measure the mechanical behavior. Table I reports a list of the experimentally measured CNTs mechanical properties, along with the various techniques employed, in chronological order (readapted from [19]).

Measuring Method	**Elastic Modulus**	**Tensile Strength**	**CNT type and growth method**	**Ref**
Thermal vibration by TEM	1.8 TPa	-	Arc discharge - MWNTs	[14]
Cantilever beam by AFM	1.28±0.59 TPa	14.2±8 GPa	Arc discharge - MWNTs	[15]
Thermal vibration by TEM	1.25 TPa	-	Laser ablation- SWNTs	[20]
Compression monitored by micro-Raman spectroscopy	2.825÷3.577 TPa 1.718÷2.437 TPa	-	Laser ablation -SWNT Arc discharge - MWNT	[21]
Simple-supported beam bending model by AFM tip and TEM	0.87 TPa 0.027 TPa	-	Arc discharge – MWNT CVD -MWNT	[18]
Tensile test in 'nanostressing stage' in SEM and TEM	0.27÷0.95 TPa	11÷63 GPa	Arc discharge – MWNT	[16]
Three-point bending by AFM	1.2 TPa	-	CVD-SWNTs	[22]
Pulling and bending by TEM	0.91 TPa	150 GPa	Arc discharge – MWNT	[23]
Bending a clamped MWCNT beam by AFM tip and TEM beam Mechanics	0.35±0.11 TPa	-	CVD-MWNT	[24]
TEM/AFM tensile Loading	0.62÷1.2 TPa	10÷66 GPa	Arc discharge – MWNT	[25]

Rayleigh scattering spectroscopy/tensile test by AFM cantilever	0.97±0.16 TPa	40.6 GPa	CVD-SWNTs	[26]
TEM and AFM tensile Loading	0.05÷1.36 TPa 0.03÷1.09 TPa	2÷48 GPa 1÷18 GPa	CVD-MWNT Acid treated defective MWNT	[27]

Table I. List of experimentally measured Elastic moduli and tensile strength of CNTs, produced through different methods, in chronological order.

2.2 Chemical vapor deposition of carbon nanotubes

Among the various synthesis methods today available for CNTs production, such as laser ablation and arch discharge, just to mention two of them [28-30], chemical vapor deposition (CVD) is the most widely employed. This is mainly due to the fact that it is a simple and cost effective technique and could be easily scaled-up for large-scale or industrial production. Additionally, CVD can employ both hydrocarbons and catalyst in any form (i.e. solid, liquid, vapor). An extremely interesting characteristic of such technique, especially in the field of micro- and nano-electronics and/or biosensing research, is the possibility to pattern a surface with every desired CNTs-based shape simply by patterning the catalyst layer only in surface areas where CNTs have to grow [31]. CVD process has been successfully employed for the fabrication of carbon nanofibers in 1970, and in 1996 stood out as promising technique for large scale synthesis of CNTs [32-33]. In modern CVD synthesis of carbon nanotubes, a hydrocarbon vapor, such as ethylene, methane and acetylene (with typical flow rates between 10 and 30 ml/min [34]), is fluxed (15-60 min) in a tubular reactor in which is located a nanostructured transition metal catalyst, pre-deposited on a substrate, whose temperature must be sufficiently high to decompose the hydrocarbon (from 600 °C to 1200 °C, depending on the cracking temperature of the hydrocarbon molecule used) (Figure 6).

If the hydrocarbon is liquid, such as benzene and alcohol, it is previously heated in a flask and then carried into the CVD reaction area. When, instead, a solid hydrocarbon precursor is used, it have to be placed inside a low-temperature region of the reaction chamber, subsequently, volatile materials, such as camphor, naphthalene and ferrocene, will "sublimate" from the hydrocarbon block and be transported in the high-temperature region of the CVD reactor where the supporting surfaces covered with the catalyst are located. As in the case of the

carbon source, also the catalyst can be employed in any form (i.e. solid, liquid, vapor) and can be directly placed inside the CVD reactor (e.g., as a deposition film above a supporting surface) or injected from the outside (e.g., using an injection nozzle) [35].

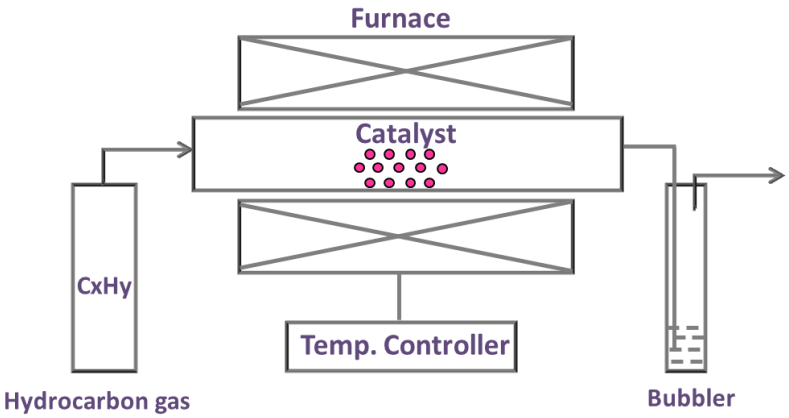

Figure 6. Schematic diagram of a general CVD setup.

The exact CNTs growth mechanism, despite several theories has been proposed to explain it, remains rather controversial. Among them, the widely-accepted mechanism can be described as follows: when the hydrocarbon source gas interacts with the catalyst nanoparticles, if their temperature is sufficiently high, decomposes into carbon and hydrogen. The first starts to dissolve into the nanoparticles, while the hydrogen flies away. The carbon solubility limit in the specific catalyst employed at that temperature dictates the precipitation and crystallization of the as-dissolved carbon into a cylindrical network. Hydrocarbon decomposition (exothermic process) and carbon crystallization (endothermic process) generates a thermal gradient inside the catalyst particles which governs this process. Moreover, the growth mechanism can be divided into two general cases: base growth and tip growth. In the first case, due to a strong interaction between the catalyst and the underlying substrate, the nanotube grows up with the catalyst nanoparticle rooted in its base (Figure 7-A) [36]. In the other case, when the catalyst-substrate interaction is weak, the catalyst is lifted off from the underneath supporting surface during nanotube's growth (Figure 7-B) [37].

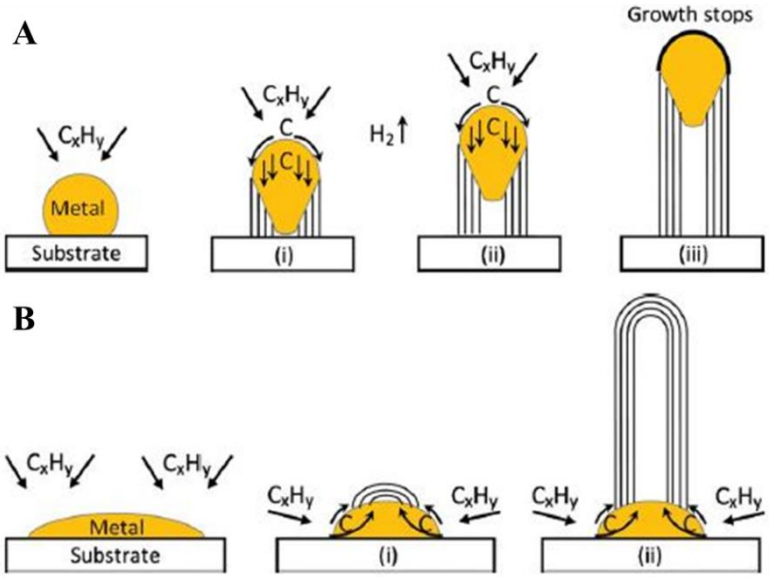

Figure 7. Widely-accepted growth mechanisms for CNTs: (A) tip-growth model, (B) base-growth model (Image from [35]).

2.2.1 The catalyst

In order to lower as much as possible the hydrocarbon source gas decomposition temperature, CVD growth of CNTs necessitates the use of metal nanoparticles catalyst acting as nucleation sites for CNT growth. The most widely employed metals are Fe, Co and Ni, because of the high carbon solubility and diffusion rate in these metals at high temperature [38]. In this scenario, the nano-structuration of the catalyst plays a key role. In fact, because of the increase in the surface-to-volume ratio at the nanoscale level, physical and chemical reactivity of the materials change compared to the bulk counterpart, thus resulting in lower melting temperatures and higher carbon solubility in metal nanoparticles.[39-40]. It is general experience that the surface or bulk diffusion of the carbon in the catalyst particle determines the adsorption and consequent crystallization of carbon after reaching the saturation level. At the same time, it is still under debate which is the catalyst nanoparticle state (i.e. solid or liquid form) during CNTs growth as well as the type of carbon diffusion mechanism, in particular if it occurs on the surface or in the bulk of the catalyst nanoparticles [41]. Regarding the first aspect, it is influenced by the interaction with the underneath supporting substrate together with the thermal gradient 'driving' CNTs growth, according to the most accepted CNTs growth mechanism (see previous section). Baker and colleagues [42], during the first attempt to investigate *in-situ* carbon filament growth via transmission electron microscopy (TEM), have clearly identified a change in the shape of nickel

nanoparticle, thus assuming that it was in liquid phase. Other works, performing *in-situ* TEM observation during CNT growth, have revealed a crystalline structure of nickel and iron particles characterized by diameters higher than 5 nm [41]. Nevertheless, aside from such findings, it was generally observed a change in the shape of catalyst nanoparticles during CNTs growth, turning from a spherical conformation to an elongated shape and resulting also partially or completely encapsulated into the nanotube [35,38]. The extremely high surface energies associated to the nanometric curvature radius of such nanoparticles could explain how Fe, Co, Ni, characterized by a bulk melting point of about 1500 °C, could be in liquid state at temperature ranging from 600 to 900 °C (temperature range in which normally occurs CVD growth of CNTs). It is in fact important to point out that the melting point of metals decrease with nanoparticle radius, a physical principle all sintering processes take advantage from, falling to very low temperatures for nanoparticles below 10 nm in diameter (Figure 8) [40].

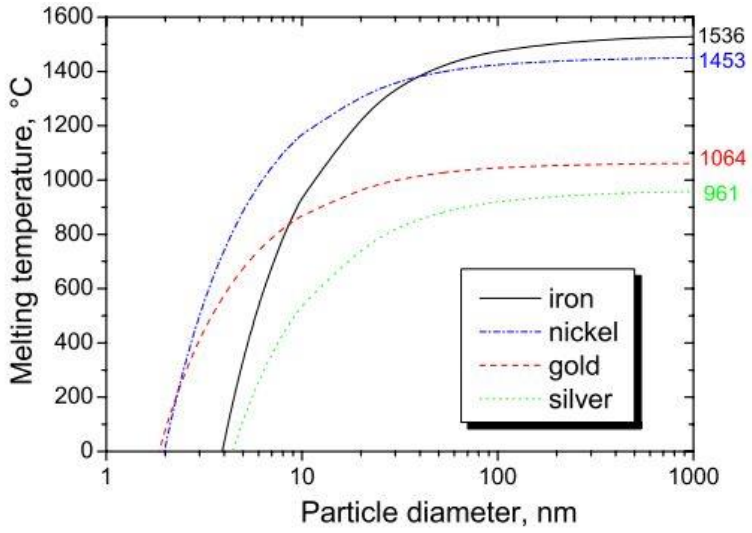

Figure 8. Melting temperature of various metals as a function of particle diameter (Image from [40].

The drastic reduction in the melting temperature values occurs on the lines reported in the figure. Therefore, for nanoparticles having diameters between 1 and 3 nm, it is possible to assess their liquid phase during nanotube (i.e. SWCNTs) growth [40,44]. On the other hands, in the case of MWCNTs, which usually originate starting from bigger (>20 nm) metal particles, it is still not completely clear the metal's physical state. Regarding, instead, the second aspect (i.e. carbon diffusion through the metal particle) remains still a highly-debatable question, because the literature reports works leading to opposite conclusions. As

an example, by observing the benzene decomposition on iron catalyst at 1100 °C, a surface diffusion of carbon on the nanoparticle was hypothesized [45]. Later, by investigating methane decomposition (500 °C) on Ni catalyst nanoparticles, it was observed that the metal remained crystalline during the growth of carbon nanofibers, thus suggesting a bulk diffusion of carbon [46]. Therefore, the exact mechanism by which carbon diffuses on metal nanoparticles is still unknown. At the same time, it is clear that, also in this case, it is strongly related to catalyst particle size, from which in turn depend the particle's physical state, and consequently the diffusion of carbon on its surface or bulk.

2.2.2 The carbon precursor

As previously stated, CVD can exploit various hydrocarbons in any form (i.e. solid, liquid or gas). It is well-documented the strong relationship between CNTs morphology and hydrocarbon molecular structure [35]. Specifically, linear hydrocarbons such as methane, ethylene, and acetylene usually give rise to linear dimers/trimers of carbon, allowing to straight tube; while the decomposition of cyclic hydrocarbons such as benzene, xylene or fullerene results in curved CNTs [35,38]. Additionally, carbon source influences the type of CNTs (i.e. SWCNTs or MWCNTs): high-temperature hydrocarbons such as methane or other carbon containing gas carbon monoxide lead to the synthesis of SWCNTs, due to their higher energy formation which in turn is probably related to small particles (high curvature tolerate high energy) [35]. For CNTs synthesis can be also employed carbon precursor deriving from 'natural' environment. It is the case of camphor, an agricultural product, which has led to the production of CNTs, thus attracting the attention of industrial ecologists [47]. Unfortunately, the main issue of these natural-derived materials is their changeable chemical composition which determines contaminations in the final CNT produced.

Overall, despite the huge improvement in CNTs synthesis over the years, there are various aspects not completely clear and still debated concerning the CNTs growth mechanism which strongly depends on each involved parameter such as carbon precursor, metal catalyst, particle size, temperature, pressure. Despite the numerous open-questions and although the issues related to the fine control of CNTs growth, the CNT research continues to go ahead considerably in the pursuit to solve all these concerns.

2.3 Three-dimensional carbon nanotube networks

Chemical vapor deposition technique was exploited also to realize sponge-like CNT networks, by adding sulfur, a CNTs growth rate enhancer [48], during the synthesis process [49]. As an example, De Crescenzi's group, by employing ferrocene (2.3 wt %), tiophene (1.5 wt %) and acetylene as catalyst, sulfur and carbon precursor, respectively, and carrying out the synthesis of CNTs at 900-1000 °C during an ambient pressure CVD process, have produced freestanding three-dimensional structures entirely made of long and randomly interconnected tubular nanostructures (Figure 9).

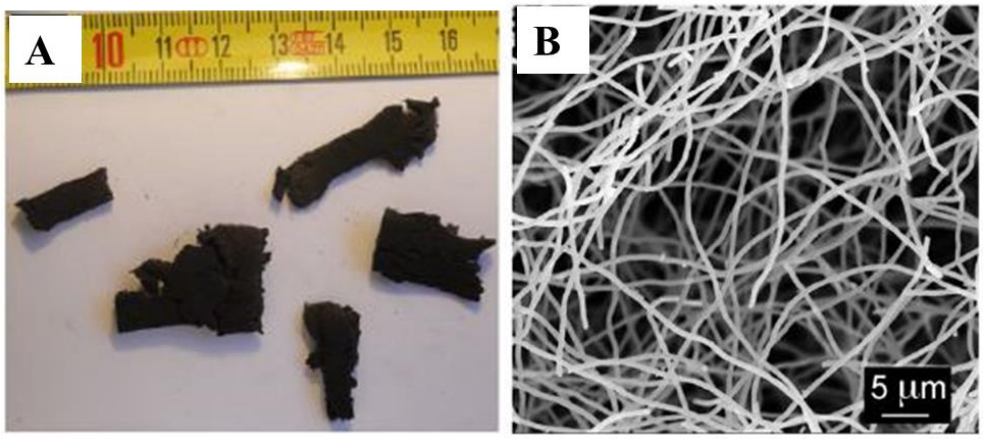

Figure 9. (A) Photo of various CNT sponges synthesized after 30 min of the sulfur-assisted CVD process. (B) SEM micrograph showing the entangled CNTs network which constitutes the sponges. (Image from [49]).

The authors hypothesized that the interconnections between tubes are given by the curled geometry of tubes. Raman spectroscopy performed on the as-produced 3D CNT structures highlighted the high number of structural imperfections characterizing the samples which are required to bend the tubular nanostructures in order to obtain a sponge-like network [50]. In fact, sulfur addition during CVD synthesis induces the formation of structural defects, by introducing pentagon and heptagon carbon rings [49]. Such defects serve as preferential immobilization and nucleation sites for Fe atoms coming from ferrocene. Thus, the exceeding carbon provided by acetylene keeps on the growth of carbon layers, which occurs surrounding and capping the Fe sites. Therefore, sulfur is needed to manufacture defective CNTs characterized by curved and bent graphene sheets, thus giving rise to highly interconnected and random carbon-based network.

References

[1] S. Iijima, *Helical microtubules of graphitic carbon*, Nature, 354, 56–58, 1991.

[2] S. Iijima, T. Ichihashi, *Single-shell carbon nanotubes of 1-nm diameter*, Nature 363, 603–605, 1993.

[3] M.S. Dresselhaus, G. Dresselhaus, P.C. Eklund, *Science of fullerenes and carbon nanotubes*, San Diego: Academic Press, 1996.

[4] S. Reich, C. Thomsen, J. Maultzsch, Chapter 3: *Electronic Properties of Carbon Nanotubes*, Carbon Nanotubes: Basic Concepts and Physical Properties, WILEY-VCH Verlag GmbH & CO**.** KGaA 2004.

[5] A. Eatemadi, H. Daraee, H. Karimkhanloo, M. Kouhi, N. Zarghami, *Carbon nanotubes : properties, synthesis, purification, and medical applications*, Nanoscale Research Letters, 1–13, 2014.

[6] M. Meyyappan, *Carbon nanotubes: science and applications*, CRC Press Inc.: Boca Raton, FL, 2005.

[7] C. P. Poole, F. J. Owens, *Introduction to Nanotechnology*, Wiley&Sons, Inc., 2003.

[8] S. Frank, P. Poncharal, Z. L. Wang, W. A. De Heer, *Carbon Nanotube Quantum Resistors*, 1744 1998, 10–13, 2008.

[9] M. J. O'Connell, S. M. Bachilo, C. B. Huffman, V. C. Moore, M. S. Strano, E. H. Haroz, K. L. Rialon, P. J. Boul, W. H. Noon, J. Ma, R. H. Hauge, R. B. Weisman, R. E. Smalley, *Band Gap Fluorescence from lndividual Single-Walled Carbon Nanotubes*, Science, 80, 297, 5581, 593–596, 2002.

[10] K. Mizuno, J. Ishii, H. Kishida, Y. Hayamizu, S. Yasuda, D. N. Futaba, M. Yumura, *A black body absorber from vertically aligned single-walled carbon nanotubes*, Proc Natl Acad Sci USA, 106 (15), 6044–6047, 2009.

[11] M. S. Saito, R Dresselhaus, G Dresselhaus, *Elastic Properties of Carbon Nanotubes*, Physical Properties of Carbon Nanotubes (Imperial College Press), 1998.

[12] G. Overney, W. Zhong, D. Tom, *Structural rigidity and low frequency vibrational modes of long carbon tubules*, Zeitschrift für Physik D Atoms, Molecules and Clusters, 27 (1) 93–96, 1993.

[13] J. P. Lu, *Elastic properties of single and multilayered nanotubes*, J. Phys. Chem. Solids, 3697 (11), 1649-1652, 1997.

[14] M. M. J. Treacy, T. W. Ebbesen, J. M. Gibson, *Exceptionally high Young's modulus observed for individual carbon nanotubes*, Nature, 381, 678–680, 1996.

[15] E. W. Wong, P. E. Sheehan, C. M. Lieber, *Nanobeam Mechanics: Elasticity, Strength, and Toughness of Nanorods and Nanotubes*, Science, 277, 1971–1975, 1997.

[16] A. M. Yu, O. Lourie, M. J. Dyer, K. Moloni, T. F. Kelly, R. S. Ruoff, M. Yu, O. Lourie, M. J. Dyer, K. Moloni, T. F. Kelly, R. S. Ruoff, *Strength and Breaking Mechanism of Multiwalled Carbon Nanotubes Under Tensile Load*, Science, 287, 637–640, 2000.

[17] J. N. Coleman, U. Khan, W. J. Blau, Y. K. Gun, *Small but strong : A review of the mechanical properties of carbon nanotube – polymer composites*, Carbon, 44, 1624-1652, 2006.

[18] B. J. Salvetat, A. J. Kulik, J. Bonard, G. A. D. Briggs, T. Stöckli, K. Møtønier, S. Bonnamy, F. Bøguin, *Elastic Modulus of Ordered and Disordered Multiwalled Carbon Nanotubes*, Adv. Mater., 2, 161–165, 1999.

[19] Z. Hu, X. Lu, Book Chapter 8: *Mechanical Properties of Carbon Nanotubes and Graphene*, Carbon Nanotubes and Graphene, 2nd Edition. Oxford: Elsevier, 165-200, 2014.

[20] Krishnan, A., Dujardin, E., Ebbesen, T. W., Yianilos, P. N. & Treacy, M. M. J. *Young's modulus of single-walled nanotubes*, Phys. Rev. B 58, 13–19, 1998.

[21] O. Lourie, H. D. Wagner, *Evaluation of Young's modulus of carbon nanotubes by micro-Raman spectroscopy*. J. Mater. Res. 13, 2418–2422, 1998.

[22] T. W. Tombler, , C. Zhou, , L. Alexseyev, J. Kong, H. Dai, *Reversible electromechanical characteristics of carbon nanotubes under local-probe manipulation*, Nature 661, 769–772, 2000.

[23] B. G. Demczyk, Y. M. Wanga, J. Cumingsa, M. Hetmana, W. Hana, A. Zettla, R.O. Ritchie, *Direct Mechanical Measurement of the Tensile Strength and Elastic Modulus of Multiwalled Carbon Nanotubes*, Microsc. Microanal. 12, 934–935, 2006.

[24] G.Guhados, W. Wan, X. Sun, X., J. L. Hutter, *Simultaneous measurement of Young' s and shear moduli of multiwalled carbon nanotubes using atomic force microscopy,* J. Appl. Phys. 101, 2007.

[25] W.Ding, , L. Calabri, K. M. Kohlhaas, X. Chen, *Modulus, Fracture Strength, and Brittle vs. Plastic Response of the Outer Shell of Arc-grown Multi-walled Carbon Nanotubes*, Exp. Mech. 47, 25–36 , 2007.

[26] M. Huang, *Studies of Mechanically Deformed Single Wall Carbon Nanotubes and Graphene by Optical Spectroscopy*. (Columbia University, 2009).

[27] G. Yamamoto, J. W. Suk, J. An, R. D. Piner, T. Hashida, T. Takagi, R. S. Ruoff, *The influence of nanoscale defects on the fracture of multi-walled carbon nanotubes under tensile loading*, Diam. Relat. Mater. 19, 748–751, 2010.

[28] S. K. Tiwari, V. Kumar, A. Huczko, R. Oraon, A. De Adhikari, G. C. Nayak. *Magical Allotropes of Carbon: Prospects and Applications*, Critical Reviews in Solid State and Materials Sciences, 41 (4), 257–317, 2016.

[29] M. Musaddique, A. Rafique, J. Iqbal, *Production of Carbon Nanotubes by Different Routes - A Review*, Journal of Encapsulation and Adsorption Science 1, 29–34, 2011.

[30] B. K. Kaushik, M. K. Majumder, *Carbon Nanotube Based VLSI Interconnects: Analysis and Design*, Carbon Nanotube Based VLSI Interconnects, 1, 86, 2014.

[31] Q. Zhang, J.-Q. Huang, M.-Q. Zhao, W.-Z. Qian, F. Wei, *Carbon nanotube mass production: principles and* processes, Chem Sus Chem 4, 864, 2011.

[32] W. Z. Li, S. S. Xie, L. X. Qian, B. H. Chang, B. S. Zou, W. Y. Zhou, R. A. Zhao,G. Wang, *Large scale synthesis of aligned carbon nanotubes*, Science 274, 1701–1703, 1996.

[33] H. Tempel, R. Joshi, J. J. Schneider, *Ink jet printing of ferritin as method for selective catalyst patterning and growth of multi-walled carbon nanotubes*, Mater. Chem. Phys. 121, 178–183, 2010.

[34] Ç. Öncel, Y. Yürüm, *Carbon Nanotube Synthesis via the Catalytic CVD Method: A Review on the Effect of Reaction Parameters*, Fullerenes, Nanotubes and Carbon Nanostructures, 14(1), 17-37, 2006.

[35] M. Kumar, Y. Ando, *Chemical Vapor Deposition of Carbon Nanotubes: A Review on Growth Mechanism and Mass Production*. Journal of Nanoscience and Nanotechnology, 10, 3739–3758, 2010.

[36] R.T. K. Baker, R. J. Waite, *Formation of carbonaceous deposits from the platinum-iron catalyzed decomposition of acetylene*, J. Catalysis 37, 101, 1975.

[37] R. T. K. Baker, P. S. Harris, R. B. Thomas, and R. J. Waite, *Formation of filamentous carbon from iron, cobalt and chromium catalyzed decomposition of acetylene*, J. Catalysis 30, 86, 1973.

[38] K. A. Shah, B. A. Tali, *Synthesis of Carbon Nanotubes by Catalytic Chemical Vapour Deposition: A Review on Carbon Sources, Catalysts and Substrates*. Mater. Sci. Semicond. Process. 41, 67–82, 2016.

[39] A. Ramirez, C. Royo, N. Latorre, R. Mallada, R. M. Tiggelaar, A. Monzón, *Unraveling the growth of vertically aligned multiwalled carbon nanotubes by chemical vapor deposition*, Materials Research Express 1.4, 2015.

[40] A. Moisala, A. G. Nasibulin, E. I. Kauppinen, *The role of metal nanoparticles in the catalytic production of single-walled carbon nanotubes—a* review, J. Phys.: Condens. Mater. 15, S3011, 2003.

[41] V. Jourdain, Christophe Bichara, *Current understanding of the growth of carbon nanotubes in catalytic chemical vapour deposition*, Carbon 58, pp. 2–39, 2013.

[42] R. T. K. Baker, M. A. Barber, P. S. Harris, F. S. Feates, R. J. Waite, *Nucleation and Growth of Carbon Deposits from the Nickel Catalyzed Decomposition of Acetylene*, Journal of Catalysis, Vol. 26, No. 1, 51-62, 1972.

[43] F. Ding, P. Larsson, J. A. Larsson, R. Ahuja, H. Duan, A. Rosen, K. Bolton, *The Importance of Strong Carbon−Metal Adhesion for Catalytic Nucleation of Single-Walled Carbon Nanotubes*, Nano Lett. 8, 463, 2008.

[44] A. R. Harutyunyan, T. Tokune , *Liquid as a required catalyst phase for carbon single-walled nanotube growth*, Appl. Phys. Lett. 87, 051919, 2005.

[45] A. Oberlin, M. Endo, T. Koyama, *Filamentous growth of carbon through benzene decomposition*, J. Cryst. Growth, 32, 335, 1976.

[46] S. Helveg, C. Lopez-Cartes, J. Sehested, P. L. Hansen, B. S. Clausen, J. R. Rostrup-Nielsen, F. Abild-Pedersen, J. K. Nørskov, *Atomic-scale imaging of carbon nanofibre growth***,** Nature 427, (6973): 426-9., 2004.

[47] M. J. Eckelman, J. B. Zimmerman, P. T. Anastas, *Toward green nano* , J. Industrial Ecology 12, 316, 2008.

[48] Tibbets G. G., Bernard C. A., D. W. Gorkiewicz, *Role of sulfur in the production of carbon fibers in the vapor* phase, Carbon, 32, 569, 1994.

[49] L. Camilli, C. Pisani, E. Gautron, M. Scarselli, P. Castrucci, F D'Orazio, M. Passacantando, D. Moscone, M. De Crescenzi, *A three-dimensional carbon nanotube network for water treatment*, Nanotechnology, 25**,** 065701, 2014.

[50] D. P. Hashim, N. T. Narayanan, J. M. Romo-Herrera, D. A. Cullen, M. G. Hahm, P.Lezzi, J. R. Suttle, D. Kelkhoff, E. Muñoz-Sandoval, S. Ganguli, A. K. Roy, D. J. Smith, R. Vajtai, B. G. Sumpter, V. Meunier, H. Terrones, M. Terrones, P. M. Ajayan, *Covalently bonded threedimensional carbon nanotube solids via boron induced nanojunction* Sci. Rep. 2 363, 2012.

3. Experimental

3.1. Realization of 2D and 3D scaffold for cellular development

In this work, I have designed and fabricated various scaffolds both 2D and 3D with the final purpose to create a reliable approach to tune cellular functionality and properties (i.e. neuronal communication or cellular mechanobiology). To this aim, CNT carpets with well-controlled uniformity and lengths on different substrates were realized. By exploiting the extremely high versatility of our synthesis method, CNT-based 2D patterns of different shape as well as 3D CNT-decorated architectures (e.g. sintered iron foam) were obtained. The synthesis of CNTs was possible thanks to our collaboration with Andrea Goldoni (ELETTRA Synchrotron Light Source, Nano-Materials Lab, Italy). I have worked also on the realization of 3D porous scaffolds made of polydimethylsiloxane (PDMS) characterized by a controlled geometry (porosity and internal canalization) and tuneable mechanical properties in order to investigate/control material-cell interaction and biological response in a three-dimensional frame. Afterwards, thanks to our collaboration with Prof. Laura Ballerini's group (International School for Advanced Studies (SISSA), Neurobiology, Italy), and especially with Dr. Rossana Rauti and Dr. Niccolò Pampaloni, CNT scaffolds were interfaced with hippocampal cultures. Moreover, in collaboration with Centro Cardiologico Monzino and Luisa Ulloa Severino, we have investigated also the effect of CNT carpets on porcine aortic valve interstitial cells (pVICs). Herein, are described in detail the realization routes for each type of produced scaffolds, the main steps of the culturing procedures (hippocampal cultures and VIC) along with the characterization techniques exploited to investigate the scaffolds and their interaction with cells.

3.2 CNT substrates preparation

Carbon nanotubes were grown on p-type <110> silicon wafer chips (SiO_2/Si) via catalytic chemical vapor deposition technique (CCVD) and carrying out the growth for just 90 sec [1]. The wafers were manually cleaved into 15x15 mm^2 chips using a diamond scribe and cleaned by rinsing in ultrasonic baths of acetone and ethanol (1:1) for 15 minutes. Since CVD-assisted CNTs synthesis on a supporting substrate needs a catalytic element, iron was deposited as a thin layer (2–5 nm in thickness) directly on the SiO_2/Si chips via thermal evaporation by employing a custom-made evaporator [2] (Figure 1). Specifically, iron ultrafine powder (Sigma Aldrich >99% purity) was placed on a tantalum crucible electrically connected to a

power supply. SiO_2/Si substrate was mounted over the crucible (hosting the catalyst) and a blade shutter, located between the growth substrate and the crucible, ensure the beginning of iron deposition only under the optimized operation conditions. The evaporation was carried out by setting the heating current up to 60 A for just 9 sec and starting from a pressure in the reaction chamber of $9 \cdot 10^{-6}$ mbar. Subsequently, the growth substrates ($Fe/SiO_2/Si$) were mounted on the heating element inside the high-vacuum reaction chamber (Figure 2). CVD process was preceded by sample thermal annealing (4 min at 670 °C in H_2 atmosphere, up to a partial pressure of $3 \cdot 10^{-1}$ mbar) in order to reduce iron oxides that might be present on sample surface, due to the exposition to atmospheric air conditions during transfer from the metal deposition system to the CVD reactor, and to de-wet the iron layer, thus inducing nanoparticle formation. Then, an acetylene gas (carbon source) was delivered through a flow meter system in the reaction chamber in which the growth chips were located. Thereafter, sample temperature was raised to 700-730 °C and acetylene was introduced into chamber up to a partial pressure of 10–20 mbar. Reaction time was limited to merely 90 sec, resulting in the formation of a uniform network of CNTs of about 10 μm in thickness. Samples were used as removed from the reaction chamber. It is important to highlight that the produced samples consisted of a uniform network of vertically aligned CNTs of thickness increasing with the reaction time. Reaction times below 90 sec lead to entangled CNTs network, showing no preferential alignment. On the other hand, by increasing the reaction time from 1.5 min to 4 min, the CNTs length (i.e. CNTs forest's thickness) can be enhanced from 10 μm up to 200 μm. A further increase of the reaction time beyond 4 min and up to 10 min, only leads to a maximum thickness of the forest of 300 μm, indicating the onset of a saturation effect.

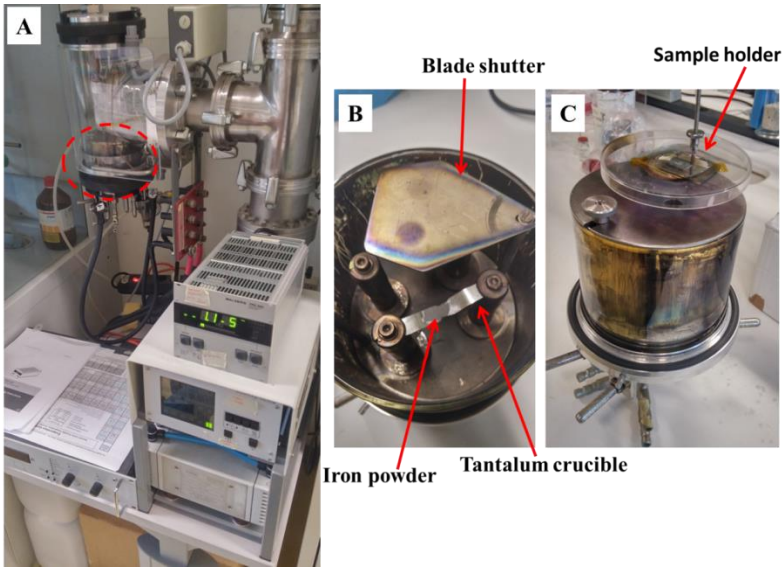

Figure 1. Custom-made thermal evaporator. (A) The thermal evaporation process occurred in a high-vacuum chamber (highlighted by the red circle). The catalyst (iron powder) loaded into the crucible (B) was resistively heated, by applying a large current (60 A), until its surface atoms have enough energy to leave the surface and travel in straight lines to strike the surface of the growth SiO_2/Si substrate (C).

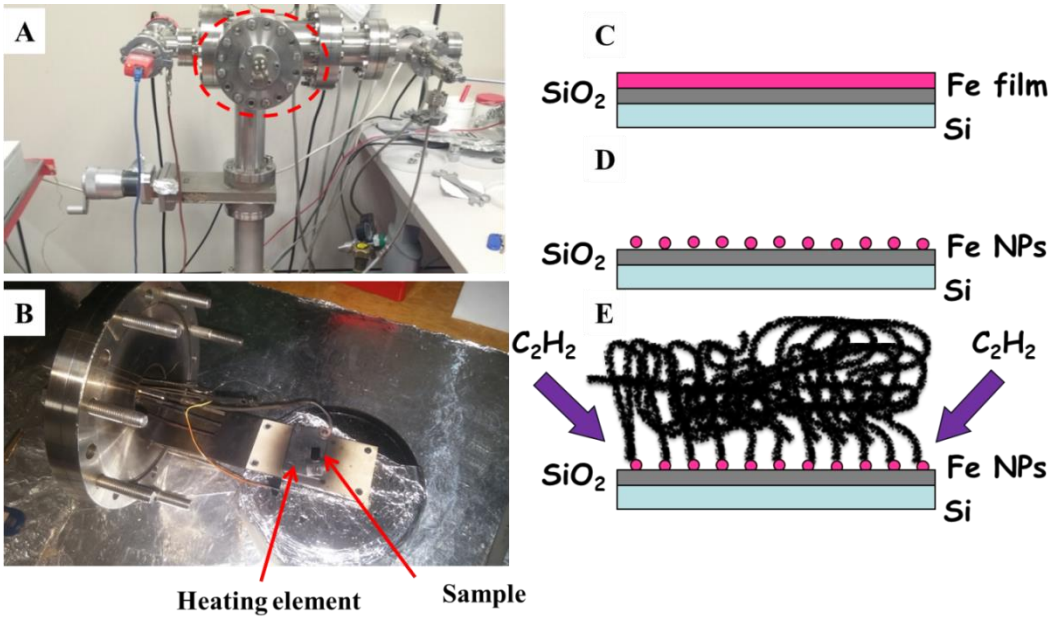

Figure 2. Custom-made CVD system and a scheme of the CVD process employed for CNTs growth. (A) CVD reaction chamber and its extractable flange (highlighted by the red circle) with SiO_2/Si chip champed over the heating element (B). Uniform CNTs forests were grown by CCVD by depositing an ultra-thin catalyst layer of iron on an underneath SiO_2/Si support (C). Then, an annealing treatment was employed to convert the catalyst layer into active metal nanoparticles through catalyst reduction (D). Finally, CNTs growth was carried out by cracking of acetylene as hydrocarbon source gas (E).

3.3 Patterned CNT substrates

A selective growth of CNTs was performed on silicon wafer chips (SiO_2/Si) substrates patterned with octadecyltrichlorosilane [$CH_3(CH_2)_{17}SiCl_3$, (OTS)] by microcontact printing (μCP) method [3] (Figure 3). The OTS ability to spontaneously form self-assembled monolayers (SAMs) on a SiO_2/Si substrate was usually adopted to modify specific surface properties [4-5]. Accordingly, CNTs-based micropatterns were fabricated by a site-selective deposition of the catalytic element (iron as thin layer) by exploiting the OTS capability to create a barrier for metal nucleation and growth [6]. Polydimethylsiloxane (PDMS) stamps with a relief micro-size patterned structure were fabricated according to a previous procedure [7]. Afterwards, the patterns were transferred onto the SiO_2/Si substrates, previously cleaned

by rinsing in ultrasonic baths of acetone and ethanol (1:1) for 15 minutes, by μCP using OTS as ink solution, prepared in reagent grade toluene with a concentration 10 mM. Polyester applicators were used to ink the PDMS stamps with the OTS solutions, and N_2 gun was employed to remove from the stamps the excess solvent. The stamps were kept in contact with substrates for 5 min and then cleaned using acetone followed by N_2 blowing. After that, the catalyst layer was deposited as a thin layer (2–5 nm in thickness) via thermal evaporation (Figure 1) directly on the as-realized OTS-patterned substrates. Finally, the subsequent growth of patterned CNTs was carried out following the same procedure described in the previous section (1.1 CNTs preparation).

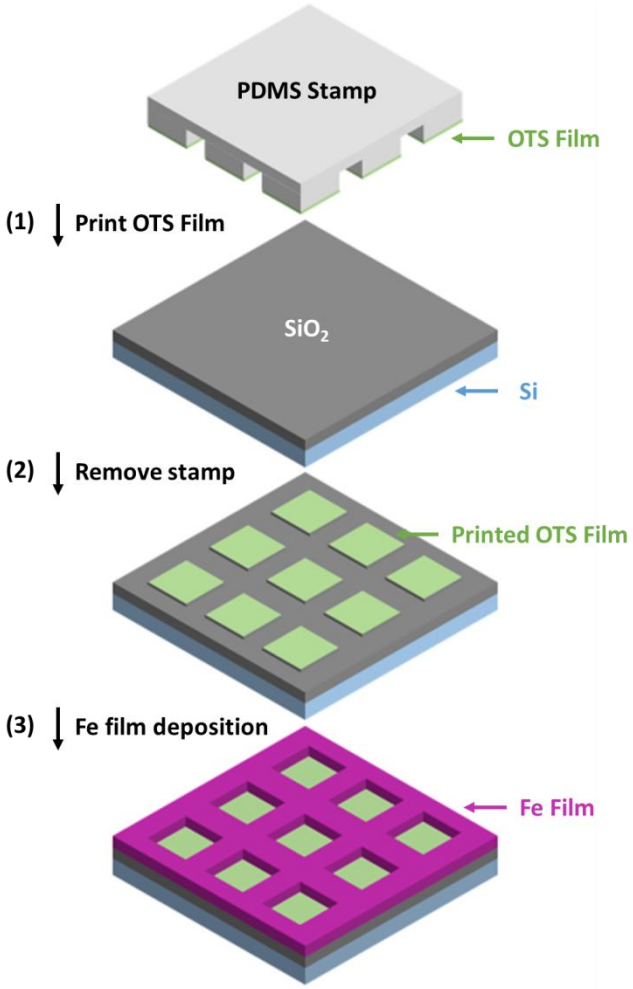

Figure 3. Schematic overview of the procedure followed to synthesized patterned CNTs on substrates that have been previously patterned with OTS film. In the printing procedure we have adopted PDMS stamps with relief features that are inked with OTS solution and then pressed onto the SiO_2/Si substrates (1) realizing a printed OTS film (2). Then, the thin layer of iron was selectively deposited on the OTS-patterned SiO_2/Si substrate; specifically, the selective deposition of iron occurred only around the OTS regions, by exploiting the OTS ability to avoid metal deposition and growth.

3.4 CNTs synthesis on transparent substrates

Multi-walled carbon nanotubes were synthesized by the catalytic decomposition of acetylene (carbon source) over an ultra-thin catalyst layer of iron using fused silica (SiO_2) wafer chips as supporting substrates [8]. The wafers were manually cleaved into 15x15 mm^2 samples using a diamond scribe and cleaned by Radio Corporation of America (RCA) method [9]. This was followed by the deposition of an ultra-thin iron layer (0.2–1 nm in thickness) directly on the SiO_2 chips using electron beam (e-beam) evaporation. Iron film thickness was monitored with an in-situ quartz crystal microbalance. Since the uniformity of the catalyst layer is crucial for CNTs growth, an average deposition rate of 0.2 Å/sec was adopted. Subsequently, the as-evaporated substrates were located on the heating element inside the high vacuum reaction chamber (Figure 2A). A thermal annealing treatment (4 min at 670°C in H_2 atmosphere, up to a partial pressure of $3 \cdot 10^{-1}$ mbar) was performed to reduce iron oxides possibly present on film surface, and to break down the continuous iron layer into nanoparticles which subsequently act as nucleation sites for CNTs growth. Once the pretreatment process was over, the carbon source was immediately introduced in the reaction chamber up to a partial pressure of 10–20 mbar. Sample temperature was increased up to 730°C and reaction time was limited to 90 sec, resulting in the formation of a uniform carpet of CNTs of less than 10 μm in thickness. After that, the samples were cooled down to room temperature and employed as removed from the reaction chamber.

3.5 A step towards 3D: layer-by-layer procedure

In order to create a perfectly controlled CNTs-based 3D system, lithographic and etching techniques have been exploited [10]. The fabrication process (Figure 4) was carried out on 4 inch p-type <110> silicon wafers on which a 2 μm thick silicon nitride (Si_3N_4) film was previously deposited on both sides, via low-pressure chemical vapor deposition (LPCVD). The first lithography was conducted on the front side (Si_3N_4) with the final aim to realize circular through-holes with diameters of 10 μm and a characteristic period of 100 μm. The second step was the transfer of the sloping photoresist patterns into the silicon by etching both photoresist molds and the silicon surface through inductively coupled plasma (ICP) process. Whereupon, a second lithography was performed at the back of the wafer to open large windows (side square 1 mm) aligned not only with the <1 0 0> Si crystallographic axes, but also with the apertures on the top side. This second lithography was followed by the transfer of the pattern into the silicon by ICP. After that, the silicon nitride was etched from the back

side in a reactive ion etcher (RIE) using a CF_4 chemistry. Finally, the silicon bulk was anisotropically wet etched in a 30% KOH solution heated at 80 °C, at a rate of about 1,26 µm /min in order to etch away the thick Si layer through the opening. The anisotropic etching in the silicon crystalline bulk results in an inverted truncated pyramid with 54.74° facets.

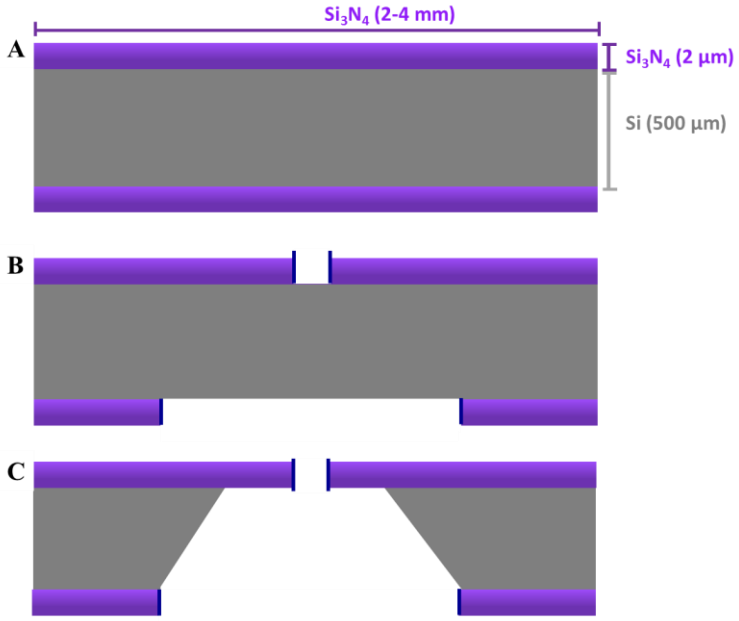

Figure 4. Fabrication process: (A) LPCVD-deposited silicon nitride membranes on both sides of the wafer; (B) First and second lithography performed on the front side (with diameters of 10 µm and a characteristic period of 100 µm) and on the back side (side square 1 mm); (C) Finally, silicon nitride and silicon bulk were etched via RIE and in 30% KOH, respectively.

In order to create a 3D cellular scaffold these membranes could be stacked one on the top of another with the possibility to control and modulate the porosity and the properties of each layer employed. In this way, cells can pass through the holes and extend themselves for the entire thickness of such well-controlled 3D system.

3.6 Fe foam

In order to realize a 3D CNTs-based architecture, we have adopted sintered Fe foam acting both as catalyst and template. Accordingly, a tantalum crucible, containing the iron powders which must be sintered, was located in a quartz tube furnace [11] (Figure 5) under nitrogen atmosphere until reaching 1000 °C; whereupon, the iron powders were exposed to a reducing gas (H_2) for 20 minutes at that temperature. The system was then cooled down to room temperature.

Figure 5. Quartz tube furnace adopted to sintered iron powder.

After the sintering process, the resulting metallic foam was subjected to an acid attack (NITAL solution) in order to increase its surface roughness, thus better catalyzing the CNTs growth. It is documented that short immersion (10-15 s) of metallic sponge in NITAL solution leads to an initial selective attack of the ferritic grain boundaries, but a general corrosion occurs with longer immersion [12]. Two different time of NITAL attack were tested for the as-sintered Fe sponges: 30 and 60 seconds. Subsequently, the specimen was mounted on the heating element inside the CVD chamber (Figure 2A) for the subsequent CNTs growth that was warried out following the same procedure described before (see paragraph 3.2), but with an increase in the annealing and growth time (10 and 20 minutes respectively).

3.7 3D porous PDMS-based scaffolds

3D porous scaffolds made of PDMS characterized by a different geometry (porosity and internal canalization) and mechanical properties were produced. Two types of PDMS were employed: Sylgard® 184 and Sylgard® 527, adopting the standard elastomeric/crosslinking agent precursor ratios of 1:10 and 1:1, respectively. Both polymers were degassed in a vacuum chamber for at least 30 minutes and then stored at -20 °C. PDMS-based scaffolds were obtained by following a modified solvent casting particulate leaching approach (SCPL) [13]. Specifically, after an accurate sieving of glucose (G8270-D-(+)-Glucose Sigma-Aldrich®), the portion between 80-40 μm was selected; 0.8 g of the as-sifted glucose was then mixed with 200 μL of aqueous solution poured into a metal mold and gently pressed. The following aqueous solutions were tested: 100%, 90%, 80%, 70% decane/water, 100% and 80% 2-butanol/water, and a mixture of 50% decane/2-butanol. After the solvent evaporation, PDMS (Sylgard® 184) was poured on the glucose tablets and cured at room temperature for

48 hours. Finally, the glucose leaching out occurred only after more than 24 hours under bath sonication in water (Figure 6).

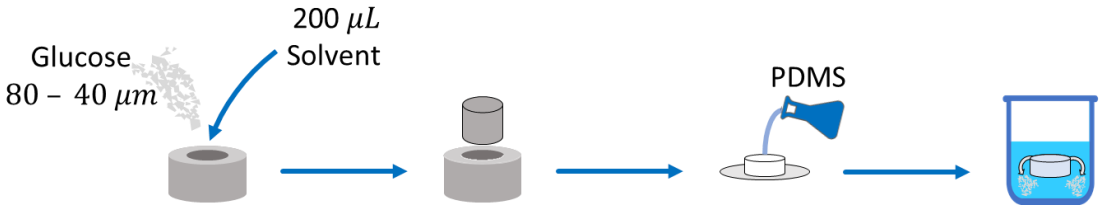

Figure 6. A scheme showing the procedure followed to produce 3D porous PDMS-based scaffolds.

By using a similar approach, but a different 'precursor', 3D PDMS-based scaffolds, characterized by not only pores, but also an internal canalization, were realized. In this case, cotton candy sugar acted as mold template e no solvent solution was employed. The adopted process is shown in Figure 7.

Moreover, we have blended together elastomers with different stiffness (Sylgard® 184 and Sylgard® 527), in order to control the mechanical properties of the realized PDMS-based structures. In particular, we have adopted 3 different blending conditions of Sylgard® 184 (elastic modulus of about: 1.72 MPa) and Sylgard® 527 (elastic modulus of about: 5 kPa): 3:1, 1:3 and 1:5, respectively.

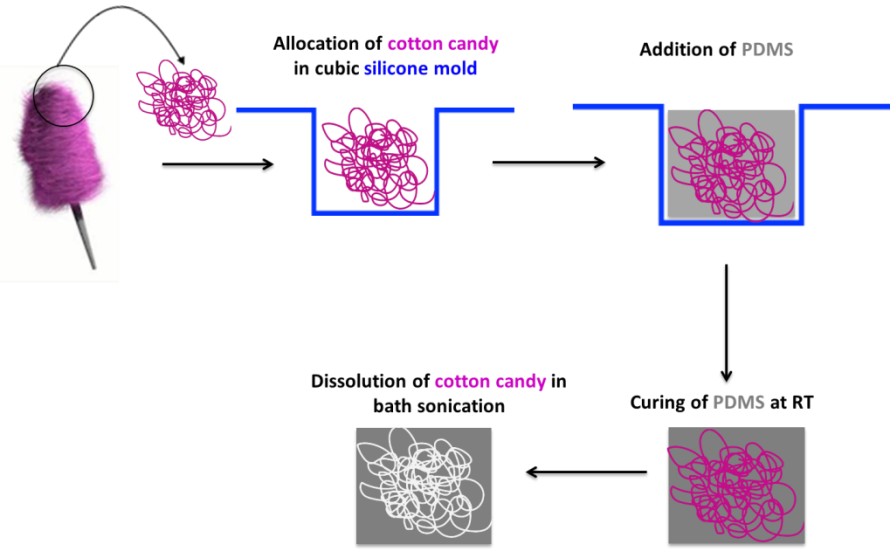

Figure 7. Schematic overview of the process employed to realize 3D PDMS scaffolds with pores and internal canalization.

3.8 CNTs characterization

The morphology of the continuous catalyst layer and the nucleation of Fe nanoparticles on the supporting layer were investigated via AFM, using an XE-100 (Park System). The samples were processed under the same CVD conditions adopted for CNTs growth. Specifically, an iron catalyst layer (~2 nm in thickness) was characterized before and after the thermal annealing treatment performed at 670 °C for 4 min in H_2 atmosphere (up to a partial pressure of $3 \cdot 10^{-1}$ mbar) without introducing acetylene. Topographic measurements were recorded in contact mode in air using an AFM tip (MikroMasch NSC36/CR-AU, spring constant 2 nN nm^{-1}), at 512 × 512 pixels with a cantilever speed of 0.5 Hz. Image processing was performed using Gwyddion analysis software (version 2.40) [14].

Moreover, AFM (Solver Pro, NTMDT, RU) was used also to determine CNTs surface topography. Measurements were carried out in air at room temperature working in non-contact mode. Cantilevers, characterized by a resonant frequency of about 65 KHz (MikroMasch HQ:NSC36/NO AL) were used. AFM images were acquired at 512 × 512 pixels with a cantilever speed of 0.2 Hz and then processed via Gwyddion analysis software (version 2.40) [14].

Field Emission Scanning Electron Microscopy (FE-SEM) imaging was performed on the as-obtained carbon nanostructures to address their diameter, alignment, uniformity and density by using a Gemini SUPRA 40 SEM (Carl Zeiss NTS GmbH, Oberkochen, Germany) operating at an accelerating voltage of 5 keV.

In order to investigate CNTs internal structure (i.e. number of walls in MWCNTs, inner and outer diameter, structural integrity), transmission electron microscopy (TEM) was performed using an EM 208-Philips TEM system equipped with Quemesa (Olympus Soft Imaging Solutions) camera. Before TEM imaging, samples were released from the substrates, dispersed in ethanol and a drop of the solution was deposited onto a commercial lacey-carbon grid. [In collaboration with Dr. Paolo Bertoncin, TEM facility of the University of Trieste].

To evaluate the purity, structure and defects of CNTs combined with the possibility to discriminate MWCNTs from other carbon allotropes, Raman spectroscopy was conducted on at room temperature employing a Renishaw inVia Raman microscope with a 60x objective lens at 632.8 nm laser excitation and a laser power of 2 mW. [In collaboration with Prof. Alois Bonifacio, University of Trieste, Italy].

In order to evaluate the CNTs surface composition, X-ray Photoelectron Spectroscopy (XPS) was carried out using a commercial Xray photoelectron spectrometer (VG-ESCALAB-II) equipped with a monochromatic Al Kα X-ray source (1486.6 eV) and a hemispherical energy analyzer with a base pressure below 1×10^{-10} mbar. Core-level XPS data analysis was performed after the removal of nonlinear Shirley background and deconvolution into Gaussian/Lorentzian components using Casa-XPS software. [In collaboration with Dr. Matteo Dalmiglio, University of Trieste, Italy].

3.9 PDMS-based scaffolds characterization

The morphologies of 3D PMDS platforms, previously sliced (200 μm) and gold metallized, were qualitatively assessed through SEM operating at an accelerating voltage of 2 keV.

X-ray microcomputed tomography was employed to characterize/reconstruct the three-dimensional structure of PDMS constructs. It was obtained by means of a custom-made cone-beam system called TOMOLAB (https://www.elettra.trieste.it/it/lightsources/labs-and-services/tomolab/tomolab.html). Samples were positioned onto the turn table of the instrument and acquisitions were performed with the following parameters: distance source-sample (F_{OD}), 80 mm; distance source-detector (F_{DD}), 250 mm; magnification, 3.1×; binning, 2×2; resolution, 8 μm; tomography dimensions (pixels), 2004×1335; slices dimensions (pixels), 1984×1984; number of tomographies, 1440; number of slices, 1332; E = 40 kV, I = 200 μA; exposure time, 3 s. The slices reconstruction process and the correction of beam hardening and ring artifacts were achieved by means of commercial software (Cobra Exxim). Input projections and output slices are represented by files (one file per projection and one file per slice) using arrays of 16-bit integers. BoneJ plugin [15] implemented on Fiji software [16] was used for the analysis of porosity, the dimension of pores and the thickness of pore walls. [In collaboration with Dr. Davide Porelli, University of Trieste, Italy].

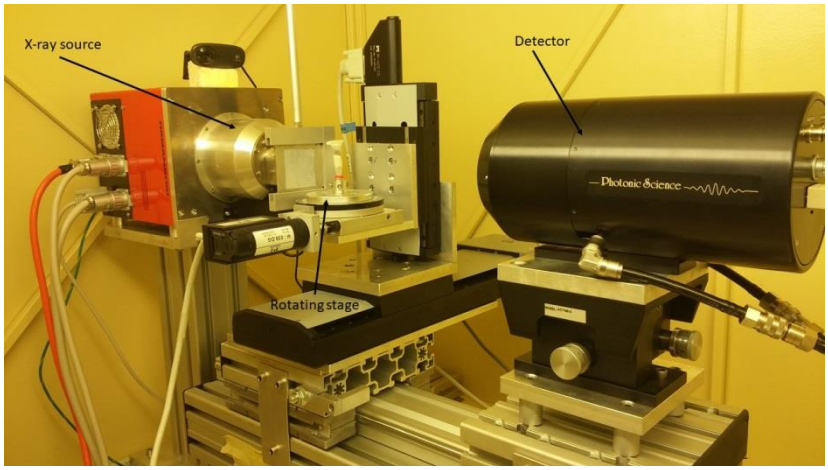

Figure 8. Custom-made cone-beam system (TOMOLAB).

Moreover, the mechanical properties of elastomeric 3D porous constructs were evaluated. In order to collect their elastic modulus, uniaxial loading tests were conducted on the samples using a Mecmesin Multitest 2.5-i. Three curves were acquired for each sample and the propagation of errors theory has been applied to acquire the elastic modulus from a linear fitting.

3.10. Preparation of primary hippocampal cultures

Primary dissociated cultures were prepared from postnatal (P2-P3) rats as previously reported [17-19]. Cells were plated on poly-L-ornithine-coated glass coverslips and on CVD grown CNT carpets. Before using for culturing, CNT substrates were mounted on the glass converslips (12×24 mm^2, 0.13–0.16 mm thick, Kindler, EU) by a thin adhesive layer of PDMS cured at 120 °C. One hour prior to plating, CVD substrates were treated with an air-plasma-cleaner in order to facilitate cell adhesion and then sterilized with an UV lamp. Cultures were incubated at 37 °C, in a humified atmosphere with 5% CO_2 in culture medium, consisting of Neurobasal Medium (Gibco), supplemented with B27 (2%; Gibco), Glutamax (10 mM; Gibco) and Gentamycin (500 nM; Gibco). Culture medium was renewed (60%) after four days from seeding. Plating was carried out at a nominal density of 200.000±16.000 cells/mL (n= 4 different series of cultures). Cultures were then used for experiments after 8÷12 days in vitro (DIV).

3.11 Organotypic cultures

The possibility to investigate the chronic (days/weeks) effect of CNT substrates on a more complex system, compared to dissociated cultures, in which the basic cytoarchitecture of the explanted organ is maintained, assumes a prominent role in this field. Therefore, we have focused our attention on organotypic Hippocampal-Entorhinal cultures (EHCs), prepared via the roller-tube technique [20-21]. Briefly, 400 μm thick entorhinal-hippocmpal slices were obtained from P6 to P8 old Wistar rats, because the Perforant Pathway is described to be fully developed from the postnatal day 6 in rats [22], by means of a tissue Chopper (McIlwain) and stored for 1h in cold (4°C) Gey's Balanced Salt Solution (GBSS, Sigma) enriched with Glucose and Kinurenic Acid to limit excitotoxic processes. The slices were then placed onto glass or CNTs supports and embedded in chicken plasma (16 μl; SIGMA), which was coagulated with the addition of a drop of thrombin (23 μl). The lesion was made by outdistancing the Entorhinal Cortex (EC) from the hippocampus 400 to 600 μm apart, by placing a millimeter graph paper below the coverslips. At this point, cultures were left 1h at RT, placed in Nunc tubes filled with 750 μl of Neurobasal-A (Thermo Fischer) medium containing B27 2% (Gibco), Glutamax 10 mM and Gentamycin 0.5 μM and then incubated at 37 °C in a roller drum rotating 10 times per hour, in (Gibco), and used for experiments at 8–10 days in vitro (DIV). The medium was completely replaced every 3 days.

3.12 Immunocytochemistry, confocal microscopy, SEM and image processing

Neuronal cells cultured on CVD grown CNT carpets and on glass controls for (8÷11 DIV) were fixed in PBS containing 4% formaldehyde for 20 min, at room temperature (RT) and then permeabilized with 1% Triton X-100 for 30 min, blocked with 5% fetal bovine serum (FBS) in PBS (blocking buffer) for 30 min at room temperature and incubated with primary antibodies for 30 min. The primary antibodies employed were: rabbit polyclonal anti-β-tubulin III (Sigma T2200, 1:250 dilution) and mouse monoclonal anti-GFAP (Sigma-Aldrich, 1:200 dilution). After the primary incubation and PBS washes, neurons were incubated for 30 min with Alexa 594 goat anti rabbit (Invitrogen, dilution 1:500), Alexa 488 goat anti mouse (Invitrogen, dilution 1:500) and with DAPI (Invitrogen, 1:200 dilution) to stain the nuclei. Samples were mounted using Vectashield (Vector Laboratories) on rectangular coverslips of 0.120 mm in thickness. Upon immunofluorescence staining, hippocampal cultures on both CNTs and glass controls were imaged using a confocal Nikon microscope (Nikon Eclipse Ti,

Nikon, Japan). The images were analyzed offline using the image-processing package Fiji [16]. Image reconstructions were performed at 20x magnification.

For SEM characterization cellular samples cultured on CNT substrates for 8÷11 DIV were washed with 0.1 M cacodylate buffer (pH = 7.2) and fixed with a solution containing 2% glutaraldehyde (Fluka, Italy) in 0.1 M cacodylate buffer for 1 h at RT. Cultures were then washed in a cacodylate buffer and dehydrated by dipping in water/ethanol solutions at progressively higher alcohol concentrations (30, 50, 70, 80, 90, 95 and 100% ethanol for 10 min each). Afterwards samples were left in 100% ethanol to dry at 4°C overnight. Prior to SEM imaging samples were gold metalized in a metal sputter coater (Polaron SC7620).

Organotypic cultures were fixed for 1h at RT in PBS containing 4% PFA. After PBS washes, cultures were incubated with mouse SMI32 (1:250) in order to stain neural processes ("crossing fibers") bridging the two parts of the lesioned slices. Cultures were then mounted with Vectashield (see above) on 1 mm thick microscope glass slides, visualized with a Confocal Microscope (see above; 10x objective) and analyzed with the Volocity Software (Perkin Elmer). To quantify the SMI32-positive "crossing-fibers", we selected a same 3D region of interest (ROI) (500 μm x 50 μm x 15 μm), between the hippocampus and the entorhinal cortex in controls and cultures grown on CNTs. The amount of SMI32- positive fibers within each ROI was quantified for each image, and normalized to the overall ROI volume, and all values for all the images from the same condition were then averaged together and plotted.

3.13 Calcium imaging, patch clamp, field potential recordings and data analysis

In order to evaluate the electrical performances of cells grown on CNTs, synthesized by employing silicon as growth substrate, calcium imaging was performed due to the lack of optical transparency of such substrates. For Ca^{2+} measurements, hippocampal cells were loaded with cell permeable Ca^{2+} dye Oregon Green 488 BAPTA I-AM (Molecular Probes). 4 mM stock solution of the Ca^{2+} dye was prepared in DMSO (Sigma-Aldrich) and hippocampal cultures were incubated with a final concentration of 4 μM for 20 min. Samples were then mounted in a recording chamber on an inverted microscope (Nikon TE-200) where they were perfused by a recording solution of the following composition (mM): 150 NaCl, 4 KCl, 2 $CaCl_2$, 1 $MgCl_2$, 10 HEPES, 10 glucose (pH adjusted to 7.4 with NaOH; osmolarity 300 mOsm) at 5 mL/min. Video microscopy and Ca^{2+}-imaging measurements were carried out at

RT. The Oregon Green loaded cultures were observed with a 40× air objective (0.8 NA, Nikon, Japan). All the recordings were taken from randomly selected visual fields. Prior to Ca^{2+} signal recording, the regions of interest were drown around cell bodies trying to include as little background as possible. Images were continuously acquired by a Till Photonics Till-Imago system, exciting the Ca^{2+}-dye with a 488 nm wavelength with a monochromator device equipped with an integrated Xenon light source (Polychrome IV, Till Photonics). Excitation light was separated from the light emitted from the sample using a 395 nm dichroic mirror and filter. Images of emitted fluorescence >480 nm were acquired at 5 Hz for 30 minutes at 200 ms exposure time per frame by a cooled slow-scan interline transfer camera (IMAGO CCD camera; Till Photonics) and simultaneously displayed on a color monitor. Camera was operated in binning mode at 60×80 pixels. The imaging system was controlled by an integrating imaging software package (TILLvisION; Till Photonics) using a personal computer. Recorded images were analyzed off-line both with Clampfit (pClamp software, 10.2 version; Axon Instruments) and Igor Pro Software (6.32A version; WaveMetrics, Lake Oswego, Oregon, USA). Intracellular Ca^{2+} transients were expressed as fractional amplitude increase ($\Delta F/F_0$, where F_0 is the baseline fluorescence level and ΔF is the rise over baseline). We determined the onset time of neuronal activation by detecting those events in the fluorescence signal that exceed at least five times the standard deviation of the noise. We then computed the difference between consecutive onset times, to obtain the inter-event interval (IEI), reciprocal of frequency. Hence, after obtaining the IEI values from each active cell in the same field, data were pooled for all fields recorded under the same experimental conditions and averaged for further comparison. Fraction of active cells per field of view was evaluated for both CNTs and controls as the ratio between the number of cells showing an electrical bursting activity and the total number of cells present in the field.

Due to the optical transparency of CNTs grown on fused silica, it was possible to compare the spontaneous activity of hippocampal neuronal networks directly grown on CNTs mat with that of control networks grown on conventional substrates (polyornithine-treated glass) by means of the patch-clamp technique, gaining a proper visualization of cells during electrophysiological recordings, otherwise impossible with CNTs grown on silicon.

Patch clamp technique, performed as previously reported [23], allows measuring the small currents (instrumental noise <1 pA), generated by neuronal cells with a small cell soma (<15 μm in diameter), such as hippocampal interneurons. For electrophysiological recordings, the

whole cell configuration was adopted. Such configuration involves the rupture of cell membrane by applying a slight negative pressure to the pipette (suction) after the first pressure, applied in turn to create a tight contact between the cell membrane and the glass pipette (inflection of the patched membrane). Whole cell recordings were achieved with glass micropipettes with a resistance of 4-7 MΩ. The intracellular pipette solution was the following (mM): 120 K gluconate, 20 KCl, 10 HEPES, 10 EGTA, 2 $MgCl_2$, 2 Na_2ATP, pH 7.3. Cultures were positioned in a custom-made chamber mounted on an inverted microscope (Eclipse TE-200, Nikon, Japan), and continuously perfused with external solution at a rate of 5 mL/min. The external saline solution contained (mM): 150 NaCl, 4 KCl, 1 MgCl2, 2 CaCl2, 10 HEPES, 10 glucose, pH 7.4. Cells were voltage clamped at a holding potential of −56 mV mV (not corrected for liquid junction potential that was calculated to be 13.7 mV at 20 °C in these experimental conditions). The uncompensated series resistance had values <8 MΩ. All recordings were performed at RT. Data were collected using a Multiclamp 700A Amplifier (Molecular Devices, US), and analyzed using Clampfit 10.4 (Molecular Devices).

Extracellular field potential co-recordings from the dentate gyrus (DG) and entorhinal cortex (EC) layers were performed on slices at 8-10 DIV at RT (20-22 °C) using low resistance (4-6 MΩ) glass micropipettes filled with extracellular solution. For each experiment, the organotypic slices, cultured on control and CNT substrates, were positioned into a recording chamber, mounted onto an upright microscope, and superfused with standard Krebs solution containing (in mM): 152 NaCl, 4 KCl, 1 $MgCl_2$, 2 $CaCl_2$,10 HEPES, and 10 glucose. The pH was adjusted to 7.4 with NaOH. A period (45') of stabilization, was followed by the recordings of the spontaneous activity (45') in standard Krebs, after which Bicuculline (30'; 10 μM) was added to the extracellular solution to weaken synaptic inhibition and induce synchronization between the two recorded areas. All recordings were performed at RT. Data were collected using a Multiclamp 700A Amplifier (Molecular Devices, US),digitized at 10kHz, and analyzed using Clampfit 10.4 (Molecular Devices). To evaluate the frequency of voltage transients, only the events with a minimum peak of three times the baseline signal were included. The CCF between each voltage pair was calculated in Clampfit 10.4 (Molecular Devices, US). The synchrony between hippocampal and entorhinal LFPs was assessed through a MATLAB custom made script, as previously described [24-25]. Briefly, for each pair of voltage time series, the Pearson correlation coefficient was assessed and its statistical significance.

All data are presented as mean ± standard deviation (SD) of the mean (n is the number of cells, if not otherwise indicated). Statistical significance was calculated using Student's-t test (value of $p < 0.05$ was accepted as indicative of statistically significant difference) for parametric data and by the Mann-Whitney U test for nonparametric data.

3.14 Preparation of porcine valve interstitial cells (pVICs)

pVICs were prepared from porcine (6–9 months) aortic valve as previously reported [26]. Cultures were then incubated at 37 °C, in a humified atmosphere with 5% CO_2 in DMEM (Thermo Fisher Scientific) culture medium, implemented with 150 U mL^{-1} penicillin/streptomycin (Sigma-Aldrich), 2 mM L-glutamine (Sigma-Aldrich) and 10% fetal bovine serum (FBS) (Sigma-Aldrich).

3.15 Immunostaining and AFM force spectroscopy

pVICs cultured on both CNT carpets and on glass controls were fixed in 4% PFA for 30 minutes at RT, permeabilized using 0.5% Tween in PBS for 10 minutes and rinsed with 0.1% Tween in PBS for three times. Subsequently, samples were blocked in 5% FBS for 1 hour and then incubated with Alexa Fluor 594 phalloidin (Thermofisher scientific, 1:10) and anti-vinculin antibody (Sigma-Aldrich, 1:20) primary antibodies in 5% FBS for 30 min and 2 hours, respectively. After the primary incubation, followed by rinsing in PBS three times for 5 min, cells were incubated for 2 hours with Alexa Fluor 488 (Thermo Fisher Scientific, 1:500) secondary antibody and with DAPI (Sigma-Aldrich, 1:3000) to stain the nuclei. Samples were mounted using Vectashield (Vector Laboratories) on circular coverslips of 0.17 mm in thickness. Upon immunofluorescence staining, pVICs on both CNTs and glass controls were imaged using an inverted microscope (Nikon Eclipse Ti-U). The images were analyzed offline using the image-processing package Fiji [17].

Moreover, the mechanical properties of cells, cultured on both glass controls and CVD-grown CNTs on fused silica, were evaluated by using Smena AFM (NT-MDT Co., Moscow, Russia) mounted on an inverted fluorescence microscope (Nikon Eclipse Ti-U). In particular, we have exploited the remarkable AFM force spectroscopy capabilities to measure the deflection of AFM cantilever while it is pushed to the surface sample which can be then interpreted and converted in a force/indentation curve via cantilever spring constant and displacement knowledge [27]. In order to determine the compliance of the analyzed material, the data were fitted with a Hertian model of surface indentation [28]. For AFM indentations the tip was

positioned roughly on cell nucleus by exploiting the possibility to visualize, during the measurements, cells cultured on glass controls as usually performed, and notably also those grown on CNTs. The optical transparency of CNTs grown on fused silica has allowed us to perform simultaneously immunofluorescence assay and cell mechanics via AFM. Cantilever adopted was a tip-less probe with a spring constant of about 0.03 nN/nm (HQ:CSC38 cantilevers from MikroMasch Co., Tallinn, Estonia) at the end of which is mounted a 20 μm in diameter silica bead (Thermo Fisher Scientific). Force spectroscopy measurements were performed at constant speed (2.5 μm/s) and the maximum force applied to the sample was 5 nN. For each sample were acquired about 60 curves. Finally, by fitting the force-displacement curves with a Hertzian model for the adopted tip was possible to estimate the elastic modulus values (kPa) by means of the NOVA (NT-MDT Co., Moscow, Russia) control and analysis software.

Statistics and data processing were performed using Igor Pro software (www.wavematrics.com) and R statistical computing software (www.R-project.org). Significance of data differences was established as equality of probability distributions via the Kolmogorov-Smirnov test.

References

[1] W. Z. Li, S. S. Xie, L. X. Qian, B. H. Chang, B. S. Zou, W. Y. Zhou, R. A. Zhao, G. Wang, *Large-Scale Synthesis of Aligned Carbon Nanotubes*. Science, 274, 1701, 1996.

[2] K. L. Kepplea, G. P. Sanbornb, P. A. Lacassea, K. M. Gruenbergc, W. J. Readyd, *Improved fracture toughness of carbon fiber composite functionalized with multi walled carbon nanotubes*, Carbon , *46*, 2026 -2033, 2008.

[3] A. L. Briseno, S. C. B. Mannsfeld, M. M. Ling, S. Liu, R. J. Tseng, C. Reese, M. E. Roberts, Y. Yang, F. Wudl, Z. Bao, *Patterning organic single-crystal transistor arrays*, Nature 444, 913–917, 2006.

[4] Y. Xia, G. M. Whitesides, *Soft Lithography*, Angew. Chem, 37, 551, 1998.

[5] P. M. Mendes, J. A. Preece, *Precision chemical engineering: integrating nanolithography and nanoassembly, Curr. Opin. Colloid Interface Sci*, 9, 236-248, 2004.

[6] J. Huang, M. Lee, J. Kim, *Selective atomic layer deposition with electron-beam patterned self-assembled monolayers*, Journal of Vacuum Science & Technology A: Vacuum, Surfaces, and Films, 30, 01A128, 2012.

[7] A. Kumar, H. A.Biebuyck, G. M. Whitesides, *Patterning Self-Assembled Monolayers: Applications in Materials Science*, Langmuir, 10, 1498-1511, 1994.

[8] J.W. Ward, B. Q. Wei, P.M. Ajayan, *Substrate effects on the growth of carbon nanotubes by thermal decomposition of methane*. Chemical Physics Letters, 376: 717–725, 2003.

[9] W. Kern, D.A. Puotinen, *Cleaning solutions based on hydrogen peroxide for use in silicon semiconductor technology*. RCA Rev. 31:187-206, 1970.

[10] C. Py, M. W. Denhoff, M. Martina, R. Monette, T. Comas, T. Ahuja, D. Martinez, S. Wingar, J. Caballero,S. Laframboise, J. Mielke, A. Bogdanov, C. Luk, N. Syed, G. Mealing, *A Novel Silicon Patch-Clamp Chip Permits High-Fidelity Recording of Ion Channel Activity From Functionally Defined Neurons*, Biotechnology and Bioengineering, Vol. 107, No. 4, 2010.

[11] V. V. Korol'Kov, B. Kibak, *Sintering mechanism of iron powder with microadditions of boron*, Powder Metallurgy and Metal Ceramics, 36, 9-10, 1997.

[12] L. F. Pease. *Metallography and Microstructures of Powder Metallurgy Alloys*. Metallography and Microstructures of Powder Metallurgy Alloys, Metallography and Microstructures, Vol 9, ASM Handbook, pp. 994–1020, 2004.

[13] J. W. Han, B. Kim, J. Li, M. Meyyappan, *Flexible, compressible, hydrophobic, floatable, and conductive carbon nanotube-polymer sponge.* Applied physics letters 102, 0519031–0519034, 2013.

[14] P. Klapetek., M. Valtr, D. Nečas, O. Salyk, P. Dzik, *Atomic force microscopy analysis of nanoparticles in non-ideal conditions*, Nanoscale Res. Lett, 6, 514, 2011.

[15] M. Doube, M. M. Kłosowski, I. Arganda-Carreras, F.P. Cordelières, R.P. Dougherty, J. S. Jackson, B. Schmid, J. R. Hutchinson, S. J. Shefelbine, *BoneJ: Free and extensible bone image analysis in ImageJ*, Bone 47 (6): 1076-1079, 2010.

[16] J. Schindelin, I. Arganda-Carreras, E. Frise, *Fiji: an open-source platform for biological-image analysis*, Nature methods 9 (7): 676-682, 2012.

[17] G. Cellot, E. Cilia, S. Cipollone, V. Rancic, A. Sucapane, S. Giordani, L. Gambazzi, H. Markram, M. Grandolfo, D. Scaini, F. Gelain, L. Casalis, M. Prato, M. Giugliano, L. Ballerini, *Carbon nanotubes might improve neuronal performance by favouring electrical shortcuts* Nat Nanotechnol. 2, 126, 2009.

[18] S. Bosi, R. Rauti, J. Laishram, A. Turco, D. Lonardoni, T. Nieus, M. Prato, D. Scaini, L. Ballerini, *From 2D to 3D: novel nanostructured scaffolds to investigate signalling in reconstructed neuronal networks*, Sci Rep. *5*, 9562, 2015.

[19] R. Rauti, N. Lozano, V. León, D. Scaini, M. Musto, I. Rago, F. P. Ulloa Severino, A. Fabbro, L. Casalis, E. Vázquez, K. Kostarelos, M. Prato, L. Ballerini, *Graphene Oxide*

Nanosheets Reshape Synaptic Function in Cultured Brain Networks ACS Nano. 10, 4459, 2016.

[20] B. H. Gähwiler, *Organotypic cultures of neural tissue*, Trends in Neuroscience 11 (11) 484-489, 1988.

[21] M. H. Mohajerani, E. Cherubini, *Spontaneous recurrent network activity in organotypic rat hippocampal slices*, Eur J Neurosci, 22:107-118, 2005.

[22] R. Fricke, W. M. Cowan, *An autoradiographic study of the development of the entorhinal and commissural afferents to the dentate gyrus of the rat*. J Comp Neurol. 15;173(2):231-50, 1977.

[23] B. Sackmann, E. Neher, *Patch clamp techniques for studying ionic channel in excitable membranes*. *Annu Rev Physiol* 46: 455-72, 1984.

[24] S. Usmani, E. R. Aurand, M. Medelin, A. Fabbro, D. Scaini, J. Laishram, F. B. Rosselli, A. Ansuini, D.Zoccolan, M. Scarselli, M. De Crescenzi, S. Bosi, M. Prato, L. Ballerini. *3D meshes of carbon nanotubes guide functional reconnection of segregated spinal explants*. Sci Adv. 2(7): e1600087, 2016.

[25] E. R. Aurand, S. Usmani, M. Medelin, D. Scaini, S. Bosi S, F. B. Rosselli, S. Donato, G. Tromba, M. Prato, L. Ballerini, *Nanostructures to Engineer 3D Neural-Interfaces: Directing Axonal Navigation toward Successful Bridging of Spinal Segments*. Adv funct Mat 1, 1700550-62, 2017.

[26] R. Santoro, F. Consolo, M. Spiccia, M. Piola, S. Kassem, F. Prandi, M. C. Vinci, E. Forti, G. Polvani, G. B. Fiore, M. Soncini, M. Pesce. *Feasibility of Pig and Human-Derived Aortic Valve Interstitial Cells Seeding on Fixative-Free Decellularized Animal Pericardium*. J. Biomed. Mater. Res. - Part B Appl. Biomater, 104, 345–356, 2016.

[27] J. L. Alonso, 202 W. H. Goldmann, *Feeling the forces: atomic force microscopy in cell biology,* Life Sci. 72, 203 2553e2560, 2003.

[28] I. N. Sneddon, *The relation between load and penetration in the axisymmetric boussinesq problem for a punch of arbitrary profile,* Int. J. Eng. Sci. 3, 47e57, 1965.

4. Results and discussion

The focal objective of this thesis was to develop and fabricate novel nano- and micro-structured materials having biomimetic design features in order to investigate the effect such novel materials have on cells cultured above (or inside) them. The final purpose is to create reliable procedures to control cellular functionalities and properties (i.e. neuronal communication or cellular mechanobiology). In particular, in order to reach this goal, I have designed, fabricated and extensively characterized various CNTs-based substrates subsequently used to study their effect on hippocampal neuronal networks and on the onset of calcific aortic valve disease. An additional area of this work is related to the realization and characterization of 3D micro-porous constructs, both CNTs- and elastomeric-based.

In the following sections, the main achievements reached in each of the above-mentioned parts are described.

4.1 Effects of CNTs directly grown on supporting surfaces on hippocampal neuronal networks

As deeply described in Chapter 1, many studies have revealed distinctive CNTs ability to perturb/potentiate neural electrical performances, probably thanks to their outstanding electrical properties and nanometric dimensional scale giving rise to an intimate contact with cell membranes [1-4]. Such findings have highlighted the potential role of these smart nanostructures in neuroscience. In previous works, aimed to investigate the interaction between cells and carbon nanotubes, purified MWCNTs deposited on supporting substrates via drop casting, were mostly employed [1]. Briefly, MWCNTs were functionalized using the 1,3-dipolar cycloaddition of azomethine ylides resulting in a functionalization with pyrrolidine groups on the nanotube tips and sidewalls. Such chemical modification significantly increases their solubility in organic solvents. The as-prepared nanotubes were then dissolved in dimethylformamide (DMF). A small amount of the so obtained homogeneous CNTs-based solution was deposited on a glass coverslips. After solvent evaporation, a de-functionalization was performed via a thermal treatment conducted in an oven a 350 °C under nitrogen atmosphere for 15 min. Although the positive impact of such substrates on neural cultures, it is important to point out the limits related to drop-casting technique, such as poor density and low uniformity of carbon nanotubes on the underneath glass substrate, clearly detectable in Figure 1. Moreover, another limiting issue is that CNTs

did not adhere properly to glass. Therefore, during neurite outgrowth, especially when organotypic slices are used, they can detach from the substrate and even float in the culture medium. In order to overcome such problems, that will cause as well CNT-related toxicity phenomena, we chose to follow another approach consisting in the growth of CNTs directly on a supporting silicon surface by CCVD technique (see Methods).

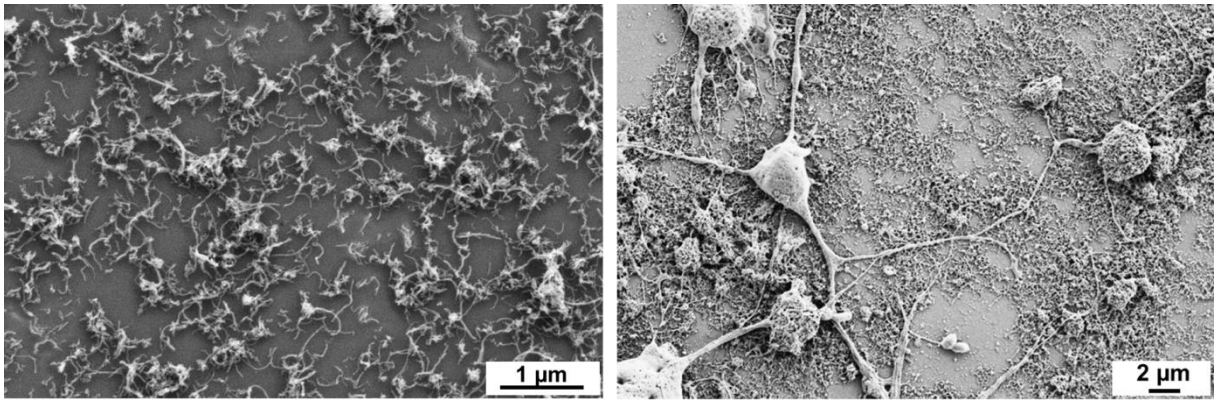

Figure 1. SEM image of drop-casted CNTs interfaced (right) or not (left) with neural network, highlighting the main issues related to drop-casting (i.e. poor CNTs uniformity and density).

We have adopted an interdisciplinary approach to address the structural and functional changes occurring in a novel nano-biohybrid system consisting of neurons developed on CVD grown CNTs carpets. To pursue this aim, I have developed artificial CVD grown culturing substrates. Our results have revealed, for the first time, that dissociated hippocampal cultures, grown on such chemical-vapor deposited substrates, give rise to a healthy hybrid system and, moreover, the functional neuronal network resulting is characterized by a potentiated electrical activity when compared to a neuronal network developed on control glass surfaces. In addition, the high versatility of our synthesis method allows realizing patterned CNTs of potentially any arbitrary shape, otherwise extremely difficult to be obtained with the previous drop-casting approaches.

4.1.1 CNTs synthesis and characterization

I have synthesized carbon nanotubes on silicon wafer chips (SiO_2/Si) substrates following an iron nanoparticle-catalyzed chemical vapor deposition (CCVD) process and carrying out the growth for just 90 sec (see Methods). At elevated temperature, it is well known in the literature that a direct coating of catalyst on Si substrate can induce catalyst silicide formation,

which in turn can deactivate the catalyst that is fundamental for nanotubes growth. In fact, in our synthesis process, catalyst film thickness plays a crucial role, because CNTs growth originate from the iron nanoparticles, formed during a subsequent thermal annealing treatment, and act as a sort of "template" for the CNTs growth [5]. Size and density of the catalyst nanoparticles covering the supporting substrate are controlled by the annealing thermal treatment parameters (i.e. temperature and time) and by the thickness and adhesion of the initial iron layer [6]. Therefore, it is fundamental to preserve catalyst nanoparticles, avoiding the silicidation of the metal catalyst. To this aim, buffer layers, such as thermally grown SiO_2, Al_2O_3, and TiO_2, were previously adopted [7-8]. Moreover, in order to enhance nanotube yields, two [9-10] or even more catalyst layers were employed [11-12]. Notably, in our CCVD synthesis method, no metal other than iron has been used as catalyst layer and no other buffer layer, besides the native SiO_2 covering the whole Si wafer upon contact with atmospheric oxygen, has been employed. Although these peculiar conditions, the as-produced CNT carpets possess the same features of carbon nanostructures produced by using more time-consuming techniques (see material characterization section). Such peculiarities of our laboratory-scaled process, together with its inexpensiveness make it an extremely interesting substrate model for research purposes.

Based on the important role that catalyst particles play, I have investigated via atomic force microscopy (AFM) the surface morphology of the catalyst layer (Fe-coated SiO_2/Si substrate) together with the formation and the size distribution of Fe nanoparticles on the supporting substrate, before and after the annealing treatment. The AFM characterization of the catalyst layer (i.e. iron as thin film) has been central in the perspective to optimize the synthesis of CNTs-based substrate. In particular, I have tested, and subsequently characterized via AFM, various thickness of iron catalyst layer and various annealing thermal treatment parameters (i.e. time, temperature and partial pressure) (Data not shown) in order to individuate the best conditions leading to the realization of CNT carpets characterized by the desired features in terms of tube's diameter, density and orientation. Thus proceeding, the optimal conditions for our purpose were found in a catalyst layer thickness ranging between 2 and 5 nm and an annealing thermal treatment performed at ~670 °C in H_2 atmosphere **(**up to a partial pressure of $3 \cdot 10^{-1}$ mbar) for 4 min (See Methods for more details).

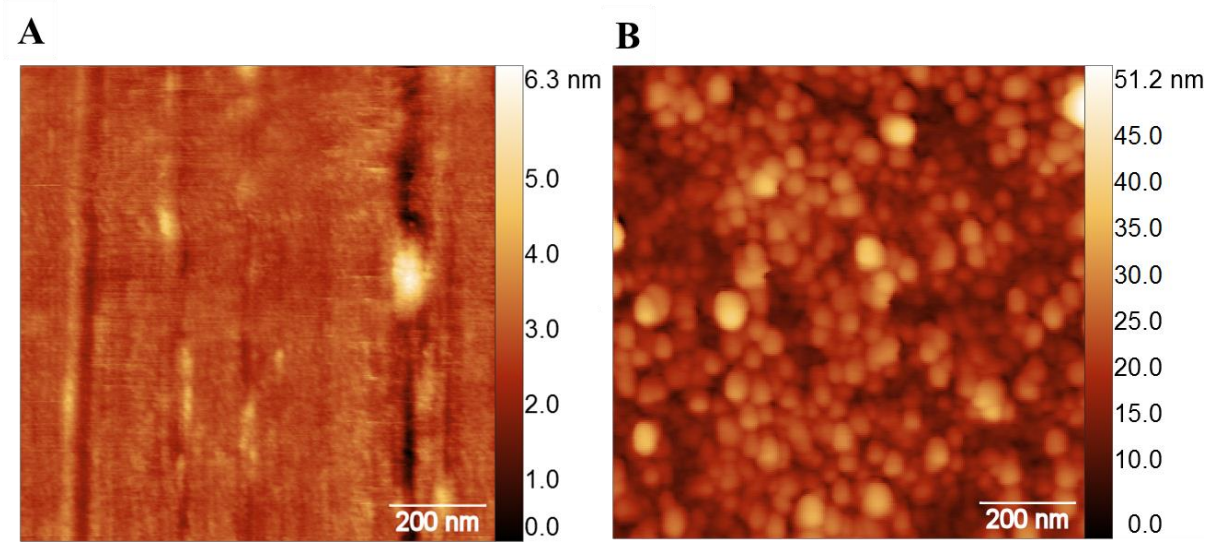

Figure 2. AFM topography images of as-evaporated (A) and successively annealed (B) Fe (~2 nm) film on SiO_2/Si substrate. The catalyst films were annealed at 670 °C in H_2 atmosphere (up to a partial pressure of $3 \cdot 10^{-1}$mbar) for 4 min.

Figure 2 shows typical AFM micrographs of an as-evaporated ~2 nm iron film before (Figure 2A) and after (Figure 2B) the thermal treatment. Prior to annealing, Fe films have been found relatively smooth and with a root-mean-square (rms) surface roughness (mediated over three samples) of about 0.37±0.06 nm; on the other hand, after the annealing pre-treatment, a completely different surface morphology characterized by a dramatic increase in the rms roughness (5.3±0.19 nm) was observed (see Figure 2). The nucleation of particles, acting as growth seeds, is driven by a minimization of the surface free energies and the difference in surface energy between the metal catalyst and the supporting layer [13-15].

Once optimal catalyst film thickness and annealing treatment parameters were established, the growth of CNTs was conducted via CCVD process by cracking of acetylene as hydrocarbon source gas over the as-formed iron nanoparticles (see Methods).

After CNT carpets synthesis, an extensive material characterization was performed in order to explore and ensure their structure, purity, and reliability. As the first step, I have performed FE-SEM imaging on the as-obtained carbon nanostructures in order to address their diameter, alignment, uniformity and density. SEM analysis revealed that as-grown nanotubes have diameters ranging between 15 nm and 25 nm and lengths up to 300 μm. It is worth noting that CNTs diameter is strongly related to catalyst particle size [16], while CNTs length depends on the growth time [17]. Analysis of side view SEM micrographs (Figure 3A, inlet B) reveals

vertical aligned CNTs, oriented perpendicularly to the surface substrate, with a very high packing density forcing their vertical orientation. Instead, in the top view CNTs appear randomly oriented (Figure 3A, inlet C) due to the proximity effect of densely distributed catalyst nanoparticles forcing initially randomly oriented CNTs into a vertical alignment [18]. In particular, the reason of this intriguing phenomenon could be ascribed to the following mechanism: when acetylene (hydrocarbon source gas) comes into contact with the "hot" metal nanoparticles (after the annealing treatment), starts to crack. In this initial phase, a layer of few and random distributed CNTs initiates the growth without any preferential directionality. As soon as CNTs density increases, van der Waals forces between adjacent nanotubes direct their vertical growth [19].

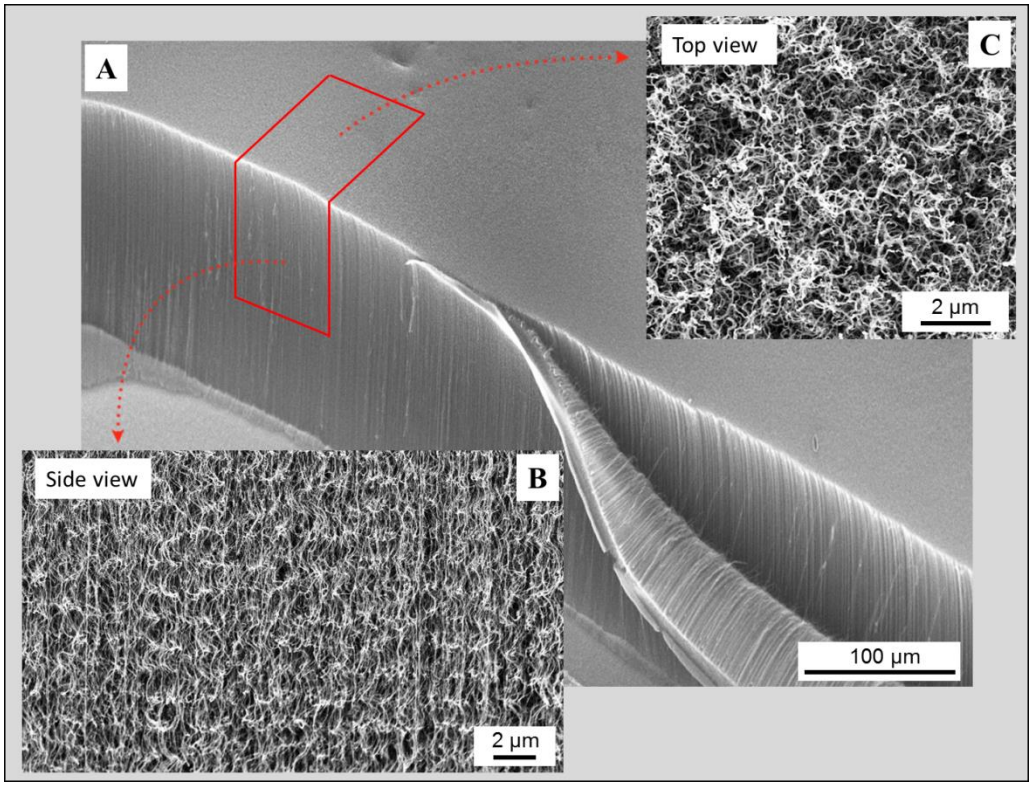

Figure 3. Side view FE-SEM image (A and inlet B) revealing the vertical alignment of CNTs perpendicularly to the underneath SiO_2/Si substrate. Conversely, in the top view CNTs are randomly oriented.

A typical top-view SEM image of our CNT substrates is shown in Figure 4 pointing out not only their superficial "bush like" conformation, but also that CNTs surface coverage is extremely homogeneous and, differently from the case of drop-casted CNTs, no empty areas exposing the underneath silicon surface are present. To note, by further increasing the

magnification, no metallic residual were found on CNTs carpet surface (Figure 4, C and D), thus suggesting that nanotube grow up with the catalyst particle rooted on its base (base-growth model, see Chapter 2) [6]. Such observation is very suitable in the perspective to adopt these substrates as (bio)scaffolds for cellular development, in particular dealing with fragile cells as primary cultures.

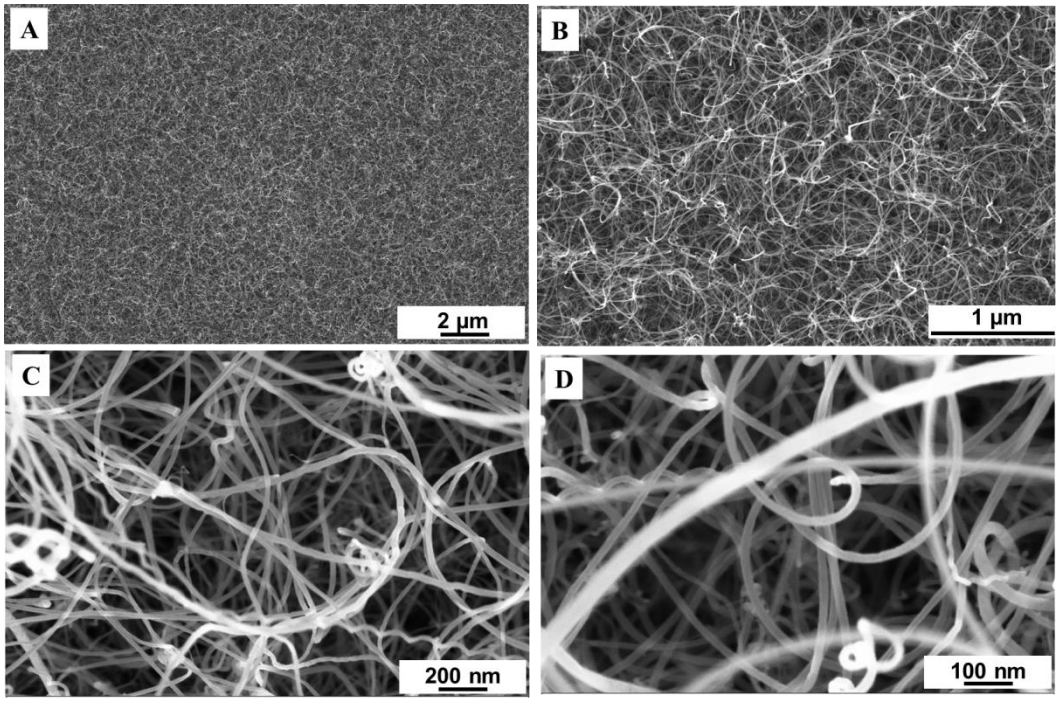

Figure 4. Top-view SEM images of CVD-grown CNTs at increasing magnifications.

Such peculiar features of CVD-grown CNTs (i.e. high density, good uniformity, strong adhesion to the underlying substrate since there are directly grown on it) allow us to speculate that with our synthesis method the issues related to drop-casting technique, described before, can be overcome. Figure 5, by comparing SEM images of CVD-grown and drop-casted carbon nanotubes, highlights the huge increase in density and uniformity obtained following our CNTs synthesis procedure. In addition, I have investigated, via AFM, the surface topography of CNTs which has been found to have a surface rms roughness (mediated over four samples) of 93.2±16.7 nm. Figure 6A is a representative AFM micrograph of our CNT carpets revealing an entangled fractal-like structure of nanotubes, deriving from the randomly oriented terminal part of the nanotubes, resembling the ECM in terms of general organization and dimensions which are comparable to fibril extracellular matrix (ECM) constituents [20] (Figure 6, B and C).

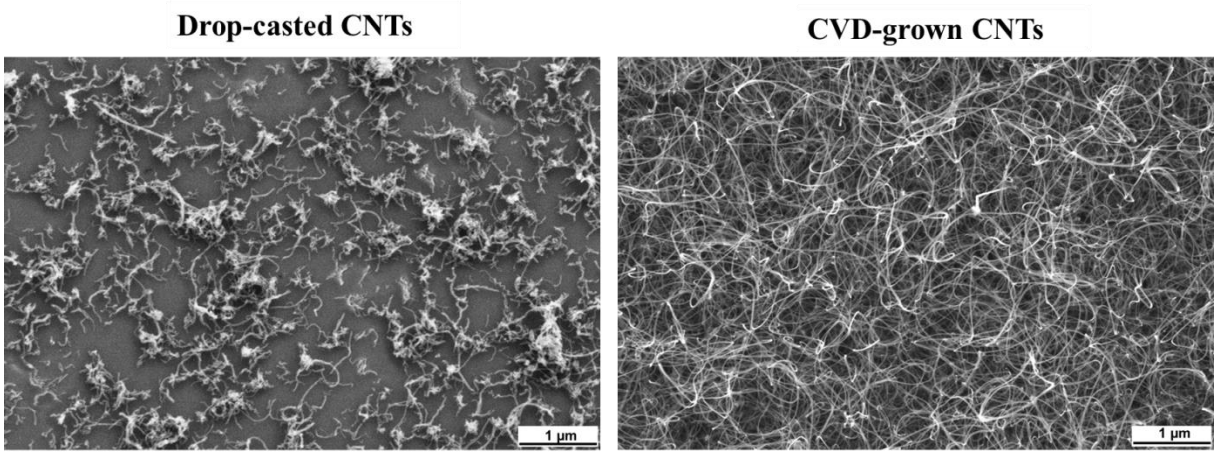

Figure 5. Comparison between top-view SEM images of drop-casted and CVD-grown CNTs revealing the increased density and uniformity of nanotubes in the second case.

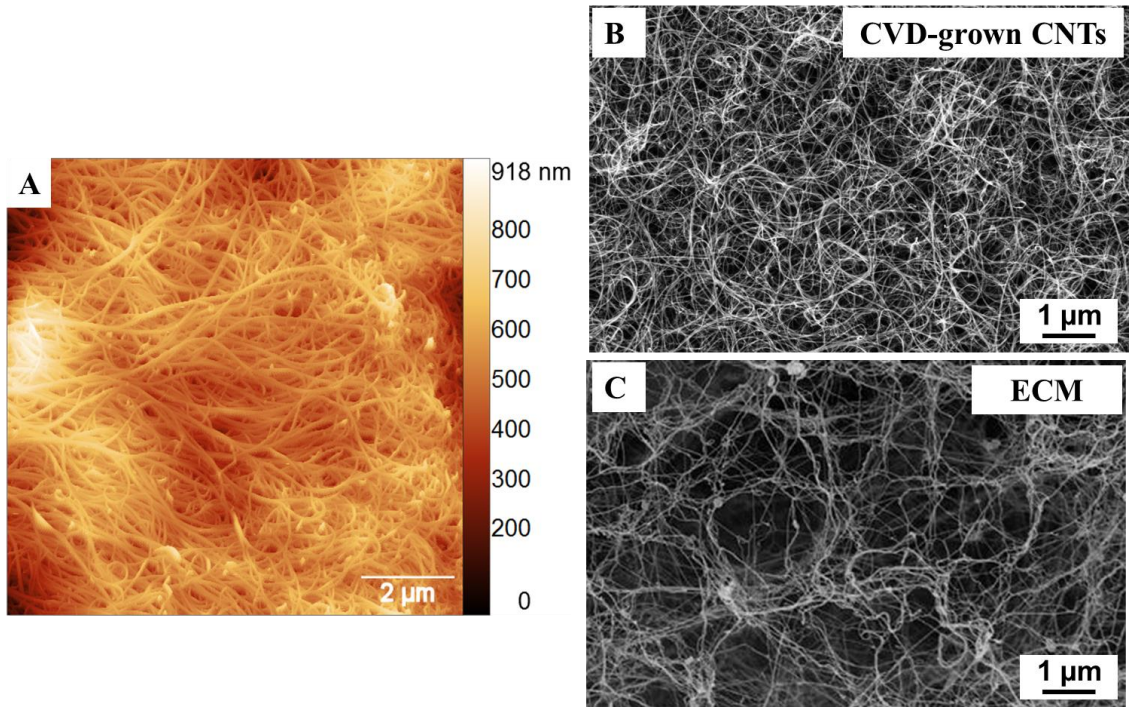

Figure 6. (A) Typical AFM topography micrograph of CNT carpets. Measurements were carried out in air at room temperature working in non-contact mode. Cantilevers, characterized by a resonant frequency of about 65 KHz (MikroMasch HQ:NSC36/NO AL) were used. (B-C) SEM images highlighting the similarities in terms of micro- and nano-morphology between our CVD-grown CNTs (B) and ECM derived from bovine cotyledons after decellularization (C) [Image (C) from *Barreto et al. 2017*].

TEM analysis was done to determine CNTs structure and crystallinity, the catalyst particles size and their localization along the tubes. It has been found that CNTs consist of multi-walled nanotubes with different wall number. Specifically, Figure 7A, left, shows an isolated

MWCNT with an outer diameter (OD) of less than 22 nm and an inner diameter (ID) of nearly 12 nm. These measurements are consistent with MWCNT of about 14 walls. In addition, TEM observations reveal only a partial encapsulation of Fe particles into tubes and, as a matter of fact, their localization at one end of different nanotubes was verified. Nanoparticles diameter coincided with MWCNTs inner diameter confirming the theory for which catalyst particle size determines tube diameter [21]. Figure 7B, right, reveals a 24 nm catalyst nanoparticle (highlighted in the red ellipsis) standing inside the endcap of a nanotube probably due to a subsequent growth, via bulk diffusion of carbon atoms into the nanoparticle, after the growth of the outer walls (See Chapter 2) [6]. The same micrograph showed several overlapping CNTs with diameters ranging from 8 to 22 nm.

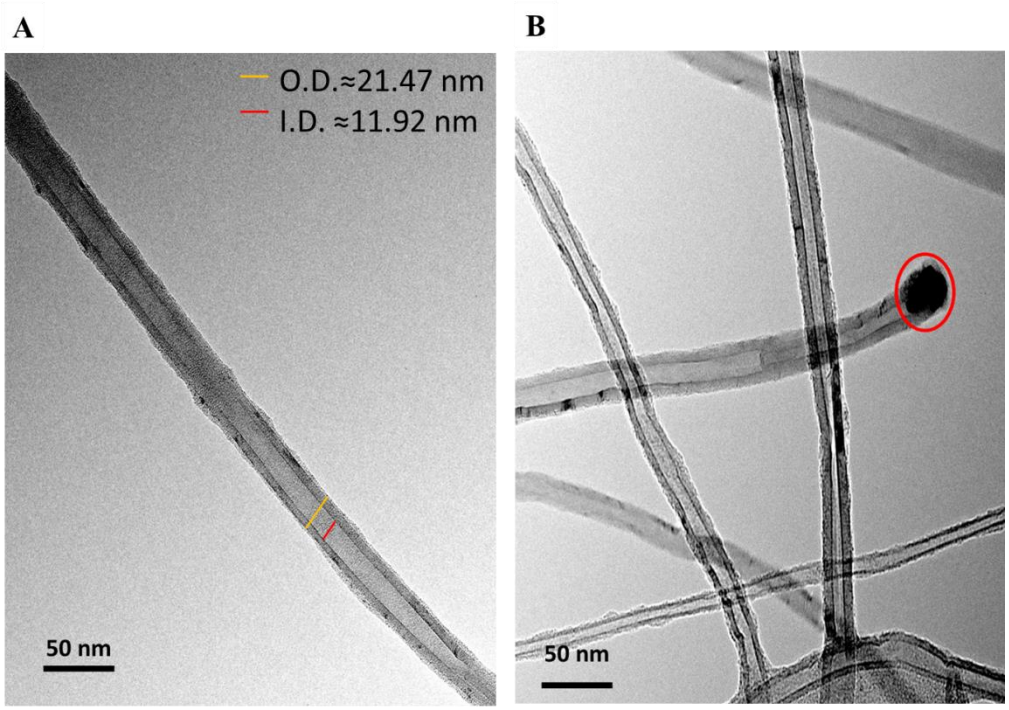

Figure 7. TEM images of CVD grown CNTs. (A) An isolated MWCNT characterized by an outer diameter (OD) of ~21.47 nm and an inner diameter (ID) of nearly ~11.92 nm. (B) Various overlapping CNTs. [In collaboration with Dr. Paolo Bertoncin, TEM facility of the University of Trieste, Italy].

Nevertheless, TEM analysis pointed out that CNTs exhibit structural defects along their length (darker regions on the side wall, Figure 7, A and B), generally imperfections of conjugated sp^2 carbon along the tubes, such as breaks, dangling bonds due to the presence of sp^3 carbon atoms, Thrower-Stone-Wales defects (i.e., two heptagons and two pentagons). All these imperfections are probably related to the low reaction temperature of the CNTs

synthesis process [22-23]. An example of wall defect, found in our CNTs, is presented in Figure 8. Such structural defect could be explained through the presence of pentagon on one side of the tube and a heptagon on the opposite side and can also determine chirality and tube diameter changes before and after the kink [21].

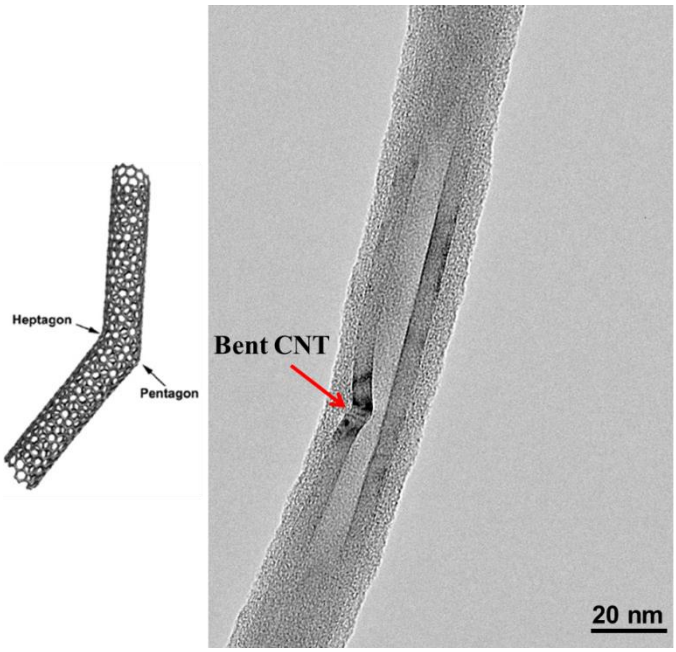

Figure 8. TEM image (right) and molecular model of a bent nanotube created by adding a pentagon–heptagon pair (left) [21]. [In collaboration with Dr. Paolo Bertoncin, TEM facility of the University of Trieste, Italy].

Moreover, Raman spectroscopy analysis was performed to investigate the purity, the degree of structural ordering combined with the possibility to discriminate MWCNTs from other carbon allotropes. Such spectroscopic technique has been very useful to describe the structural properties of SWNTs [24]. However, since much less works have been devoted to the interpretation of MWCNTs Raman spectra, in order to understand the experimental spectra from these multi-walled CNTs, we exploited and translated the well-established achievements reached for SWCNTs [21]. The first- and second-order Raman spectra recorded on the as-grown CNTs (Figure 9) revealed MWCNT characteristic peaks with a D band at ~1330 cm^{-1} and a G band at ~1583 cm^{-1}[25-26].

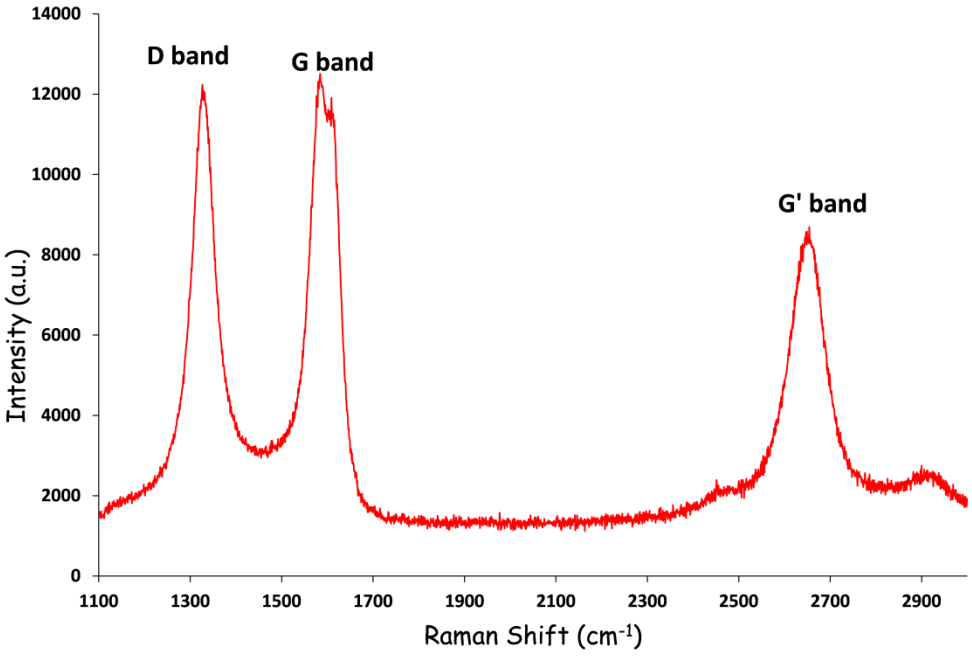

Figure 9. Raman spectra exhibiting typical bands of low temperature CVD grown CNTs. [In collaboration with Prof. Alois Bonifacio, University of Trieste, Italy]

The D band is a dispersive second order Raman peak. Therefore, its position changes depending on the laser energy: by varying the laser energy by 1 eV, a shift of approximately 53 cm^{-1} was found [27]. D peaks are also called defective, because they are related to disorder-induced features, such as amorphous and/or disordered carbon structure [28]. To note, an *in situ* Raman spectroscopy analysis of double-walled carbon nanotubes (DWCNTs), conducted during an oxidation treatment, revealed a total disappearance of the D band, suggesting that such band is not an intrinsic characteristic of the tube (defects in the tube walls), but originate from amorphous carbon [29]. The G band arises from the in-plane tangential vibration of sp^2-hybridized carbon atoms within the graphene sheets, due to the graphitic nature of CNTs. It is a non-dispersive peak and its sharpness increase with the degree of material crystallinity [27, 30].

The ratio between D (I_D) and G (I_G) bands integral intensities was generally exploited to evaluate the quality of MWCNTs. Specifically, similar intensities of these bands [30], as in our case, suggested the presence of non-graphitic carbon in nanotubes, typical of low temperature CVD-grown CNTs [31-32]. Together with the G band, the second-order Raman peak G' is a signature of graphitic sp^2 materials and is located at about 2700 cm^{-1}. The G'

band, an overtone mode of the D band [33], is associated with defect density, but not as crucially as the first order mode. It was proposed to adopt the $I_{G'}/I_G$ ratio as an additional parameter to evaluate the quality of CNTs: a high degree of crystallinity is given by a ratio approaching the unity, while a value nearly 0.2 is distinctive of very defective MWCNTs [32]. Additionally, Kim and coworkers, in 2007, have reported that the intensity of this peak depends significantly on the metallicity of CNTs [34]. Additionally, XPS analysis was carried out in order to determine CNTs surface composition. XPS survey spectrum of CNTs (Figure 10, left) pointed out three elements clearly distinguishable: carbon (C1s), oxygen (O1s) and silicon (Si2s, 2p). The amount of C and O are 87.29% and 8.90%, respectively. Moreover, a small amount (3.8%) of Si was detected suggesting a good CNTs coverage of the growth-substrate. Importantly, no metallic residual were found on CNTs surface, as confirmed by SEM characterization. The most intense peaks, shown in the C1s core level (Figure 10, right), located at 284.6 eV and 285.8 eV can be assigned to sp^2-hybridized graphitic carbon atoms on CNTs walls and to amorphous carbon (sp^3-hybridized carbon atoms), respectively [35]. The amorphous carbon is likely due to the CNTs synthesis process, as confirmed by the structural defects identified via TEM (Figure 7 and 8) and Raman spectroscopy D (Figure 9). The peak at 290.8 eV corresponds to the electron energy loss peak due to π-plasmon excitations. These three peaks are characteristics of C1s core level from CNTs [36]. The additional small peaks at 287.15 eV and 288.4 eV are related to the presence of oxygen on CNTs surface [37].

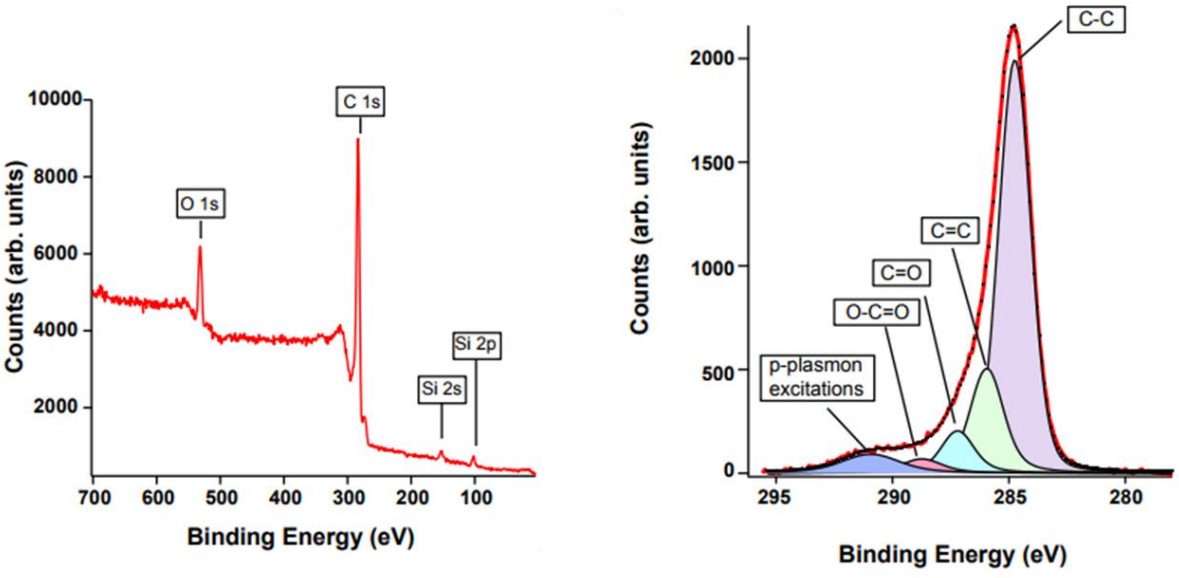

Figure 10. XPS survey (left) and C1s core level (right) of CVD grown CNTs. [In collaboration with Matteo Dalmiglio, ELETTRA Synchrotron Light Source, Trieste, Italy].

Notably, due to the exceptionally high versatility of our synthesis method, it is possible to decorate a surface with a CNTs-based carpet of potentially any arbitrary shape on specific sites simply by patterning the catalyst layer above the supporting substrate. I have adopted a non-lithographic patterning method, named microcontact printing (μCP), involving octadecyltrichlorosilane (OTS) molecules (see Methods) to direct site-selective growth of CNTs obtaining, in this way, reproducible and large-scale CNTs micrometric patterns of various geometries (Figure 11). Usually, patterned microstructures were fabricated after the deposition of a continuous film across the entire surface of a substrate, involving complex lithographic procedures and chemical or reactive ion etching of the undesired materials by the so called subtractive pattern generation process [38]. Compared to conventional subtractive patterning methods, our approach reduces process steps, costs and chemical wastes enabling a more rapid fabrication of microstructures with a resolution comparable of similar patterns realized with traditional lithographic strategies, but at a fraction of the cost and time.

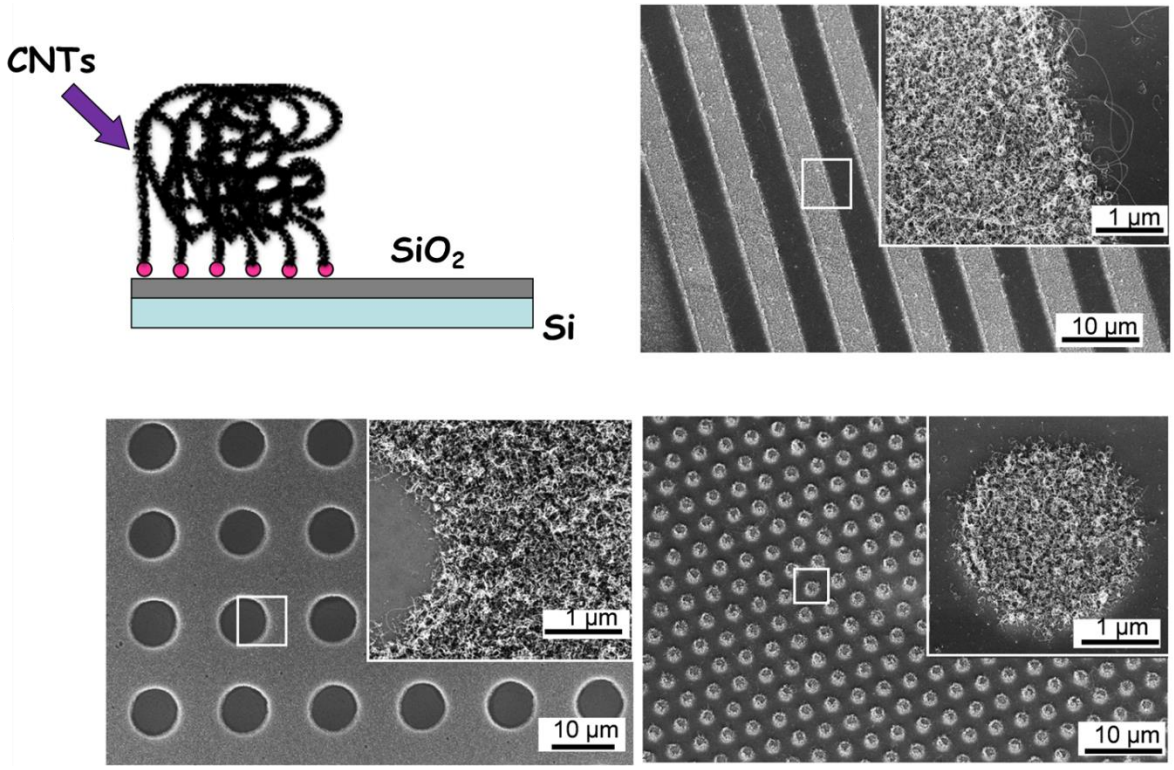

Figure 11. SEM images showing various micro-patterned geometries realized with CNTs.

Moreover, our CCVD synthesis method allows the fine control of CNTs length (i.e. the CNTs forest's thickness) by acting on the growth time: the time of interaction between acetylene (hydrocarbon source gas) and metal active nanoparticles (after the thermal annealing

treatment) (See Methods). Indeed, starting from the same geometry (CNTs-based dots, Figure 12A), a growth time of 4 min led to a CNTs length of about 45 µm (Figure 12B) while, by increasing the reaction time to 10 min, the CNTs length can be enhanced up to about 200 µm (Figure 12C).

As described in Chapter 1, the geometry of the scaffold is crucial in neural regeneration. Accordingly, our patterned CNTs substrates could be exploited as smart tools to spatially direct neurite (re)-growth [39-40]. In fact, the introduction of longitudinal tubular constructs (Figure 12C) could, for example, provide physical guidance for axonal regrowth and cell migration, and thus may enhance nerve regeneration. While, shorter CNTs (Figure 12B) could be adopted, thanks to their mechanical strength, as micrometric wells able to trap seeded cells or, alternatively, as supporting/sustaining matrices for regeneration of damaged or weakened tissues [41].

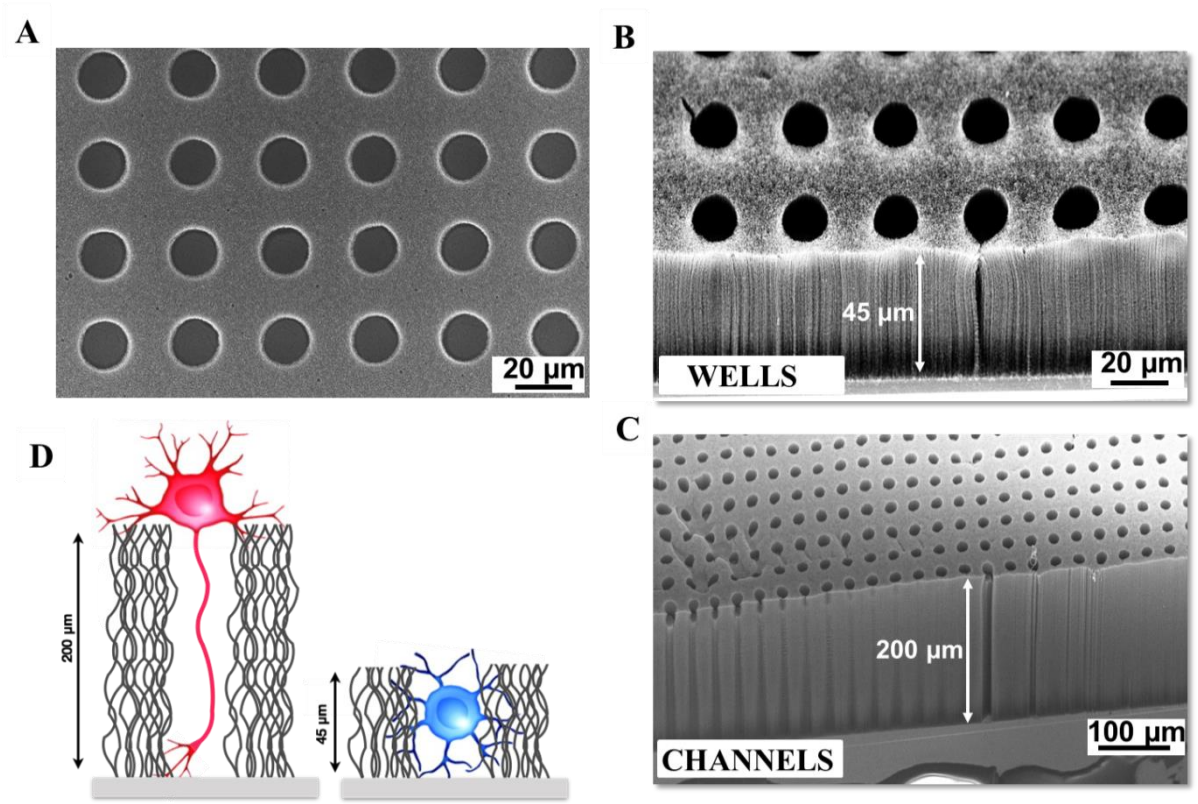

Figure 12. SEM images of CNTs-based dots characterized by different thickness controlled by varying the growth from 4 min (B) to 10 min (C). In (D) a representative sketch of CNTs-based scaffolds which could be employed as channel to direct neurite (re)-growth (left) or wells to trap seeded cells (right).

4.1.2 Development of primary neurons on CNTs substrates

In this set of experiments, we have used immunofluorescence technique to compare cells grown on control glass with those grown on a continuous carpet of our CNTs. To verify the *in-vitro* formation of a hippocampal network on the CNTs substrates, we have marked by means of immunofluorescence the neuronal-specific cytoskeletal components β-tubulin III selectively visualizing, in this way, neurons, and the glial fibrillary acidic proteins (GFAP) to visualize neuroglia [42-44]. Figure 13A shows confocal reconstructions where cultures display β-tubulin III positive cells (in red) developed above traditional control glass coverslips (left panel) or above our novel CNTs substrates (right). In both images cell nuclei were pointed out by DAPI staining (in blue).

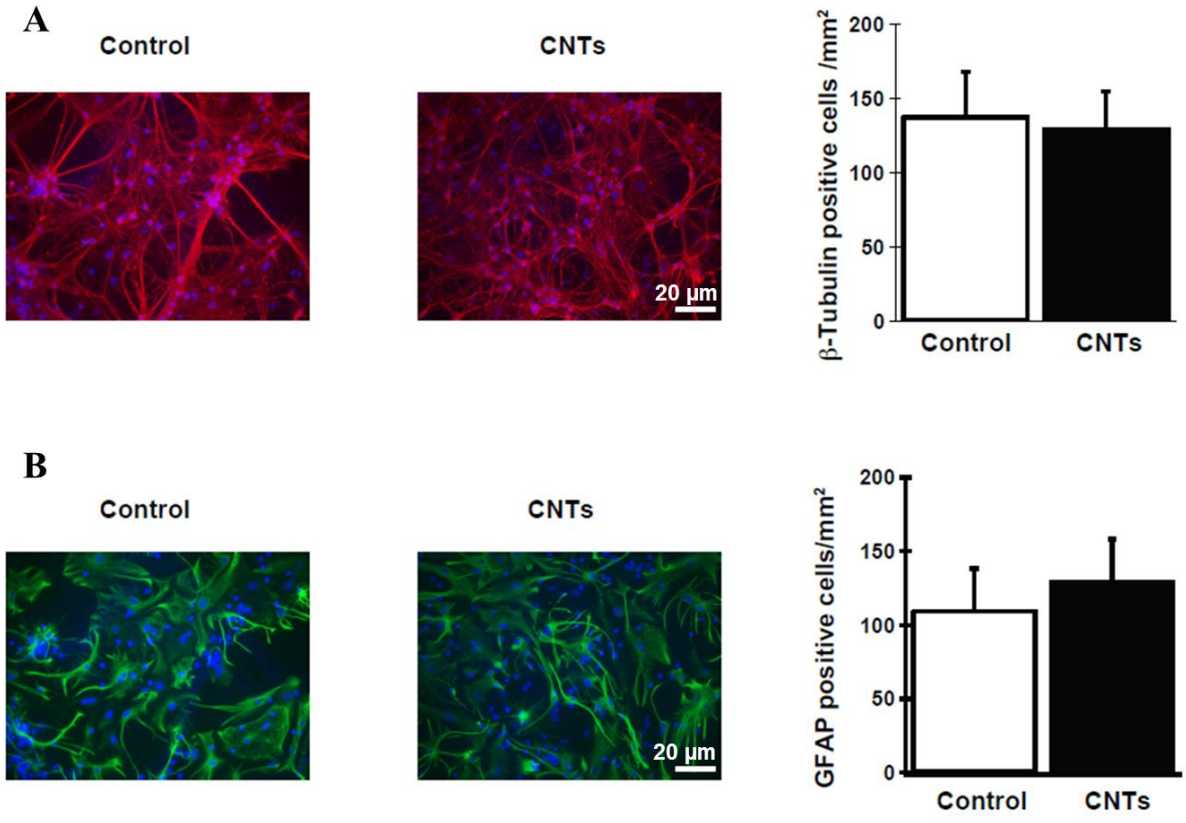

Figure 13. Immunofluorescence images showing neurons (β-tubulin III, red) and glial cells glial (fibrillary acidic protein (GFAP)**,** green) in the two analyzed conditions (control glass coverslips (left panel) or in CNTs substrates (right); in all, nuclei are visualized by DAPI in blue). The plots summarize neuronal (A) and glial (B) densities in all conditions [In collaboration with Dr. Rossana Rauti, SISSA, Trieste, Italy].

Summarizing the results, CNTs presence did not affect neuronal density (Figure 13A, right histogram; n=10 visual field per condition, three different culture series). Control cultures present a neuronal density of 138±30 β-tubulin-positive cells per mm^2 that was comparable with that measured in CNTs ones (130±25 β-tubulin-positive cells per mm^2). Subsequently, we have explored the presence and morphology of glial cells. GFAP is the main component of the astrocyte intermediate filament cytoskeleton and its expression increases as the cell matures [45]. These cells are characterized by a stellate-like morphology (see confocal reconstructions in Figure 13B) and we have measured their density both in control and CNTs samples. Again, CNTs did not affect astrocytes density (Figure 13B, right histogram; n=10 visual field per condition, three different culture series). Control cultures present a glial density of 110±28 GFAP-positive cells per mm^2 that was comparable with that measured in CNTs ones (130±28 GFAP-positive cells per mm^2).

Moreover, hippocampal network growth, morphology and adhesion to CNT mats, were assessed by SEM analysis. As shown in Figure 14, neurons adhere closely to CNTs extending their neurites and creating exceptional intimate contacts with them. An ECM poor region of the sample (highlighted by the red square in Figure 14, right) was visualized at an increased magnification (Figure 14, right) clearly pointing out the presence of the underlying CNT carpet and the tight contact between it and neuronal cells (red arrows).

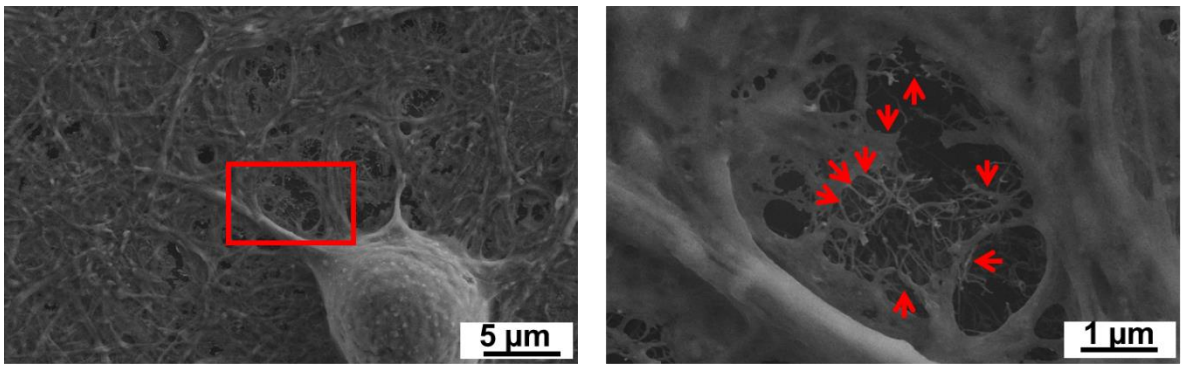

Figure 14 Postnatal hippocampal neuron cultured on CVD grown CNT meshwork after 9 DIV. Neuron adhering well to the underlying CNTs, extend dendrites across a carpet consisting of nanotubes and ECM (left). An ECM "hole" (highlighted by the red square) makes clear the very close contact between CNTs, neurite and ECM.

4.1.3 Imaging of calcium activity

In order to investigate the networks dynamics of cells grown on CNTs and how they can impact neuronal networks, we have monitored the emerging activity with fluorescence calcium imaging. This was the only possible approach we could follow in order to study neuronal network activity due to the fact samples opacity prevent use of patch-clamping electrophysiological technique. With our imaging setup we have recorded representative fields of 120×160 μm^2. At 8-10 DIV neurons are usually synaptically connected and display spontaneous activity including bursts emerging by irregular synchronized firing epochs [3,42,44]. Figure 15A shows the spatial resolution of measured cells that could be simultaneously traced within the same field of view, with single cell resolution.

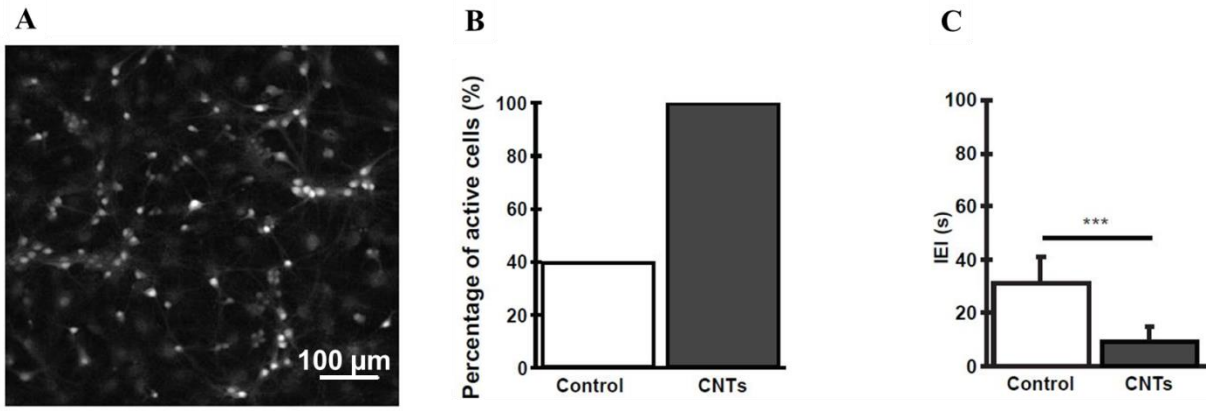

Figure 15. (A) Spatial resolution of the simultaneously visualized cells for each field; Histograms summarize the percentage of spontaneous active cells (B) and the average values of the inter-event interval (IEI; C) for cells cultured on glass control or on CNT carpets [In collaboration with Dr. Rossana Rauti, SISSA, Trieste, Italy].

In our recordings, spontaneous Ca^{2+} activity was detected in 40% of cells grown on glass coverslips, visualized in each field. Instead, in CNTs virtually all (>98%) of the visualized cells were active and generate spontaneous Ca^{2+} episodes. Data are summarized in the plot in Figure 15B. We have measured the occurrence of spontaneous Ca^{2+} episodes in active cells by quantifying the inter-event interval (IEI) that is significantly ($p<0.001$) shorter in CNTs cultures (10±5 s, n=36 cells) when compared to Control ones (32 ±9 s, n=32 cells; plot in Figure 15C), meaning an increased frequency of the spontaneous calcium activity in cells grown on CNTs. Such finding suggests a different functional organization due to the presence of CNTs.

4.1.4 Discussion

In the last two decades carbon nanotubes experienced an exponential increase in the number of application fields ranging from microelectronics and energy storage to tissue engineering and nanomedicine [46]. Many works have demonstrated the great potentialities of CNTs in neuroscience, thanks to their intriguing and unusual ability to boost neural electrical performances [1-4]. In basically all previous studies were used purified MWCNTs, deposited on a supporting glass surfaces via drop casting. Here, for the first time, we have demonstrated that CNTs directly grown on a supporting silicon surface by CCVD preserve the same effect previously demonstrated for "drop-casted" carbon nanotubes. In our approach we developed a novel synthesis method leading to the realization of various CNTs-based architectures characterized by a very high packing density together with well-controlled film uniformity, diameters and lengths. Importantly, our CNT substrates could be employed as they are at the end of the growing process without the necessity of any chemical purification or functionalization in liquid-phase, thus significantly simplifying their use. As a matter of fact, since both XPS (Figure 10) and SEM analysis (Figure 3 and 4) have revealed the absence of metallic residual on CNTs surface, thus suggesting a base-growth mechanism for nanotubes, no acid treatments were performed to remove eventually present heavy-metal (nano)residues. Accordingly, before using for culturing, the samples were just treated with an air-plasma-treatment in order to facilitate cell adhesion and then sterilized with an UV lamp (See Methods). Morphological observation and calcium imaging suggest the formation of healthy and functional neural network on CNTs substrates. In particular, we have reported that the growth of dissociated hippocampal cultures onto CVD synthesized CNT carpets is comparable, in terms of neuronal and glial density and ratio, to the cultures developed on controls glass substrates, thus proving the CNTs biocompatibility when used as growth substrates to support neuronal cells culturing. Remarkably, our CNTs have displayed the exceptional ability to potentiate the electrical activity of neuronal cells cultured on them. Our data are perfectly in agreement with previous studies, demonstrating that CNTs produced by CCVD behave at cellular level in a way similar to what observed in literature for drop-casted substrates [1-4]. The precise mechanism governing such potentiating effect is not totally clear yet. Obviously, cell density in the neural network can influence neural activity. However, since CNTs presence did not affect it, we can exclude the difference in cell density for the two substrates (nanotubes and glass controls) as possible reason for the boosting effect of CNTs on neural performances. It is documented that neuronal electrical properties can be influenced

by material-neuron interactions, especially when the material presents an intrinsic electrical conductivity [47]. Previous studies have hypothesized that carbon nanostructures can provide a sort of electronic shortcut between the proximal and distal compartments of the neuron, via a tight and discontinuous contact between neuronal membranes and CNTs [3-4] (See Chapter 1). Therefore, considering the inherent electrical conductivity together with the numerous nano-topographical cues and large surface area characterizing our novel CVD grown CNT carpets, we can assume that a similar mechanism of interaction with neural cells takes place. The abundant and very tight contacts between CNTs and neurons might represent a physical conduit for electrical coupling.

To conclude, our study has revealed that CVD grown CNTs can structurally and functionally support neural networks formation strongly enhancing their electrical performances. Such finding, demonstrates the possibility of adopting our novel, easy and well-controllable approach to modulate the performance of neural network *in vitro*. Additionally, the extremely high versatility of the CVD growth and the ability to create patterns of any arbitrary shape of CNT-decorated areas on surfaces open to new applications in brain-machine interfaces or neuro-prosthetic devices for regenerative medicine.

4.2 Transparent Carbon Nanotubes guide the reconnection of lesioned entorhinal hippocampal organotypic cultures

In the previous section, I reported the noteworthy ability of our CNTs based substrates directly grown on silicon supporting surfaces, to safely interact and potentiate neuronal networks, an effect already observed for drop-casted CNT carpets, but never verified for CVD grown carbon nanotubes.

However, I pointed out one of the main drawbacks of such preparation: CNT carpets growth on silicon are not transparent: reasons of that could be found in the thickness of the CNT carpet itself but, most critical, in the opacity of silicon wafers that lack optical transparency. This limits the exploitation of all the techniques and methods which require to be applicable to optically visualize cells ‘through’ the specimens, including electrophysiology (i.e. patch clamp experiments) or bright field microscopy (i.e. in order to position an AFM tip above a precise region of a cell as, for example, the nucleus), or any application requiring transmission illumination. To overcome such restrictions, I have modified the fabrication procedure in order to obtain a transparent CNT-based platform. The main point was to grow

CNTs directly on a transparent (and cheap) material able to sustain the high temperatures involved in the process without chemical or dimensional modifications: among all possibilities I choose fused silica. In fact, fused silica (or fused quartz) is a high-transparency glass consisting of silica in amorphous (non-crystalline) form able to sustain the CCVD process. Another important point to take into account in order to obtain transparent carpets of CNTs is the fundamental foresight to finely control the length of the CNTs (see Methods) in order to maintain such value not larger than 10-15 times the wavelength of visible light [48]. By means of electrophysiology and immunocytochemistry experiments, we have documented that this original CNT carpet is capable, as well, to induce the same synaptic potentiation in hippocampal cells observed in the case of opaque CNT films and drop-casted layers [1,3,42], alongside with a correct maturation of dissociated neurons and glial cells.

We move a step ahead with our investigation exploiting the possible use of such substrates as regenerative bidimensional scaffold. For this purpose, we tested the material with a more complex brain structure: for the first time we have interfaced a CNT substrate with Entorhinal-Hippocampal organotypic cultures (EHCs) and we have functionally characterized the neuronal tissue using patch-clamping electrophysiology experiments. We focused our attention in this investigation to the perforant pathway lesion model consisting in cutting, in the organotypic slice, this fibrous interconnection occurring between the hippocampus and the entorhinal cortex. We worsen the model introducing a physical separation between the hippocampus region and the entorhinal cortex region moving them apart roughly 0.5 mm. In our opinion this model better resembles the situation when a mechanical injury occurs in the CNS: a trauma that could cause a substantial separation of tissutal areas or portions previously interconnected [49]. Herein, we have demonstrated the profound impact of our transparent CNTs carpets on EHCs, which ultimately lead to a strong indication of functional and anatomical reconnection of the two brain structures. Our findings, recently submitted to peer review journal, make these substrates potential candidates as materials to be employed in future neural prostheses and implantable neural interfaces. In particular, their transparency could represent an extremely useful property in the field of retina prosthesis.

4.2.1 Transparent CNTs: synthesis and characterization

I have synthesized CNTs directly on supporting fused silica glass substrates via CCVD using, as catalytic element, an ultra-thin iron film 0.2–1.0 nm in thickness. This metallic layer was deposited without any adhesion layer via e-beam evaporation and, after thermal annealing to

convert it in suitable Fe nanoparticles, CCVD was run just for 90 seconds in order to limit the length of the so obtained CNTs (see Methods for more details). As previously describe for their opaque counterpart, in the CCVD process catalyst film thickness plays an important role since it determines, together with annealing thermal treatment parameters, the diameter of catalyst nanoparticles from which CNTs will grow up [50]. Other research groups, in order to preserve catalyst layer and to enhance CNT growth yield, have used intermediate metallic layers as adhesion and/or anti-diffusion layers between the catalyst and the underneath support surface [51]. Moreover, it was reported that by setting the annealing treatment conditions at 720 °C for 3 hours and the growth parameters at 720 °C for 1 hour, it is possible to obtain vertically aligned CNTs (VACNTs) on various supports [52]. In our CCVD synthesis method any adhesion layer was employed and, even if the growth time was limited to few minutes, the obtained CNTs carpet covering the supporting substrate demonstrated to have the same characteristics of carbon nanostructures produced using an adhesion-layer or by using more time-consuming methods. These peculiarities of our laboratory-scale process, together with inexpensiveness and the fact final samples are transparent to visible light, make it an extremely interesting substrate model for cell research purposes.

Regarding more in detail the material, the same morphological and chemico-structural characterization (i.e. SEM, TEM, Raman, XPS) have been performed on transparent CNT films revealing no significant difference with their opaque counterpart. Notably, the remarkable transparency of CNT carpet grown on fused silica, compared to that of nanotubes synthesized on silicon, can be appreciated in Figure 16.

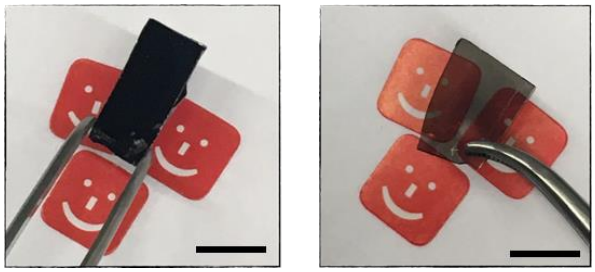

Figure 16. Representative optical images of CVD grown CNTs on silicon (left) and on fused silica (right) substrates clearly showing the higher transparency for the latter (right) (scale bar: 8 mm).

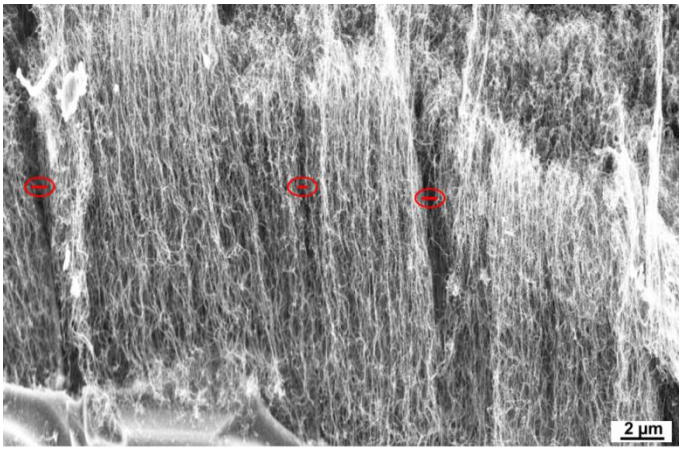

Figure 17. Side view SEM image CNT films showing their vertical alignment and the formation of channels voids (highlighted by red circles) probably permitting the transmission of visible light.

It was documented that the transparency of CNT forests synthesized on transparent substrates, such as thin (50 nm) Si_3N_4 membrane supported by a silicon frame, strongly depends on tube's length (i.e. film thickness). Specifically, shorter films (~20 µm) have shown high level of optical transparency, while thickness greater than ~70 µm have determined strong level of absorbing (opaqueness) for wavelengths in the visible [48]. They hypothesized that the mechanism determining this unusual transparency to visible light can be ascribed to the formation of self-assembled vertical voids within the CNTs mat. Such longitudinal cavities, by acting as light channels, direct the transmission of the light for the entire thickness of CNTs film. Since in this study we have adopted CNT films with thickness of around 10 µm and considering also the morphological similarities between the CNTs used in [48] and our substrates, assessed by FE-SEM imaging, we can assume the same mechanism takes place enabling also in our samples the transmission of visible light (Figure 17). In Figure 18 (left) vertical aligned CNTs, oriented perpendicularly to the surface substrate, are shown while the TOP view (Figure 18, right) revealed a random orientation. The parallel morphology, as described before (see paragraph 4.1.1 of this chapter), is established by the proximity effect of densely distributed catalyst nanoparticles forcing the initially randomly oriented CNTs into a vertical alignment [18]. Figure 19 highlights that CNTs are uniformly distributed on the underlying fused silica substrate. Remarkably, since no catalyst nanoparticles were detected on CNTs surface, also by increasing the magnification, a base-growth model was hypothesized for the formation of the tubes (as in the case of CNTs grown on silicon) [6] (see Chapter 2).

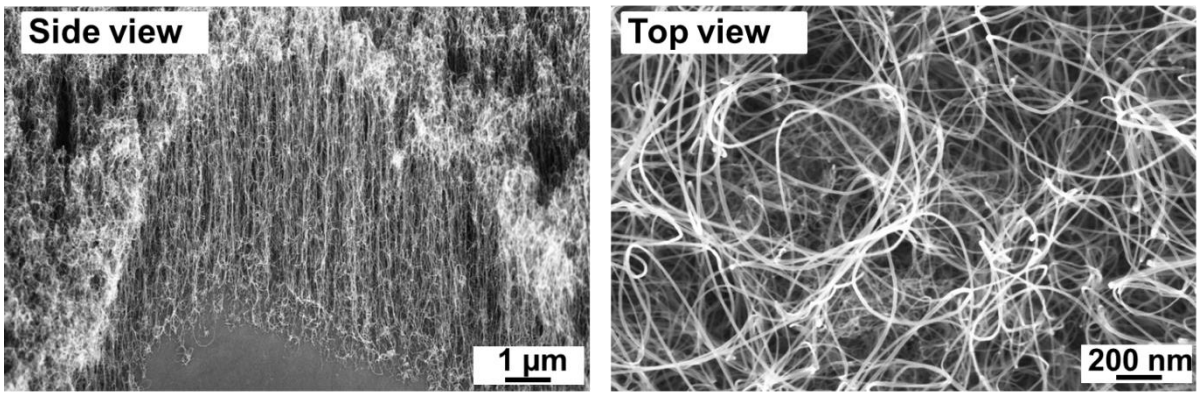

Figure 18. SEM micrographs of transparent CNTs meshwork. Side view FE-SEM image (left) showing vertical aligned CNTs, oriented perpendicularly to the underneath SiO_2 substrate. Conversely, in the top view CNTs are randomly oriented (right).

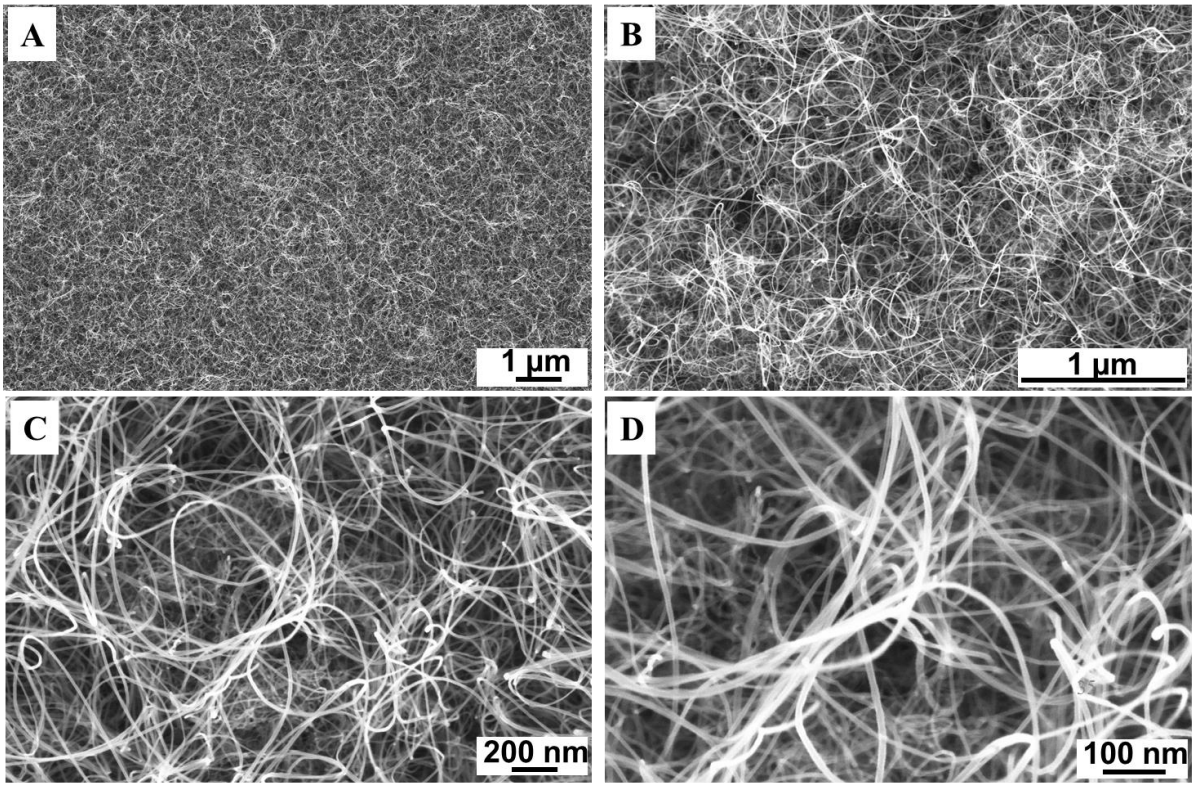

Figure 19. Top-view SEM images of transparent CVD-grown CNTs at increasing magnifications.

In order to highlight the structure and crystallinity of our CNTs, TEM characterization was conducted. Therefore, we have seen that CNTs consist of multi-walled nanotubes with different wall number. Specifically, Figure 20A shows an isolated MWCNT with an outer diameter (OD) of less than 20 nm and an inner diameter (ID) of approximately 10 nm. This

measurement is consistent with 15 nanotube walls (Figure 20B). However, TEM analysis points out the presence of structural defects represented by the darker regions on the side wall (Figure 20, A and B), probably ascribed to the low temperature used to grow our CNTs compared to other methods (730 °C) [24].

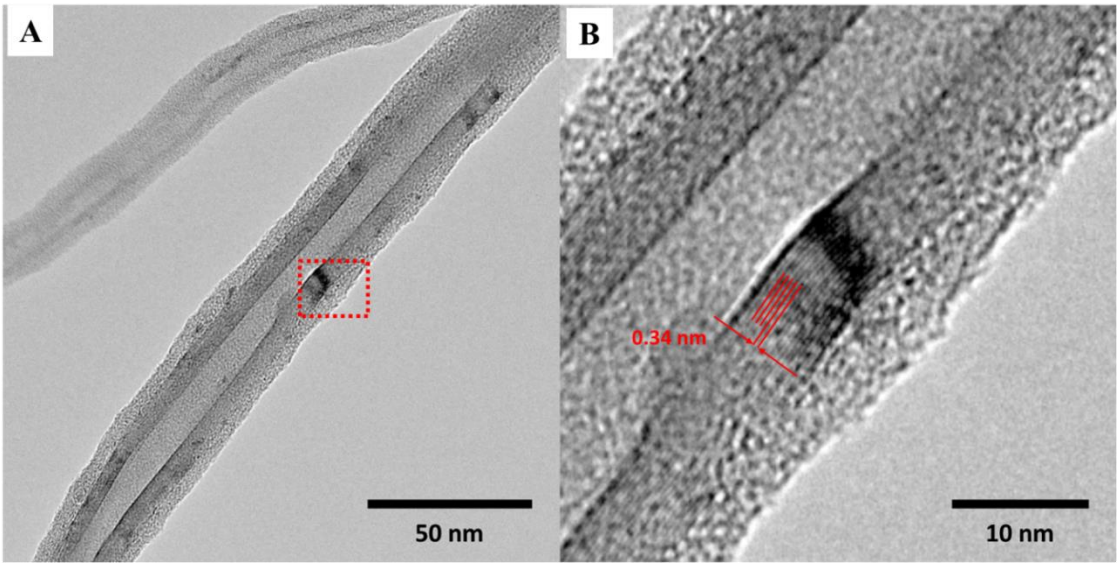

Figure 20. (A) TEM image of an isolated multi-walled nanotube constituting the mat with different wall number and a particular of an isolated MWCNT showing well-resolved single walls (B).

Raman spectroscopy analysis was performed in order to evaluate the structural arrangement and the quality of transparent CNT film. Raman spectra recorded on transparent CNT films, and shown in Figure 21, highlighted the two main bands typical of all graphite-like materials (including their opaque counterpart): the G band at ~1583 cm^{-1}, due to their graphitic nature, and the D band at ~1330 cm^{-1}, indicating the presence of amorphous and/or low ordered carbon structure (carbonaceous impurities with sp^3 bonding, and broken sp^2 bonds in the sidewalls) [53]. As described for opaque nanotubes, the quality of MWCNTs is generally expressed by the ratio between D (I_D) and G (I_G) bands integral intensities. Also for transparent CNTs such bands showed similar intensities, thus indicating the presence of non-graphitic carbon in nanotubes [54], phenomena already documented in the case of low temperature CVD-grown CNTs [55]. Together with the D and G bands, the second-order Raman peak G' located at ~2700 cm^{-1} was observed. This peak is characteristic of graphitic sp^2 materials and is related to the defect density and to the CNTs metallicity [33-34]. Other peaks located at ~1698 cm^{-1} and at ~1759 cm^{-1} are related to νC=O vibrations [56-57] and indicate a possible partial oxidation of MWCNTs.

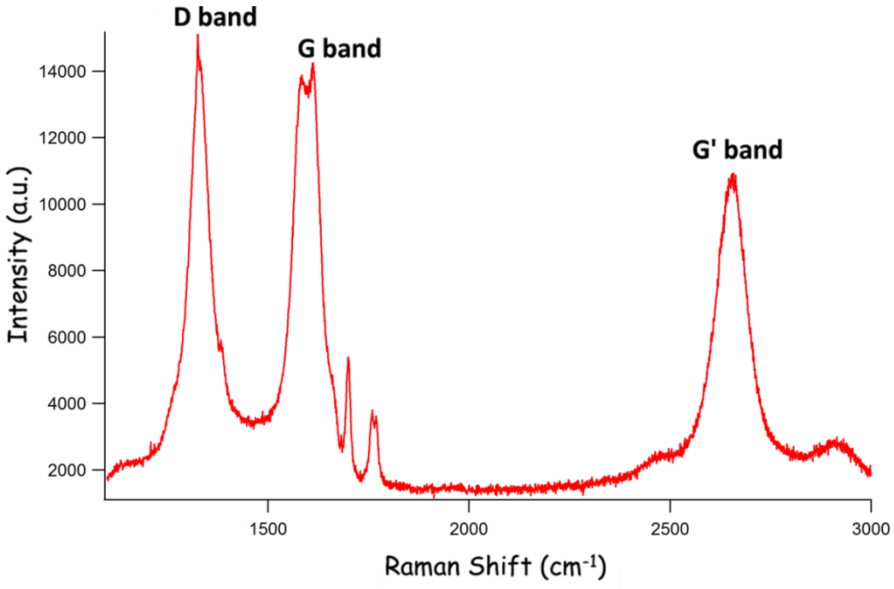

Figure21. Raman spectra of transparent CNT films exhibiting typical bands of low temperature CVD grown CNTs. [In collaboration with Alois Bonifacio, University of Trieste, Italy].

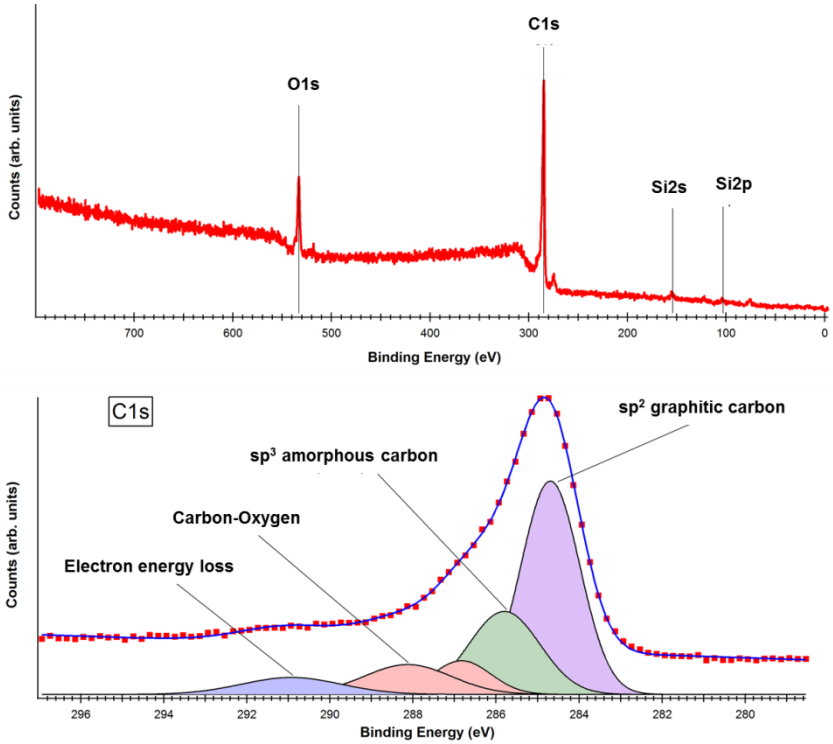

Figure 22. XPS survey (A) and C1s core level (B) of transparent CVD grown CNTs. [In collaboration with Dr. Matteo Dalmiglio, ELETTRA Synchrotron Light Source Trieste, Italy].

From the other hand, the XPS survey spectrum of CNTs in Figure 22A highlighted the presence of three elements clearly identifiable: carbon (C1s), oxygen (O1s) and silicon (Si2s, 2p). The amount of C and O are 87.6% and 10%, respectively while a small amount of 2.4% of Si was present, thus indicating also in this case a fine covering of the underneath silica support. Notably, also in this case we can assume a base-growth model as nanotubes formation mechanism since the absence of iron residual on CNTs surface (this data is confirmed by SEM observations too) [6] (see Chapter 2). Figure 22B indicates the C1s core level for ~8 μm long CNTs which presents the characteristic peaks of CNTs, already described for CNTs grown on silicon, and related to sp^2 and sp^3 hybridized carbon atoms, electron energy loss peak due to π-plasmon excitations and the presence of oxygen. A Shirley background has been subtracted.

4.2.2 Transparent CNTs interfacing dissociated primary neurons

Since transparent CNT (tCNT, hereafter) films resulted from a novel synthesis process, our first concern was to understand if such substrates can sustain correct neural growth and network development and if they would modulate the synaptic activity in a similar way traditional, opaque MWCNTs, do [1,3]. For this purpose, we choose to use a well know and characterized cellular model: primary cellular cultures made by dissociated cells from rat hippocampus. We started comparing hippocampal neuronal networks developed on control glass coverslips with those cultured on tCNT substrates by immunofluorescence experiments. We have visualized neurons and glial cells, targeted with β-tubulin III and GFAP antibodies, respectively, to evaluate the morphology of the network and its cellular composition, quantifying the neuronal and glial cell density after 8-10 days of growth *in vitro*, which were found to be similar in CNTs and control cultures (Figure 23A). As shown in the histograms of Figure 23B, we found comparable numbers of neurons and astrocytes developed above the two investigated substrates (control glass and CNTs), indicating that nanotubes did not affect both neural and astrocyte density.

Additionally, from the functional point of view, we have compared the spontaneous activity of hippocampal neuronal networks directly grown on CNTs mat with that of control networks grown on conventional substrates (poly-L-ornithine-treated glass) by means of whole cell patch clamp recordings. I want to stress here that such experiments, involving patch-clamp electrodes, were possible only due to the optical transparency of such CNTs-based substrates which enabled a proper visualization of cells and glass electrodes during electrode approach,

patch formation and electrophysiological recordings. These methodology is otherwise impossible –or, at least, extremely complex necessitating to make cells fluorescent (e.g. via GFP expression)– by employing opaque CNTs grown on silicon. As a matter of fact, opaque CNTs sample functional characterization was done performing calcium imaging analysis than patch clamping (see paragraph 4.1.1).

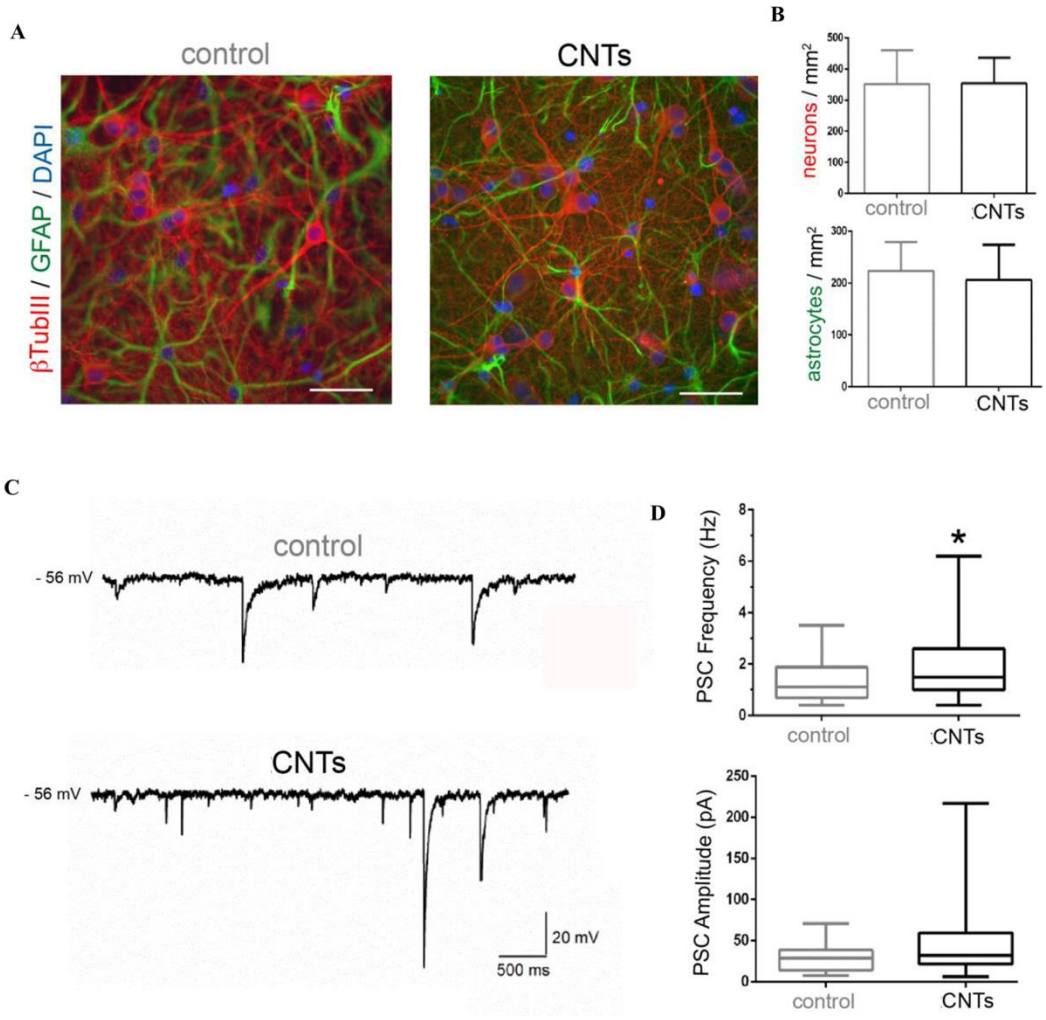

Figure 23. (A) Representative fluorescent micrographs depicting dissociated primary neurons grown on control substrates (left) or CNTs substrates (right) stained with β-tubulin III to see neurons, GFAP to highlight astrocytes and DAPI to stain cell nuclei (Scale bar: 50 µm). As summarized in the plots in (B) we have found a similar density of both neurons and astrocytes in the two conditions. (C) Representative traces of whole cell patch clamp recordings for glass controls and CNTs. A significantly higher frequency of PSC current in the presence of CNTs compared to the control (D, upper plot), with no substantial changes concerning the amplitudes of PSCs (D, lower plot).

Moving back to our experiments, since the appearance of spontaneous postsynaptic currents (PSCs) provides clear evidence of functional synapse formation and is a widely-accepted index of network efficacy, we monitored PSCs in both the investigated conditions. The frequency of the activity recorded from hippocampal neurons cultured onto CNTs carpets was found to be significantly enhanced compared to controls (controls: 1.3±0.1 Hz; n=40; CNTs: n=59; 1.8±0.1 Hz; p=0.03; data from n=7 culture series), while amplitudes were not affected significantly by the presence of CNTs (controls: 30±2.8 pA; CNTs 44±5 pA; p=0.10; Figure 23D), as the input resistance (controls=790±104 MΩ; CNTs =587±67 MΩ; p=0.10) and membrane capacitance (control=34±2 pF; CNTs 39±3 pF p=0.20) values. . In first approximation, considering that any variation in cell densities was found between networks developed above glass controls and CNTs, the increase in frequency could reflect some change at presynaptic level; while the fact amplitudes do not change is associable to any post-synaptic variation occurring in CNT interfaced neuronal networks. These considerations, anyhow, necessitate to be confirmed by a specific study at synaptic level, for example recording miniature excitatory post-synaptic currents (mEPSCs) in presence of tetrodotoxin (TTX – a toxin able to specifically impair voltage-dependent Na+ channels). Our data, revealing increased PSC frequency, associated with similar values of both PSC amplitudes and passive membrane properties, are in agreement with previous studies related to drop-casted CNTs substrates [1,3].

After this "validation" experiments we moved, as previously described, to a more complex *in vitro* brain model, such as the EHCs organotypic cultures.

4.2.3 CNTs induce synchronized Entorhinal-Hippocampal activity

Previous studies have reported that CNT-based substrates possess, to a certain extent, regenerative features for spinal cord organotypic cultures [2,58]. Therefore, we have investigated if our tCNTs would preserve, or increase, these effects when tested on brain areas such as the cortical ones. In particular, we have simulated a lesion at the subicular level involving the perforated path where the cortex and the hippocampus regions of an organotypic slice were moved apart of about 400 to 600 µm (see Methods). The aim of such experimental model was to mimic *in vitro* a traumatic event in which the cortical areas undergo to a separation due to mechanical injury (even though the model could give relevant information for spinal cord injury too). As already introduced, transecting the hippocampal formation at the subicular level leads to the disruption of the main excitatory pathway that

from the cortical areas reaches the hippocampus, known as the Perforant Pathway (PP) [59]. Lesioning the PP at the subicular level has already been exploited as a lesion model [60-62] because, since the lesion site is relatively distant from the Dentate Gyrus, degenerative/inflammatory effects, due to the lesion itself, can be easily discriminated from the regenerative effects of post-lesion circuit re-organization observed in the hippocampus [60]. Furthermore, it is known that the de-afferentation caused by the PP interruption, leads to a lamina-specific re-arrangement of the fibers and dendrites of mature granule cells [60,62], which may potentially be instructed by artificial cues, such as the physico-chemical features of CNTs.

We have evaluated the electrical activity of the slices by extracellular Local Field Potentials (LFPs) simultaneous co-recordings. Taking advantage of optical transparency of tCNTs substrates, under an inverted optical microscope, we have placed one electrode in the molecular layer of the DG (a major hippocampal hub of the Perforant Pathway), while a second electrode was positioned within the deep layer (IV/V) of the EC, where the Pathway should end (schematized in Figure 24A, left for the whole slice and right for the lesioned one). In all recordings, spontaneous LFPs were detected by both electrodes. We observed no significant changes in LFP frequency in CNT-interfaced cultures, when compared to controls, in whole (Figure 24B, left) (control: DG=0.3±0.05 Hz and EC=0.22±0.08 Hz; CNTs: DG=0.25±0.05 Hz and EC=0.21±0.04 Hz; p=0.75 and p=0.89 respectively; n=8 number of slices for controls and n=5 for CNTs) and in lesioned slices (Figure 24B, right) (control: DG=0.1±0.03 Hz and EC=0.05±0.01 Hz, n=9; CNTs: DG=0.2±0.03 Hz and EC=0.1±0.01 Hz, n=4; p=0.16 and p=0.55). Furthermore, we have measured the Entorhinal-Hippocampal LFP synchronization before and after adding Bicuculline, a blocker of ionotropic $GABA_A$ receptors, used to enhance the signal synchronization. Thus, we have found that CNTs substrates induce a strong increase in the signal synchronization, measured as Pearson correlation coefficient (CCF) whose statistical significance was determined by a permutation test (see Methods). In not lesioned cultures (entire slices), 43% of controls displayed Entorhinal-Hippocampal synchronized activity in standard saline solution (mean CCF of 0.34±0.1); while, in the presence of Bicuculline, this value reached the 86% of samples (mean CCF of 0.52±0.11; Figure 24D, left). Interestingly, 100% of CNT cultures were synchronized (mean CCF=0.55±0.18) when already in standard extracellular solution, and this percentage did not change in the presence of Bicuculline (mean CCF=0.67±0.13; p=0.01; Figure 24D, left). Still, the most striking impact of tCNTs substrates on the signal synchronization degree

between the EC and the DG was found for lesioned slices. As shown in Figure 24D (right), control lesioned cultures displayed correlated signals only in the 11% of cases in standard saline solution (mean CCF=0.39±0.11); a value which increased to 33% of correlated signals upon Bicuculline application (with a mean CCF=0.66±0.11).

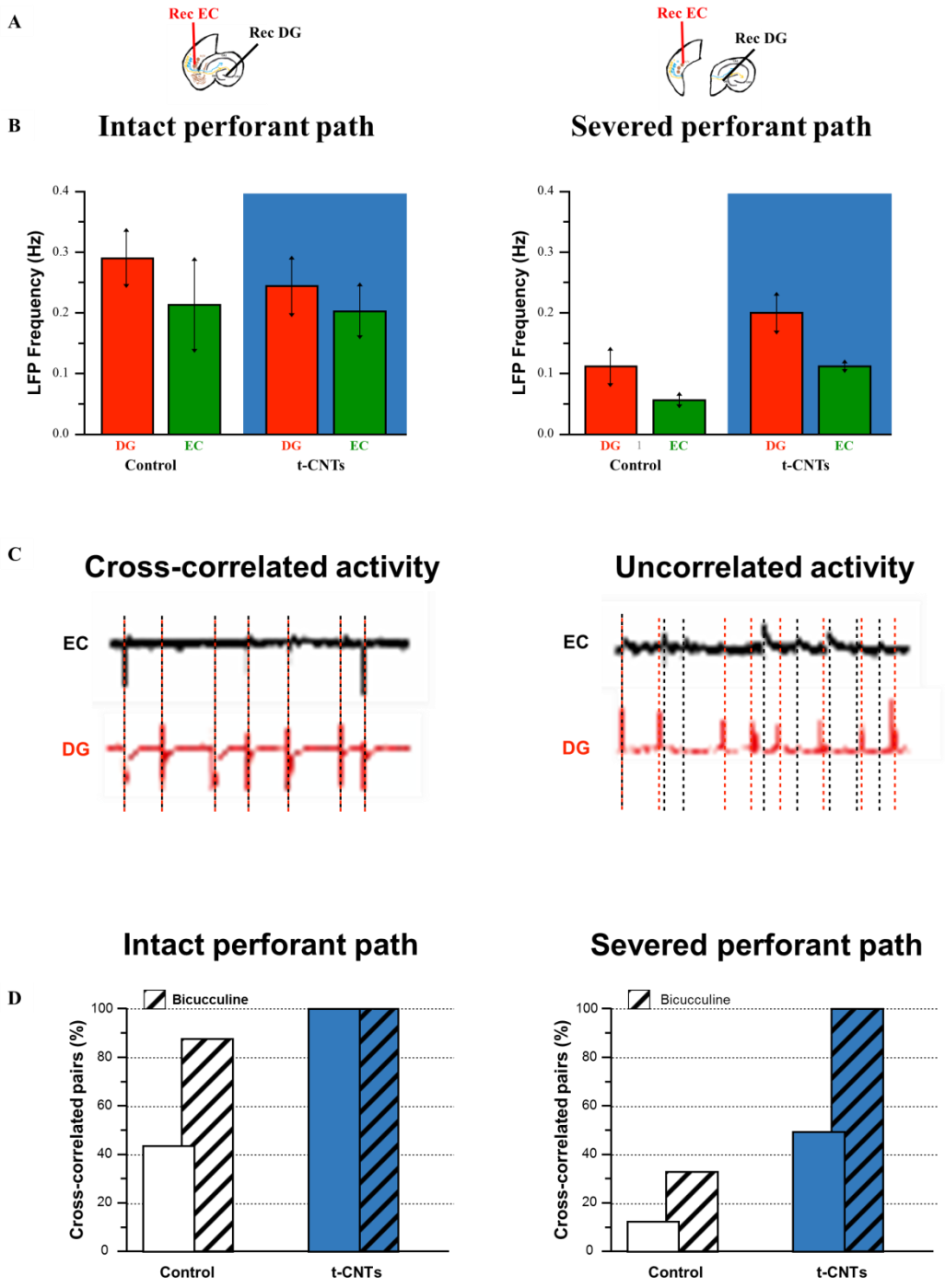

Figure 24. (A) Representative sketch showing the experimental setup adopted to perform field potential extracellular co-recordings from the EC (red) and hippocampal DG (black) in entire (left) and lesioned (right) slices. As shown in (B) no significant differences were detected in terms of LFP frequency between the two conditions. In (C) a comparison between

voltage tracings in the case of cross-correlated (left) and uncorrelated (right) activity between the EC and the DG is reported. In (D) it is evident how the totality of the voltage signal pairs was found to be synchronized in tCNTs entire slices (left panel) either in standard and Bicuculline-enriched extracellular solution. Concerning the control condition instead, the synchronization between DG and EC was found to be lower, and underwent to a 2-fold increase of its original value (from 43% to 86%) when Bic was added in entire slices. Control related lesioned slices signal synchronization was found to be lower with respect to CNTs (11% *vs* 50%, right panel). This difference was still evident (33 % *vs* 100%) when slices were treated with Bic (right panel). Note that tCNTs related signals reached the 100% of synchronization even in Bic-perfused lesioned slices, suggesting that a reconnection is established in all cases.

Since this measurement reflect a condition in which the PP had been transected and the resulting slices were outdistanced, we expected at least a decrease (if not a total absence) of the DG-EC signal synchronization with respect to not lesioned slices, because of the anatomical lack of fibers needed to carry the signals. The observed presence of a synchronized activity, even if lowered, could presumably reflect the slice ability to sprout new fibers able to re-connect the two parts of the organ. Lesioned EHCs interfaced to tCNTs carpets displayed a synchronization degree of 50% when recorded in standard saline solution (mean CCF=0.58±0.21; Figure 24D, right); surprisingly a full synchronization (100% of signals were correlated; mean CCF=0.9±0.06; Figure 24C, right) of the recorded signals was observed, when $GABA_A$ receptors were blocked with Bicuculline. Such results are particularly important, because revealed the potential ability of our nanomaterial to functionally re-connect the nervous tissue after a lesion.

Finally, we have investigated whether the tCNT-related increased synchronization was also reflecting by an increased re-generation of axons which would be able to carry the electro-chemical signals. In fact, at time zero, meaning immediately after the lesion, there are no fibers crossing the separation gap between entorhinal cortex and hippocampus, while, along with the culturing, sparse fibers tend to regrowth (Figure 25, left). By immunofluorescence we have visualized non phosphorylated neurofilament protein (SMI32) positive axons (see Methods) crossing the gap between the two cortical structures ("crossing-fibers"). As shown in Figure 25, left, we have observed that cultures grown on tCNTs mat displayed a significant increase of SMI32-positive fibers sprouting into the lesioned area and reaching the facing tissue section with respect to the control glass condition (control: n=7 number of slices, tCNTs: n=6; p=0.02; Figure 25, right). Considering the previously described increase in LFP synchronization observed in CNT-lesioned slices compared to controls, this result would strongly indicate the tCNT platforms are able to induce on EHCs cultures an increased

expression of functionally-active neural processes that are able to establish an active/functional cross-talk between the two parts of the organ.

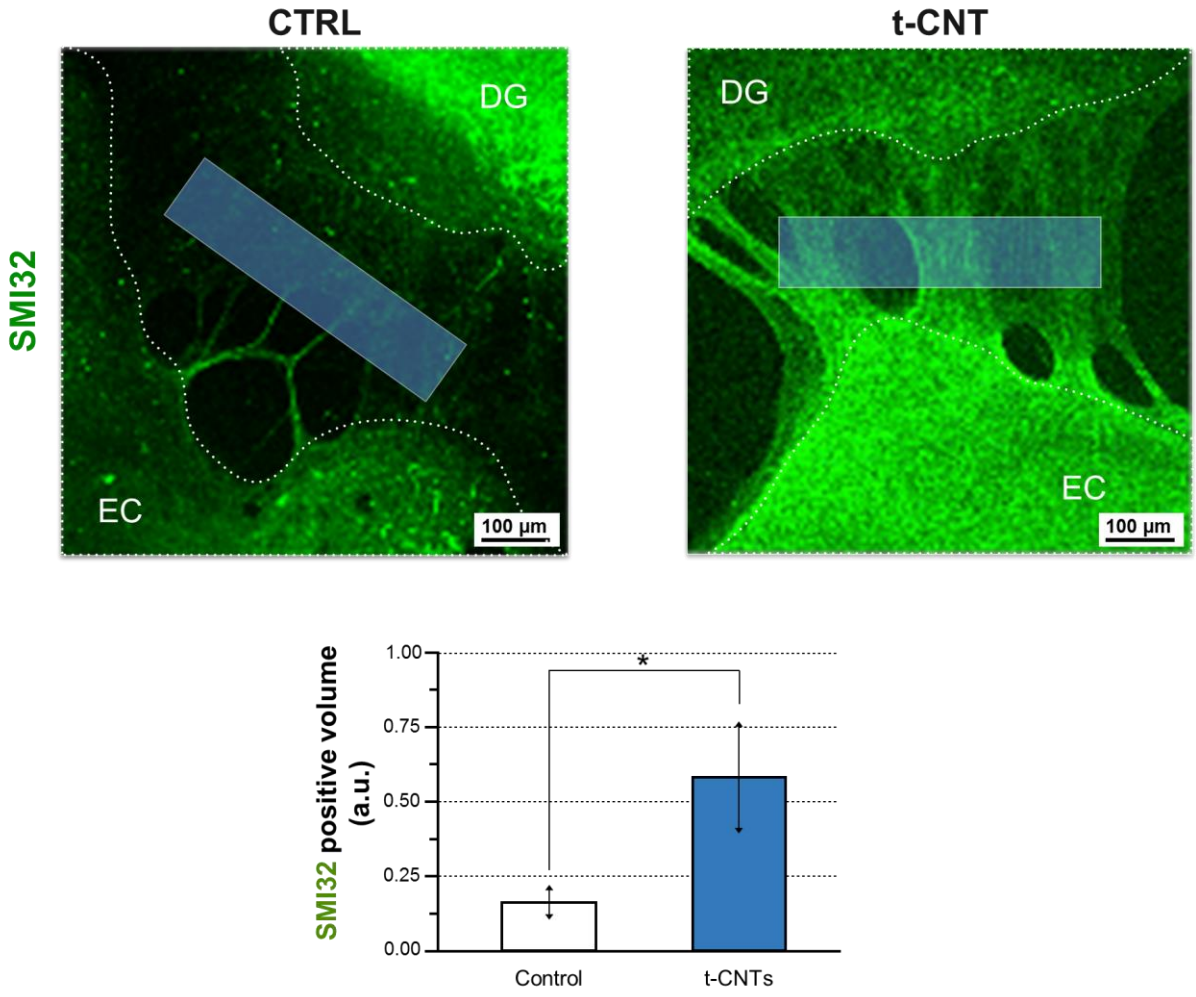

Figure 25. Representative confocal images showing the sprouting of SMI32-positive fibers into the lesioned area. As summarized in the plot, cultures grown onto CNTs displayed a significantly higher percentage of SMI32-positive volume with respect to controls.

4.2.4 Discussion

In this study we have reported a novel strategy to fabricate CNTs-based substrates, which could give rise not only to optically dark mats, but allows to obtain transparent carbon nanotubes substrates (tCNTs) too. The passage of visible light, despite the 'darker than black' association attributed to carbon nanotubes [48] opens the material to more investigation techniques. This was possible by synthesizing CNT films characterized by a thickness of about 10 µm via CCVD directly on a transparent substrate (i.e. fused silica). For the first time,

we have demonstrated that such CNT mat possess the potentiating [1,3] and regenerative [2,58] effects previously observed on neural networks interfaced with 'standard' drop-casted CNTs films. We have reported that the growth of dissociated hippocampal onto CNT carpets is comparable, in terms of neuronal and glial density, to control cultures. Additionally, neurons, when interfaced with these carbon nanostructures, displayed a significantly higher synaptic activity, measured as an increase in PSCs frequency. The exact mechanism inducing such boost in synaptic activity when neurons are interfaced with CNTs is still not clear. Many speculations could be done involving a chemical contribution, a morphological contribution and/or an electrical contribution. At the present the electrical hypothesis is the more accepted as pointed out by the works of Ballerini and co-workers [4-83].These results are consistent with previous works and, in the future, we propose to investigate the synaptogenic capability of the material pointing out excitatory and inhibitory synapses densities.

Since the understanding of the regenerative effects of this material is fundamental in the perspective of using our CNTs as neuro-prosthesis material or for the construction of implantable neural devices, we have interfaced such novel CNTs-based scaffold with organotypic EHCs cultures, a complex 3D explant of the CNS in which the functional and anatomical connections are largely preserved [62]. We have investigated the effect of these nanostructured substrates in entire and lesioned slices: in the latter case, by mechanically lesioning the cultures at the subicular level and outdistancing the resulting parts about 0.5 mm apart, we have simulated a severe traumatic injury of the CNS. Based on the previously observed CNTs regenerative impact on spinal cord segments [2,58], our interest has been addressed to understand if those positive effects could be translated even on complex structures of the brain itself, such as the cortical and sub-cortical ones. We have demonstrated here that our tCNTs allow an increased degree of synchronization between the hippocampus and the entorhinal cortex. Surprisingly, the regenerative effects of CNTs were most clear when interfaced with lesioned EHCs cultures. As matter of fact, in this latter case we have observed a 4-fold increase in the percentage of correlated signals (50% of the cultures against the 11% in controls) between the hippocampal DG and the EC in standard saline solution, which raised to the 100% of the slices, when cultures were perfused with the $GABA_A$ antagonist Bicuculline. This result strongly suggests that CNT can help in promoting a successful reconnection between the two slices after the lesion. Finally, we have demonstrated that changes in axonal regrowth may account for the enhanced correlated activity observed in

tCNT samples, because tCNT-related slices displayed a significantly higher amount of SMI32-positive fibers between the facing Hippocampal and Entorhinal portions.

By developing a novel approach to synthesize uniform CNTs substrates which are transparent to the visible light and are able to demonstrate the benefits they offer to lesioned organotypic EHCs cultures reconnection, we reinforced the current knowledge of the CNT effects on neuronal networks. CNTs, with their peculiar transparency coupled to the regenerative effects on the CNS-derived tissue, could represent a promising scaffold to be exploited in a broad range of application in modern neuroscience, ranging from the construction of research tools to the building of medical devices and neural prostheses [63-64].

4.3 Transparent Carbon Nanotubes influences the onset of calcific aortic valve disease

As previously reported (see Chapter 1), the calcific aortic valve disease (CAVD) is profoundly related to changes in the extracellular matrix morphology and mechanical properties and, in particular, valve interstitial cells (VICs) seem to be the triggering cell phenotype [65]. In this framework, the interaction between VICs and substrates featuring different compliance [66] together with the influence of chemical and/or morphological ECM properties could represent valid tools to drive VICs phenotype fate in pro-pathologic direction or not. Therefore, based on the fundamental role of ECM in this context and considering the previously described peculiar characteristic of our CNTs-based substrate to structurally resemble the natural ECM [20], we interfaced such nanostructured surfaces with porcine valve interstitial cells (pVICs) in order to investigate and try to modulate cellular properties *via* such ECM-like (nano)engineered surface. In particular, I took advantage of my transparent CNT substrates, directly grown on supporting fused-silica surfaces by CCVD (see Methods and section 4.1 of this chapter). By exploiting the optical transparency of our novel CNTs-based scaffold, we have done immunofluorescence assays, to investigate cell morphology and phenotype and, for the first time, simultaneously performed AFM force-spectroscopy measurements to evaluate cell mechanic properties pointing out, in this way, the stiffness of pVICs cultured onto these carbon-based substrates. Their mechanoresponse was then compared to the results come out from pVICs cultured on control, flat, glass slides. Interestingly, we have observed that the CNTs mat is characterized by stiffness similar to the one of healthy valve inlets (Figure 26) [67].

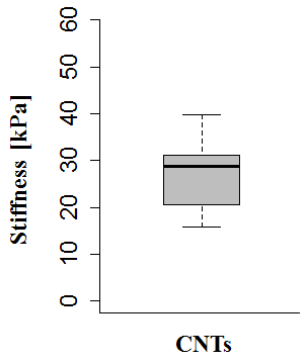

Figure 26. CNT substrates stiffness quantification via AFM (Median: 28.80 kPa; Mean: 27.50 kPa; n=5).

In this way, we have separated the contribution of substrate stiffness from the impact of nanotubes morphology on cell behavior.

4.3.1 Effect of tCNTs on cell morphology

Various studies have revealed possible toxicity of CNTs for living organism (see Chapter 1) [68-70]. In particular, different effect on cells was observed depending on the semblance of CNTs: the unbound form (solution-floating SWCNTs) seem to induce asbestos-like pathologies, such as granulomas, DNA damage, altered expression of inflammatory genes, oxidative stress, atherosclerotic lesions [70]. From these observations arise a sort of 'CNT-syndrome' that, in recent years, enormously reduced the use of this material in the biomedical research field. Anyhow, such problems involved just free-floating or air-dispersed CNTs. It is, in fact, well demonstrated in literature that any toxic effect is observable on cells or tissues facing CNTs firmly attached to an underlying glass substrate [1,3,4,71]. Our carbon nanostructures belong to this second category, because they were directly grown on a glass substrate and, as consequence of that, they result strongly attached to the underneath surface. In this condition, they did not reveal cytotoxic or any negative effects on cells cultured above them, apart in the case where presence of impurities, such as metallic and, in general, synthetic residuals, was demonstrated for the CNTs. Anyway, despite such previously reported findings, in order to demonstrate that cells could develop in a healthy condition when plated above CNTs attached to a glass substrate, we have investigated the efficiency of cell adhesion and the possible toxicity by immunofluorescence assays (see Methods). By means of this set of experiments, we have demonstrated that our nanostructured 2D scaffolds not only are not toxic for pVICs but, in addition, cells are characterized by a good adhesion to the

CNTs substrates. Afterwards, based on the idea that the ECM morphology could induce or inhibit pro-pathologic variation in pVICs mimicking, in the first case, the onset of the CAVD [65], we have evaluated if and how our nanomaterial, resembling the real ECM, influences the morphology and phenotype of the pVICs. Specifically, in order to assess possible morphological variations of cells cultured on CNTs, we pointed out cell shape marking the cytoskeletal component actin and, subsequently, we evaluated average cell areas (Figure 27A) and the average area-to-perimeter ratio (Figure 27B) for cells interfaced with transparent CNTs and flat glass supports (control condition). Such morphological characterization (Figure 27, A and B) revealed that cells cultured on glass controls are, in general, more spread over the substrate than those grown on CNTs regardless of the seeding time (12-72 hours).

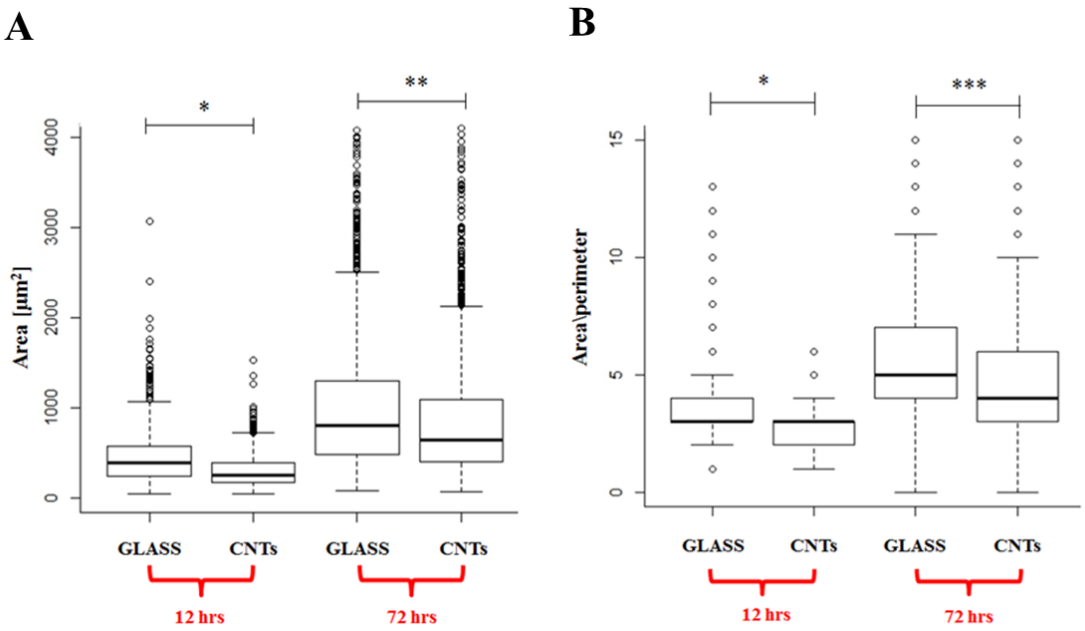

Figure 27. Morphological characterization of VICs grown on glass control and CNTs. A) Quantification of the cells area after 12-72 hours by seeding. b) Quantification of the ratio area vs perimeter after 12-72 hours by seeding (t-Testp<0.05=*, p<0.01=**, p<0.001=***, set=3, 25 fields for sets).

Afterwards, we focused our attention on possible phenotypic changes induced in VICs when interfaced to CNT mats. By considering the specific shape of cells, we identified three different cell morphologies, subsequently correlated to three different cell phenotypes [72]: i) myofibroblasts (Mfib), featuring relatively spread shape and large body area; ii) fibroblasts (Fib), characterized by a highly elongated shape and, iii) smooth muscles cells (SMc), presenting small areas and narrow shapes. The pie chart shown in Figure 28 points out a

reduction in Mfib percentage in cells cultured above tCNTs with respect to glass controls (10% on CNTs and 50% on glass controls, respectively). Interestingly, the percentage of myofibroblasts detected on glass controls is comparable to that found in pathologic valves (e.g., calcific heart valve syndromes); conversely, the amount of Mfib in the presence of CNTs is similar to that characterizing healthy valve [73].

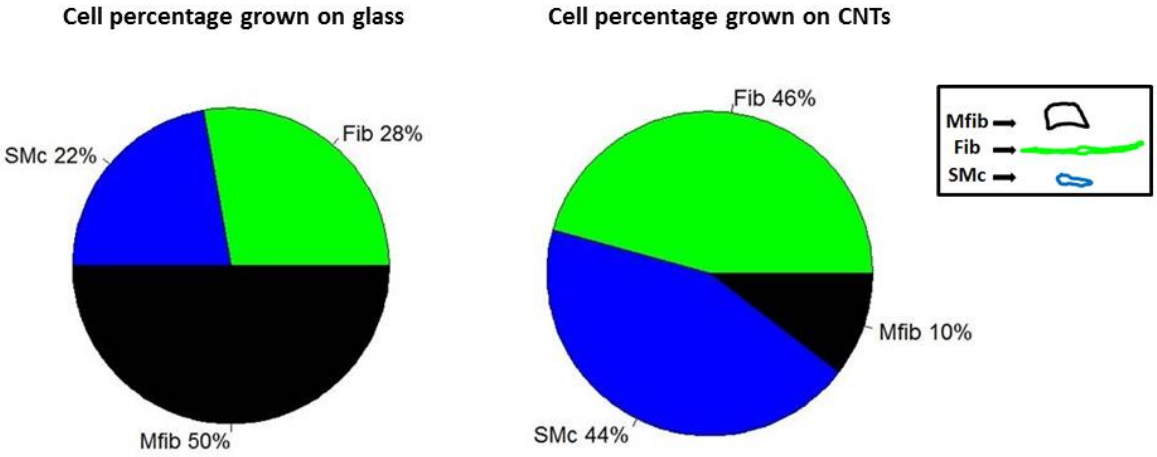

Figure 28. Pie charts showing the percentage of the three VICs phenotypes for control glass and CNTs substrates.

4.3.2 Cell stiffness and role of focal adhesion points

The stratified layered structure of aortic valve leaflets determines a significant mechanical heterogeneity in such tissues [74]. The mechanical cross-talk between different zones of the leaflets, arising from such heterogeneity, seems to be an important player in the onset of CAVD [75-76]. Not surprisingly, it was documented that the mechanical properties of the surrounding ECM strongly affect VICs elastic moduli [77-78, 65]. Therefore, we have investigated if our CNTs scaffold may affect the mechanical properties of VICs when cultured above them. Specifically, AFM force spectroscopy analysis was performed on cells grown on both substrates (glass and CNTs), previously marked with fluorescent dyes, in order to collect cell stiffness data. For this purpose, we performed a novel measurement approach evaluating, at the same time, cell morphology/phenotype, via immunofluorescence essay, and cell stiffness, via AFM analysis, for cells grown on CNTs. This was possible thanks to the optical transparency of our CNTs-based substrates that has made possible such type of characterization, by providing the possibility to clearly visualized fluorescent cells by means of the inverted optical microscope above which our home-assembled AFM is mounted. These

measurements have permitted to assess an increased stiffness of the fibroblasts grown on CNTs substrates when compared to the control cultures (i.e. fibroblasts on glass slices). Surprisingly, myofibroblasts interfaced with CNTs seem to be softer than those grown on glass controls. Any difference in cell stiffness was instead appreciable in smooth muscle cells grown on both substrates (Figure 29).

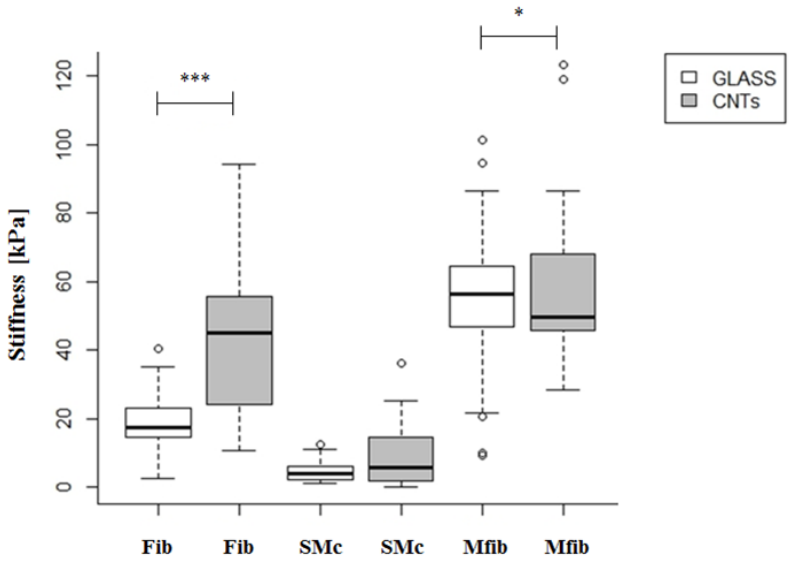

Figure 29: Mechanical properties analysis of all the three pVICs phenotypes identified when grown on glass substrates and CNTs substrates (t-Testp<0.05=*, p<0.01=**, p<0.001=***).

Since it was documented that fibroblasts and myofibroblasts are affected by ECM variations in a different manner [80], our observations related to a different mechanical behavior of these two types of phenotypes can find a partial confirmation in literature. A possible explanation of this intriguing behavior is that cells characterized by a small body area (i.e. cells of elongated shape) feel the nanometric stiffness of the CNTs (structural contribution, in the order of GPa) compared to cells having a large body surface that, instead, feel the micro- or macro-scopic stiffness of the CNTs carpet (geometrical contribution, kPa range). As consequence of that, nanotubes perturb more effectively VIC stiffness when the contact area between cells and the underneath CNT mat is small.

In order to go deeply into this aspect of CNT/VIC interaction, we have evaluated the number of focal adhesion points (FAs), through which a link between cell and ECM constituents is established. Since FAs could be directly associated to the intracellular tensional state [81], their quantification could give us additional information related to the observed variation in

the mechanical properties of Fib and Mfib. Accordingly, we have employed immunofluorescence staining to mark the vinculin (See Methods) and fluorescence microscopy to compare the number of FAs in cells grown on control glass and in cells cultured on CNTs substrates. Figure 30A shows the data summarizing our observations related to the analysis of the number of FAs. Notably, they are consistent with those concerning cellular rigidity: the number of FAs in SMc and Mfib is not altered by CNTs, while Fib grown on CNTs present a larger number of FAs, presumably connected to a more effective transmission of load from the nanostructured substrate to the cell. Interestingly, if we consider cell areas in both conditions (on tCNTs and on glass controls) we can see that any change is appreciable between Fib and SMc on both substrates while, from the other hand, a significant reduction in cell surface is appreciable in the case of Mfib grown on tCNTs (see Figure 30B). As consequence of that, we evaluated the density of FAs for every cell phenotype when interfaced or not to tCNTs (Figure 30C). FAs densities were calculated dividing the total number of FAs by the effective cell area (Mfib are characterized by areas in generally larger than Fib areas and, when developed above CNTs, generally smaller than when interfaced on glass). Also in this case an extremely significant overexpression of FAs is observable on Fib while, from the other hand, Mfib when interfaced to CNTs shown just a slight, not significant, increase in FAs density. As consequence of such data, we can see that Fib cell phenotypes are strongly influenced in its mechanobiology by the underneath CNT carpet while Mfib cells not. Anyhow, in order to understand the exact mechanism subtending to this peculiar behavior more experiments are necessary.

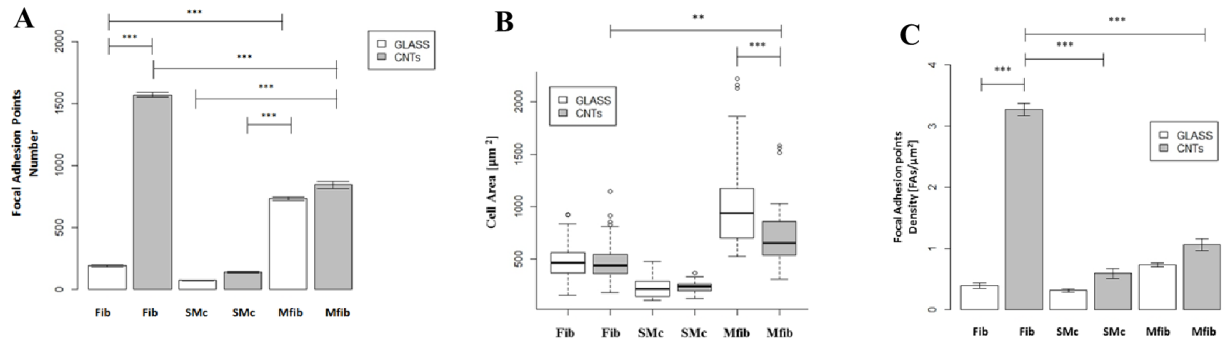

Figure 30. (A) Number of focal adhesion points, (B) cell total area, (C) resulting density of focal adhesion points (t-Test, p<0.05=*, p<0.01=**, p<0.001=***).

4.3.3 Discussion

As already stated, calcific aortic valve disease (CAVD) is strongly related to significant changes in ECM organization, composition and mechanical properties [65,80]. Based on the fundamental role of ECM in this context, in this section of my thesis research, I focused my interest toward the design and subsequent realization of a suitable ECM-like (bio)scaffold capable of providing additional insights into the cells-ECM interaction taking place inside the aortic valve. My final goal would be to develop new strategies to slow down, or even prevent, CAVD progression. To pursue this aim, I took advantage of CNT films ability to mimic ECM morphology [20]. In particular, I have developed a novel approach to grow carbon nanotubes via CCVD directly on fused-silica glass slides, allowing to obtaining transparent MWCNTs, and not opaque films as using the 'standard' procedure (see Methods and section 4.1 of this chapter) [48]. Thanks to the optical transparency of my novel CNTs-based scaffold we had the possibility, for the first time, to simultaneously perform an immunofluorescence assay, to characterize VICs morphology and phenotype, and AFM force spectroscopy analysis, to determine cellular stiffness on a large portion of cells when interfaced, or not, to my carbon-based nanostructured substrates. I have here reported that CNTs-decorated glass surfaces, well-resembling the natural ECM, resulted not toxic for cells and, additionally, a good adhesion of VICs on such substrates was observed. It was reported that VIC phenotypic transition from fibroblasts to myofibroblasts, occurring in pathological conditions, are strongly interconnected to ECM composition and morphology, in particular between organized and disordered fibrillary structures [65]. Therefore, we have investigated if these phenotypic variations could occur in VICs when cultured on tCNTs mat. By considering the specific shape of cells, we have identified three different morphologies, subsequently correlated to three cell phenotype: myofibroblasts (Mfib), fibroblasts (Fib) and smooth muscles cells (SMc). Our data revealed that, on CNTs, the percentage of myofibroblasts, correlated with VICs differentiation into osteoblastic-like cells (diseased phenotype), is significantly reduced with respect to glass controls (respectively 10% of total on CNTs and 50% on glass). Interestingly, the percentages of Mfib observed on glass and CNTs substrates are comparable to those reported in literature for pathological and healthy valves, respectively, suggesting that our CNT substrates can provide a physiological and 'safe' environment for VICs, probably thanks to their ECM-mimicking features and/or mechanical properties. In order to evaluate the effect of our ECM-like nanomaterial on VIC mechanical properties, we have exploited the advantage offered by the optical transparency of our CNTs-

based substrates to clearly visualize and discriminate fluorescent cells simultaneously with a mechanobiological characterization by means of the AFM mounted above an inverted microscope. Following this very novel approach, we have noticed that fibroblasts cultured on CNTs seem to be stiffer than those grown on glass slides, while myofibroblasts, surprisingly, show a lower stiffness if compared to the control cultures. This observation could be ascribed to a different effect of CNTs on VICs phenotypes (fibroblasts and myofibroblasts) depending on their specific shape, finding a partial confirmation in literature [79].

References

[1] V. Lovat, D. Pantarotto, L. Lagostena, B. Cacciari, M. Grandolfo, M. Righi, G. Spalluto, M. Prato, L. Ballerini *Carbon nanotube substrates boost neuronal electrical signaling*. Nano Lett., 5, 1107 – 1110, 2005.

[2] A. Fabbro, A. Villari, J. Laishram, D. Scaini, F. M. Toma, A. Turco, M. Prato, L. Ballerini, *Spinal cord explants use carbon nanotube interfaces to enhance neurite outgrowth and to fortify synaptic inputs*. ACS Nano., 6 : 2041–2055, 2012.

[3] G. Cellot, E. Cilia, S. Cipollone, V. Rancic, A. Sucapane, S. Giordani, L. Gambazzi, H. Markram, M. Grandolfo, D. Scaini, F. Gelain, L. Casalis, M. Prato, M. Giugliano, L. Ballerini *Carbon nanotubes might improve neuronal performance by favouring electrical shortcuts*. Nat. Nanotechnol, 4, 126 – 133, 2009.

[4] A. Mazzatenta, M. Giugliano, S. Campidelli, L. Gambazzi, L. Businaro, H. Markram, M. Prato, L. Ballerini, *Interfacing neurons with carbon nanotubes: electrical signal transfer and synaptic stimulation in cultured brain circuits*. J. Neurosci., 27, 6931 – 6936, 2007.

[5] K. A. Shah, B. A. T. *Synthesis of Carbon Nanotubes by Catalytic Chemical Vapour Deposition: A Review on Carbon Sources, Catalysts and Substrates*. Mater. Sci. Semicond. Process. *41*, 67–82, 2016.

[6] M. Kumar, Y. Ando, *Chemical Vapor Deposition of Carbon Nanotubes: A Review on Growth Mechanism and Mass Production*. Journal of Nanoscience and Nanotechnology, 10, 3739–3758, 2010.

[7] P. M. Parthangal, R. E. Cavicchi, M. R. Zachariah, *A generic process of growing aligned carbon nanotube arrays on metal and metal alloys*, Nanotechnology, *18*, 185605, 2007.

[8] M. K. Lai, N. M. Mohamed, K. M. Begam, *The Role of Al_2O_3 Buffer Layer in the Growth of Aligned CNTs*, Advanced Materials Research, *32*, 29, 2008.

[9] A. M. Cassell, J. A. Raymakers, J. Kong, H. Dai, *Large Scale CVD Synthesis of Single-Walled Carbon* Nanotubes, J. Phys. Chem., *103*, 6484, 1999.

[10] D. E. Resasco, W. E. Alvarez, F. Pompeo, L. Balzano, J. E. Herrera, B. Kitiyanan, A. Borgna, *A Scalable Process for Production of Single-walled Carbon Nanotubes (SWNTs) by Catalytic Disproportionation of CO on a Solid Catalyst*, J. Nanopart. Res., *4*, 131, 2002.

[11] T. Ng, B. Chen, J. E. Koehne, A. M. Cassell, J. Li, J. Han, M. Meyyappan, *Growth of Carbon Nanotubes: A Combinatorial Method To Study the Effects of Catalysts and Underlayers***,** J. Phys. Chem., *107*, 8484, 2003.

[12] M. Horibe, M. Nihei, D. Kondo, A. Kawabata, Y. Awano, *Carbon Nanotube Growth Technologies Using Tantalum Barrier Layer for Future ULSIs with Cu/Low-k Interconnect* Processes, Jpn. J. Appl. Phys., *44*, 5309, 2005.

[13] J. M. Wen, J. W. Evans, M. C. Bartelt, J. W. Burnett, P. A. Thiel, *Coarsening Mechanisms in a Metal Film: From Cluster Diffusion to Vacancy* Ripening, Phys. ReV. Lett., *76*, 652, 1996.

[14] E. Jiran, C. V. J. Thompson, *Capillary instabilities in thin films*, Electron. Mater. *19*, 1153, 1990.

[15] P. R. Gadkari, A. P. Warren, R. M. Todi, R. V. Petrova, K. R. Coffey, *Comparison of the agglomeration behavior of thin metallic films on SiO_2,* J. Vac. Sci. Technol. A, 23, 1152, 2005.

[16] Y. M. Li, W. Kim, Y. G. Zhang, M. Rolandi, D. W. Wang, H. J. Dai, *Growth of Single-Walled Carbon Nanotubes from Discrete Catalytic Nanoparticles of Various* Sizes, J. Phys. Chem. B, 105, 11424, 2001.

[17] J. F. Colomer, B. Ruelle, N. Moreau, S. Lucas, R. Snyders, T. Godfroid, C. Navio, C. Bittencourt, *Vertically aligned carbon nanotubes: Synthesis and atomic oxygen functionalization,* Surf. Coat. Technol., *205*, 592, 2011.

[18] L. Zhang, Z. Li, Y. Tan, G. Lolli, N. Sakulchaicharoen, F. G. Requejo, B. S. Mun, D. E. Resasco, *Influence of a Top Crust of Entangled Nanotubes on the Structure of Vertically Aligned Forests of Single-Walled Carbon Nanotubes***,** Chem. Mater., 18, 5624, 2006

[19] A. Ramirez, C. Royo, N. Latorre, R. Mallada, R. M. Tiggelaar, A. Monzón. *Unraveling the growth of vertically aligned multiwalled carbon nanotubes by chemical vapor deposition*. Materials Research Express 1.4, 2015.

[20] T. Dvir, B.P. Timko, D.S. Kohane, R. Langer, *Nanotechnological strategies for engineering complex tissues,* Nat. Nanotechnol. 6, 13–22, 2011.

[21] J. H. Lehman M. Terrones, E. Mansfield, K. E. Hurst, V. Meunier, *Evaluating the characteristics of multiwall carbon nanotubes*, Carbon 49.8, pp. 2581–2602. 2011.

[22] C. J. Lee, J. Park, Y. Huh, L. Yong, *Temperature Effect on the Growth of Carbon Nanotubes Using Thermal Chemical Vapor* Deposition, J. Chem. Phys. Lett., 343, 33, 2001.

[23] J. C. Charlier, *Defects in Carbon Nanotubes*, Acc. Chem. Res, 35, 1063, 2002.

[24] A. Jorio, M. A. Pimenta, A. G. Souza, R. Saito, G. Dresselhaus, M. S. Dresselhaus, *Characterizing carbon nanotube samples with resonance Raman scattering*. New J Phys, 5: 139.1–17, 2003.

[25] M. S. Dresselhaus, P. C. Eklund, *Phonons in carbon nanotubes*, Adv. Phys., 49, 705, 2000

[26] P. C. Eklund, J. M. Holden, R. A. Jishi, *Vibrational modes of carbon nanotubes; Spectroscopy and theory*, Carbon, 33, 959, 1995

[27] M. S. Dresselhaus, G. Dresselhausb, R. Saitoc , A. Joriod, *Raman spectroscopy of carbon nanotubes*, Physics Reports 409, 47–99, 2005.

[28] R. Saito, A. Jorio, A. G. Souza Filho, G. Dresselhaus, M. S. Dresselhaus, M. A. Pimenta, *Probing phonon dispersion relations of graphite by double resonance Raman scattering*. Phys Rev Lett; 88(2):027401-1–4, 2001.

[29] S. Osswald, E. Flahaut , H. Ye , Y. Gogotsi, *Elimination of D-band in Raman spectra of double-wall carbon nanotubes by oxidation*, Chemical Physics Letters, 402:422-427, 2005.

[30] E. F. Antunes, A.O. Lobo, E.J. Corat, V.J. Trava-Airoldi, *Influence of diameter in the Raman spectra of aligned multi-walled carbon nanotubes*, Carbon, , 45, 913, 2007

[31] W. Li, H. Zhang, C. Wang, Y. Zhang, L. Xu, K. Zhu, *Raman characterization of aligned carbon nanotubes produced by thermal decomposition of hydrocarbon* vapor, Appl. Phys. Lett., 70, 2684–2686, 1997.

[32] R. A. DiLeo, B. J. Landi, R. P. Raffaelle, *Purity assessment of multiwalled carbon nanotubes by Raman spectroscopy***,** J. Appl. Phys., 101, 064307, 2007.

[33] R. Saito, A. Gruneis, G. G. Samsonidze, V. W. Brar, G. Dresselhaus, M. S. Dresselhaus, A. Jorio, L. G. Can, C. Fantini, M. A. Pimenta, A. G. Souza Filho, *Double resonance Raman spectroscopy of single-wall carbon nanotubes*, New J. Phys. 5, 157, 2003.

[34] K. K. Kim, J. S. Park, S. J. Kim, H. Z. Geng, K. H. An, C. M. Yang, K. Sato, R. Saito, Y. H. Lee. *Dependence of Raman Spectra G′ Band Intensity on Metallicity of Single-Wall Carbon Nanotubes*, Phys Rev B, 76 (20) :205426-1–8, 2007.

[35] C. Mattevi, C. T. Wirth, S. Hofmann, R. Blume, M. Cantoro, C. Ducati, C. Cepek, A. Knop-Gericke, S. Milne, C. Castellarin-Cudia, S. Dolafi, A. Goldoni, R. Schloegl, J. Robert-son, In-*situ X-ray Photoelectron Spectroscopy Study of Catalyst−Support*

*Interactions and Growth of Carbon Nanotube Forests***,** J. Phys. Chem. C, 112, 12207, 2008

[36] M Scardamaglia, M Amati, B Llorente, P Mudimela, J-F Colomer, J Ghijsen, C Ewels, R Snyders, L Gregoratti, C Bittencourt, Nitrogen ion casting on vertically aligned carbon nanotubes: Tip and sidewall chemical modification, Carbon, 77, 319-328, 2014.

[37] T. I. T. Okpalugo, P. Papakonstantinou, H. Murphy, J. McLaughlin, N. M. D. Brown, *High resolution XPS characterization of chemical functionalised MWCNTs and SWCNTs*, Carbon, 43, 153, 2005.

[38] H. M. Saavedra, T. J. Mullen, P. Zhang, D. C Dewey, S. A. Claridge, P. S Weiss, *Hybrid strategies in nanolithography*, Rep. Prog. Phys., 73, 036501, 2010.

[39] P. Galvan-Garcia, E. W. Keefer, F. Yang, M. Zhang, S. Fang, A. A. Zakhidov, R. H. Baughman, M. I. Romero. *Robust cell migration and neuronal growth on pristine carbon nanotube sheets and yarns*. J. Biomater. Sci. Polym. Ed, 18, 1245 – 1261, 2007.

[40] A. Béduer, F. Seichepine, E. Flahaut, I. Loubinoux, L. Vaysse, C. Vieu, *Elucidation of the role of carbon nanotube patterns on the development of cultured neuronal cells*, Langmuir 28, 17363–17371, 2012.

[41] T. J Webster, M. C. Waid, J. L. McKenzie, Price, R., J. U. Ejiofor, *Carbon nanofibers/nanotubes for neural and orthopedic applications*. Nanotechnology, 15, 48-54, 2004.

[42] G. Cellot, F. M. Toma, Z. K. Varley, J. Laishram, A. Villari, M. Quintana, S. Cipollone, M. Prato, L. Ballerini, *Carbon nanotube scaffolds tune synaptic strength in cultured neural circuits: novel frontiers in nanomaterial-tissue interactions*, J Neurosci, *31*, 12945, 2011.

[43] S. Bosi, R. Rauti, J. Laishram, A. Turco, D. Lonardoni, T. Nieus, M. Prato, D. Scaini, L. Ballerini, *From 2D to 3D: novel nanostructured scaffolds to investigate signalling in reconstructed neuronal networks. Scientific Reports*, Sci Rep, *5*, 9562, 2015.

[44] R. Rauti, N. Lozano, V. León, D. Scaini, M. Musto, I. Rago, F. P. Ulloa Severino, A. Fabbro, L. Casalis, E. Vázquez, K. Kostarelos, M. Prato, L. Ballerini, *Graphene Oxide Nanosheets Reshape Synaptic Function in Cultured Brain Networks*, ACS Nano. *10*, 4459, 2016.

[45] D. Avossa, M. D. Rosato-Siri, F. Mazzarol, L. Ballerini, *Spinal circuits formation: a study of developmentally regulated markers in organotypic cultures of embryonic mouse spinal cord***,** Neuroscience, 122, 391, 2003**.**

[46] M.F. L. De Volder, S. H. Tawfick, R. H. Baughman, A. J. Hart, *Carbon Nanotubes: Present and Future Commercial Applications,* Science, 339, 535 (2013).

[47] M. Tang, Q. Song, N. Li, Z. Jiang, R. Huang, G. Cheng, *Enhancement of electrical signaling in neural networks on graphene films*, Biomaterials 34, 6402-6411, 2013.

[48] J. V. Anguita , D. C. Cox , M. Ahmad , Y. Y. Tan , J. Allam ,S. R. P. Silva, *Highly Transmissive Carbon Nanotube Forests Grown at Low Substrate Temperature*, Adv. Funct. Mater., 23, 5502–5509, 2013.

[49]J. W. Finnie, P.C. Blumbergs, *Traumatic Brain Injury*. Vet Pathol (2002) 39:679–689.

[50] K. A. Shah, B. A. Tali, *Synthesis of Carbon Nanotubes by Catalytic Chemical Vapour Deposition: A Review on Carbon Sources, Catalysts and Substrates*. Mater. Sci. Semicond. Process. 41, 67–82, 2016.

[51] F. B.Michaelis,, R. S. Weatherup, B. C. Bayer, M. C. D. Bock, H. Sugime, S. Caneva, J. Robertson, J. J. Baumberg,; S. Hofmann, *Co-Catalytic Absorption Layers for Controlled Laser-Induced Chemical Vapor Deposition of Carbon Nanotubes*. ACS Appl. Mater. Interfaces, *6*, 4025–4032, 2014.

[52] M. Morassutto, R.M. Tiggelaara, M.A. Smithers, G.E. Gardeniersa. *Vertically aligned carbon nanotube field emitter arrays with Ohmic base contact to silicon by Fe-catalyzed chemical vapor deposition*. Materials Today Communications 7, 89-100, 2016.

[53] S. Costa, E. Borowiak-Palen, M. Kruszyńska, A. Bachmatiuk, R. J. Kaleńczuk, *Characterization of Carbon Nanotubes by Raman Spectroscopy*. Mater. Sci., 26, 2008.

[54] E.F. Antunes, A.O. Lobo, E.J. Corat, V. J. T.-A. *Influence of Diameter in the Raman Spectra of Aligned Multi-Walled Carbon Nanotubes*. *Carbon N. Y.* **2007**, *45*, 913–921.

[55] L. G. Bulusheva, A. V. Okotrub, I. A. Kinloch,; I. P. Asanov, A. G. Kurenya, A. G. Kudashov, X. Chen,; H. Song, *Effect of Nitrogen Doping on Raman Spectra of Multi-Walled Carbon Nanotubes*. Phys. status solidi **2008**, *245*, 1971–1974.

[56] D. A. Long, *Raman Spectroscopy*; McGraw-Hill International Book Company, 1977.

[57] N. P. G. Roeges, *A Guide to the Complete Interpretation of Infrared Spectra of Organic Structures*; Wiley, 1994.

[58] S. Usmani, E. R. Aurand, M. Medelin, A. Fabbro, D. Scaini, J. Laishram, F. B. Rosselli, A. Ansuini, D.Zoccolan, M. Scarselli, M. De Crescenzi, S. Bosi, M. Prato, L. Ballerini. *3D meshes of carbon nanotubes guide functional reconnection of segregated spinal explants*. Sci Adv. 2(7): e1600087, 2016.

[59] S. Jacobson, E. M. Marcus. *Neuroanatomy for the Neuroscientist*. Springer New York, 2008.

[60] J. V. Perederiy, G. L. Westbroo, *Structural plasticity in the dentate gyrus - revisiting a classic injury model*. Front Neural Circuits 7: 17, 2013.

[61] M. Vuksic, D. Del Turco, A. Vlachos, G. Schuldt, C. M. Müller, G. Schneider, T. Deller, *Unilateral entorhinal denervation leads to long-lasting dendritic alterations of mouse hippocampal granule cells*. Exp Neurol. 230(2):176-85, 2011.

[62] A. Vlachos, D. Becker, P. Jedlicka, R. Winkels, J. Roeper, T. Deller. *Entorhinal denervation induces homeostatic synaptic scaling of excitatory postsynapses of dentate granule cells in mouse organotypic slice cultures*. PLoS One. 7(3):e32883, 2012.

[63] S. Raspopovic, M. Capogrosso, F.M. Petrini, M. Bonizzato, J. Rigosa, G. Di Pino, J. Carpaneto, M. Controzzi, T. Boretius, E. Fernandez, G. Granata, C. M. Oddo, L. Citi, A. L. Ciancio, C. Cipriani, M.C. Carrozza, W. Jensen, E. Guglielmelli, T. Stieglitz, P.M. Rossini, S. Micera, *Restoring natural sensory feedback in real-time bidirectional hand prostheses*, Sci Transl Med. 5 (6), 222, 2014.

[64] M. Capogrosso, T. Milekovic, D. Borton, F. Wagner, E.M. Moraud, J.B. Mignardot, N. Buse, J. Gandar, Q. Barraud, D. Xing, E. Rey, S. Duis, Y. Jianzhong, W.K. Ko, Q. Li, P. Detemple, T. Denison, S. Micera, E. Bezard, J. Bloch, G. Courtine, *A brain-spine interface alleviating gait deficits after spinal cord injury in primates*. Nature, 539, 284-8, 2016.

[65] H. Ma, A. R. Killaars, Frank W. Del Rio, Chun Yang, Kristi S. Anseth, *Myofibroblastic activation of valvular interstitial cells is modulated by spatial variations in matrix elasticity and its organization*, Biomaterials 131, 131e144. 2017.

[66] A. J. Engler, S. Sen, H. L. Sweeney, D. E. Discher, *Matrix Elasticity Directs Stem Cell Lineage Specification*. Cell, *126*, 677–689, 2006.

[67] S. Hinderer, J. Seifert, M. Votteler, N. Shen, J. Rheinlaender, T. E. Schäffer, K. Schenke-Layland, *Engineering of a bio-functionalized hybrid off-the-shelf heart valve*, Biomaterials 35, 2130e2139, 2014.

[68] A. Patlolla, B. Knighten, P. Tchounwou. *Multi-walled carbon nanotubes induce cytotoxicity, genotoxicity and apoptosis in normal human dermal fibroblast cells*. Ethn. Dis, 20, 1 – 17, 2010.

[69] C. Poland, R. Duffin, I. Kinloch, A. Maynard, W. H. Wallace, A. Seaton, V. Stone, S. Brown, W. Mac Nee, K. Donaldson. *Carbon nanotubes introduced into the abdominal cavity of mice show asbestos-like pathogenicity in a pilot study*. Nat. Nanotechnol, 3, 423 – 428, 2008.

[70] Z. Li, T. Hulderman, R. Salmen, R. Chapman, S. S. Leonard, S. H. Young, A. Shvedova, M. I. Luster, P. P. Simeonova. *Cardiovascular effects of pulmonary exposure to single-wall carbon nanotubes*. Environmental Health Perspectives, 115, 377-382, 2007.

[71] V. Martinelli, G. Cellot, F. M. Toma, C. S. Long, J. H. Caldwell, L. Zentilin et al., *Carbon nanotubes promote growth and spontaneous electrical activity in cultured cardiac myocytes*. Nano Lett. 12, 1831–1838, 2012.

[72] J. Baum, H. S. Duffy, *Fibroblasts and Myofibroblasts: What Are We Talking About?* J. Cardiovasc. Pharmacol., 57, 376–379, 2011.

[73] N. M. Rajamannan, M. Subramaniam, D. Rickard, S. R. Stock, J. Donovan, M. Springett, T. Orszulak, D. A. Fullerton, A. J. Tajik, R. O. Bonow, *T. Spelsberg, Human Aortic Valve Calcification Is Associated with an Osteoblast Phenotype*. Circulation, 107, 2181–2184, 2003.

[74] M. S. Sacks, W. David Merryma, D. E. Schmidt, *On the biomechanics of heart valve function.* J Biomechic, 42:1804 –1824, 2009.

[75] W. L. K. Chen, C. A. Simmons, *Lessons from (Patho)physiological Tissue Stiffness and Their Implications for Drug Screening, Drug Delivery and Regenerative Medicine.* Adv. Drug Deliv. Rev, 63, 269–276, 2011.

[76] J. H. Chen, W. L. K. Chen, K. L. Sider, C. Y. Y. Yip, C. A. Simmons, *β-Catenin Mediates Mechanically Regulated, Transforming Growth Factor-β1-Induced Myofibroblast Differentiation of Aortic Valve Interstitial Cells.* Arterioscler. Thromb. Vasc. Biol, 31, 590–597, 2011.

[77] H. Liu, Y. Sun, C. A. Simmons, *Determination of Local and Global Elastic Moduli of Valve Interstitial Cells Cultured on Soft Substrates*. J. Biomech, 46, 1967–1971, 2013.

[78] C. Yang, F. W. DelRio, H. Ma, A. R. Killaars, L. P. Basta, K. A. Kyburz, K. S. Anseth, *Spatially Patterned Matrix Elasticity Directs Stem Cell Fate*. Proc. Natl. Acad. Sci., 113, E4439–E4445, 2016.

[79] J. H. Chen, C. A. Simmons, *Cell-Matrix Interactions in the Pathobiology of Calcific Aortic Valve Disease: Critical Roles for Matricellular, Matricrine, and Matrix Mechanics Cues*. Circ. Res., 108, 1510–1524, 2011.

Conclusions

During the last decade, the interest on biocompatible materials promoting tissue regeneration and/or functional restoration has significantly increased. Such scaffolds should emulate as close as possible the complex extracellular and physiological environment of the tissue areas where they are programmed to be placed as well as display suitable mechanical, chemical and biological properties. Among the most promising materials in this context, carbon nanotubes (CNTs) show distinctive physico-chemical properties and satisfy biomimetic requirements, representing therefore an excellent candidate.

Here, we adopted an interdisciplinary approach to investigate the possible structural and functional changes occurring in a novel nano-biohybrid system, consisting of neurons developed on CNTs carpets which are synthesized via catalytic chemical vapor deposition (CCVD) technique on supporting silicon surfaces. We revealed, for the first time on these novel substrates, a potentiation in electrical activity of neuronal cells cultured above them. Our results are consistent with previous works, indicating that CNTs produced by CCVD behave at cellular level in a way similar to what observed in literature for drop-casted substrates, offering the added value of synthesis tunability to realize complex 2D CNTs patterns or 3D CNTs architectures. Since classical cell investigation techniques, exploited to study cell matrix interaction, are based on optical transmission through the sample, we adapted our CNT synthesis method to a transparent substrate, as fused silica, obtaining transparent CNT (tCNT) mats with CNT lengths about 10 μm. Thanks to such strategy, by performing electrophysiology and immunocytochemistry experiments, we demonstrated the ability of our novel tCNT substrate to induce the same synaptic potentiation in hippocampal cultures previously verified on ‘standard’ drop-casted CNT films. Moreover, we assessed the impact of our tCNTs-based scaffolds on the entorhinal cortex and hippocampal complex using organotypical cultures (EHCs): we adopted this model to investigate if regenerative processes take place between complex components and to evaluate the capability of nanotubes to enhance axonal sprouting and fibers regeneration. Morphological and electrophysiological measurements performed on these neuro-nano hybrid structures revealed the astonish ability of our nanomaterial to determine a successful reconnection and functional cross talk between the lesioned brain tissue area.

Overall, the presented results provide novel insights about the promising interaction between carbon nanotubes and neural networks and open the possibility of adopting our novel, cost-

effective, fabrication approach to design new scaffolds able to modulate/tune cell performances *in vitro*. Our CNTs-based scaffolds could be considered as promising tools for the development of a new generation of implantable neural interfaces and prosthetic devices for medical neuroscience.

Furthermore, we interfaced our novel tCNTs scaffold with porcine valve interstitial cells (pVICs), the predominant constituent of aortic valve, in order to investigate and try to modulate cellular properties *via* such nanomaterial. We observed that CNTs induce a significant reduction in the percentage of myofibroblasts, correlated with VICs differentiation into osteoblastic-like cells (disease associated phenotype), with respect to flat glass controls. Interestingly, since the amount of myofibroblasts on glass and CNTs substrates are comparable to those reported in literature for pathological and healthy valves, respectively, we can speculate that our CNT substrates can provide a physiological and 'safe' environment for VICs, probably thanks to their ECM-mimicking features and/or mechanical properties. Our CNTs-based substrates, thanks to their ECM-like semblance, could be exploited to expand our knowledge about the interaction between cells and ECM taking place inside the aortic valve, paving the way to reduce, or even prevent, CAVD progression, since such disease is strongly related to variations in ECM morphology and mechanical properties.

Appendix

1 The third dimension

In order to identify a reliable strategy to control/tune cellular behavior, representing the groundwork for developing novel bio-implants, it is important to mimic as much as possible the real physiological condition of cells inside the tissue they want to mimic or replace. The native *in vivo* cellular organization is three-dimensional, consequently 2D scaffolding structures fail in reproducing the complex and dynamic environment of native tissues [1]. Consequently, if a reliable cellular organization is the final objective, three-dimensional (3D) scaffolds have to be developed and adopted as matrices resembling the structure, chemistry and signaling framework of the natural cellular matter [2]. Moving toward this goal, I have worked on the design and realization of various 3D bio-constructs made of different materials, including carbon nanotubes and polymers. In the following sections, all of these different attempts to realize innovative cellular scaffolds are briefly described. Presented data must be considered as preliminary, since a thorough study is still ongoing. Nevertheless, this part of my research is noteworthy, since preliminary results are extremely encouraging.

1.1 A step towards 3D: layer-by-layer procedure

In order to create a perfectly controlled CNTs-based 3D system, lithographic and etching techniques have been exploited [3]. As described previously (see Methods), I have patterned, and then etched silicon nitride (Si_3N_4) membranes, with the final purpose to create circular through-holes with dimensions comparable with those of cells. Subsequently, a thin catalyst layer of Fe (2–5 nm in thickness) was deposited on the underneath suspended membrane and, finally, CNTs growth was carried out by CCVD. These membranes could be stacked one on the top of another with the possibility to control and modulate the porosity and the properties of each layer employed. In this way, cells can pass through the holes and extend themselves for the entire thickness of this well-controlled 3D system (Figure 1).

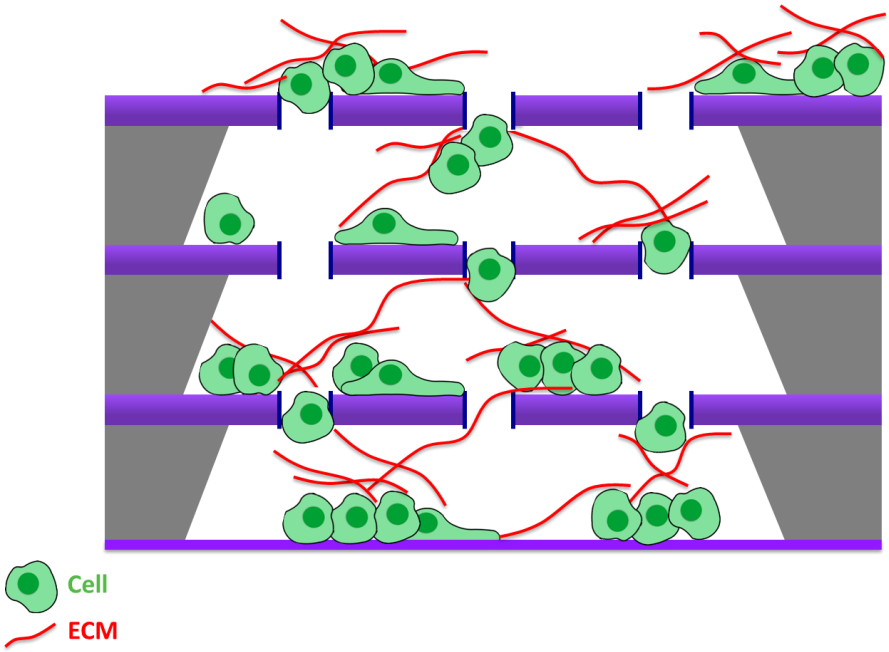

Figure 1. Schematic overview of our strategy: patterned, and then etched silicon nitride (Si_3N_4) membranes, characterized by circular through-holes with dimensions comparable with those of cells. They could be stacked one on the top of another, with the final purpose to create a well-controlled 3D constructs.

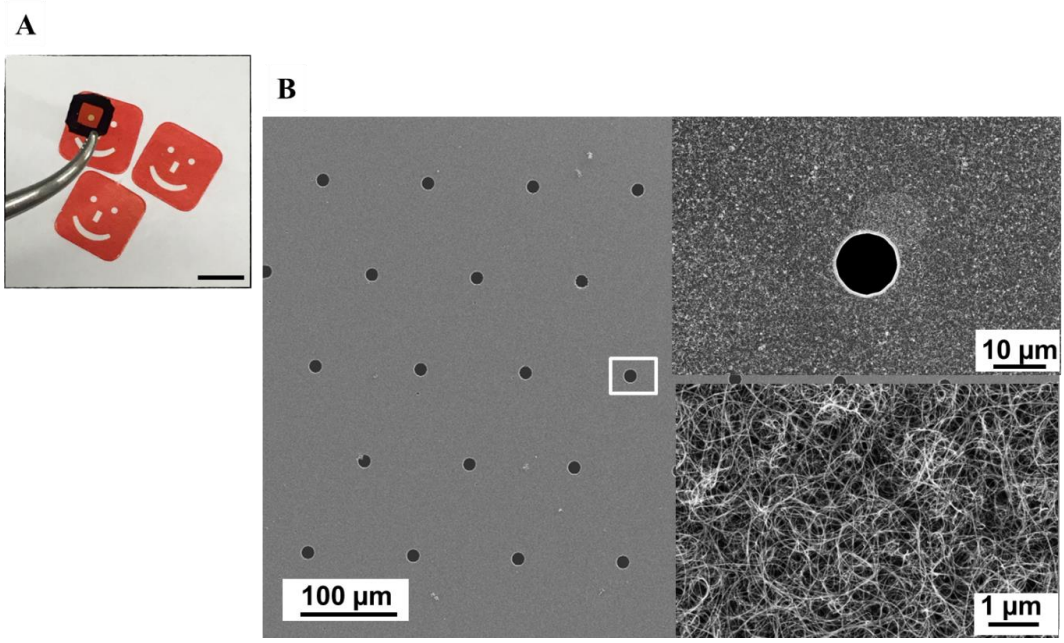

Figure 2. (A) Representative optical images of silicon nitride (Si_3N_4) membranes on which were grown CNTs by CCVD clearly showing their optical transparency (scale bar: 8 mm); (B) SEM images of CNTs synthesized on Si_3N_4 substrates.

Figure 2 reveals the successful growth of CNTs mat on Si_3N_4 membranes together with the optical transparency of these substrates (despite the presence of nanotubes). This later aspect, as already stated, represents a powerful tool for all the techniques and methods which require 'to see' through the specimens. So far, I have realized only one layer of this scaffold. Next step will be the stacking of more membranes in order to investigate how cells adjust in a well-controlled 3D scaffold.

1.2 Fe foam

As previously introduced, in order to realize a porous 3D CNTs-based architecture, we have adopted a sintered Fe sponge acting simultaneously as catalyst and template (see Methods). The general idea of our strategy was to obtain free-standing MWCNTs foam by taking advantage of a Fe foam-templated/catalyzed CVD technique followed by the subsequent etching of the entire metallic template living, as result, a free-standing 3D porous scaffold of entangled CNTs: the negative replica of our starting Fe mold [4]. Figure 3 shows the general morphology of the as-sintered mold (See Methods) constituted by grains characterized by very smooth surfaces. Since in CVD-assisted CNTs synthesis, nanotubes formation occurred from the iron nanoparticles, which act as 'catalytic template' for the subsequent CNTs growth [5], we have performed an acid attack (NITAL solution) in order to increase the surface roughness of the metallic mold (See Methods) and 'activate' its catalytic ability. Two different NITAL treatments were tested on the Fe-mold (30 and 60 seconds), leading to a significant increase of grains surface roughness with respect to the un-treated counterpart (Figure 4, A-C). In particular, the better condition leading to the higher grain surface roughness was obtained after a NITAL treatment of 60 seconds (Figure 4-C). Subsequently, the specimen was mounted on the heating element inside the CVD chamber for the subsequent CNTs growth step (see Methods). Figure 5 clearly highlights that CNTs was almost absent in the un-treated sample (Figure 5, A); while nanotubes can be observed above the Fe mold surfaces subjected to the acid treatment with no significant differences between the two tested conditions (30 and 60 sec) (Figure 5, B and C). At the same time, it is possible to appreciate the low uniformity of nanotubes grown on the as-sintered metallic foam. I have supposed that the presence of a thin oxide layer on the Fe surfaces had prevented the uniform growth of the CNTs together with the relative low temperature employed (730 °C).

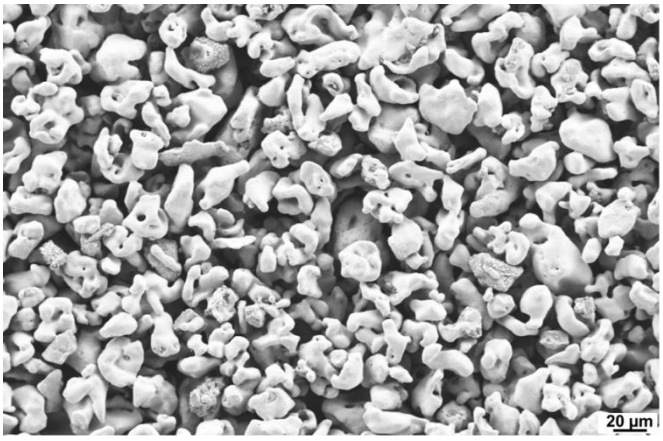

Figure 3. SEM micrograph showing the general morphology of the as-sintered Fe foam.

Figure 4. SEM micrographs showing the surface morphology of the as-sintered un-treated (A), treated with a NITAL attack of 30 sec (B) and 60 sec (C) Fe foam.

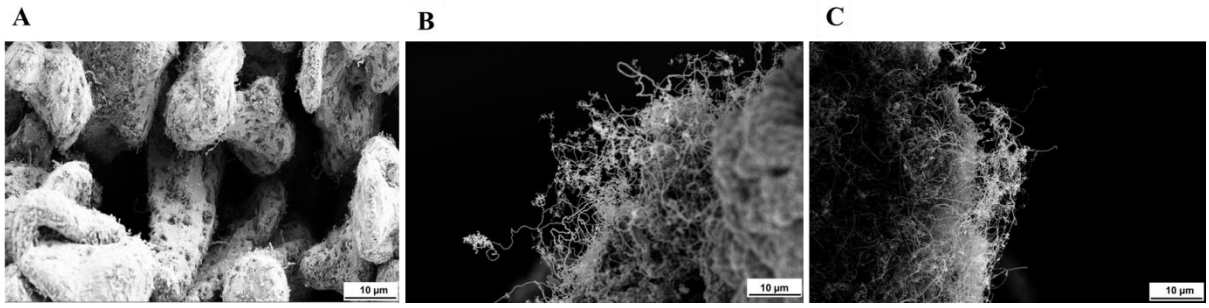

Figure 5. SEM micrographs displaying CNTs grown by CCVD directly on the un-treated (A), treated with a NITAL attack of 30 sec (B) and 60 sec (C) Fe foam.

An increase in the duration and temperature of the thermal annealing treatment could probably enhance the yield of CNTs over the Fe foam, because it may lead to a thermal equilibrium, before the CNT growth, for the whole sample. Unfortunately, the current

available experimental set-up did not allow us to test these synthesis conditions, because of the restriction imposed by the heating element inside the CVD chamber which is able to tolerate a maximum temperature of about 750 °C for no extended periods, before the rupture caused by the thermal fatigue. Although this result is very promising in order to realize a self-standing 3D CNTs-based scaffold, further studies are required to optimize this synthesis process.

1.3 PDMS-based 3D porous scaffolds

We have realized 3D porous scaffolds made of PDMS (Sylgard® 184 and Sylgard® 527) via a modified solvent casting particulate leaching approach (SCPL) [5]. Starting sugar molds were prepared moistening sugar grains of calibrated dimensions with the following solution: 100%, 90%, 80%, 70% decane/water, 100% and 80% 2-butanol/water, and a mixture of 50% decane/2-butanol (See Methods for more details). Reason for these attempts originates from our first experiments, aimed at obtaining a porous elastomeric scaffold, were just water was used as solvent. This experimental condition unfortunately has led to an extremely compact structure, due to pronounced glucose dissolution: in this condition the complete infiltration of PDMS was extremely difficult. Therefore, in order to preserve as much as possible the micro-structured template made of glucose, giving rise to a final porosity compatible with cell dimensions and favorable to percolation, we have though to use the non-polar solvent decane in the process mixing it with water at different concentrations (from 5 to 30% in weigh). This resulted as well in an increase of pore interconnectivity. The experimental parameter that we have adopted to evaluate the pore interconnectivity was the leaching time (see Methods): higher leaching rate is an indicator of a better interconnectivity inside the scaffold. A halving in such parameter was observed, for example, in sugar molds produced by using 70% decane/water as wetting solution when compared to those realized starting from sugar wetted using just pure decane (from two days to less than one day). This leaching time is consistent with values observed in literature for similar approach [6-7]. No significant differences were, instead, observed in both leaching time and microstructure for the other tested conditions, except for the microporous scaffold obtained using a mixture of 50% decane/ 2-butanol for which the leaching time was reduced to 7 hours of bath sonication. Figure 6 shows SEM micrographs of our porous elastomeric 3D scaffolds obtained by employing a mixture of 50% decane/2-butanol, pointing out the uniform micro-structuration present in all the analyzed samples and the absence of bulky PDMS regions.

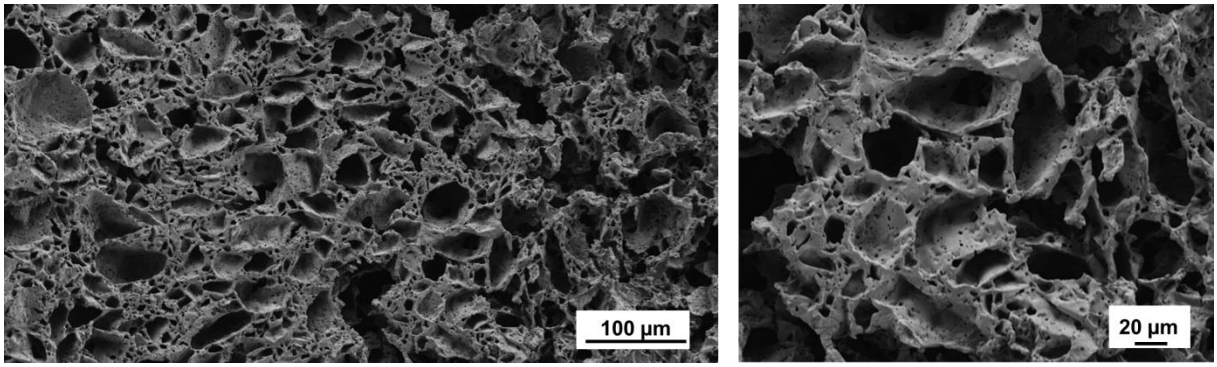

Figure 6. SEM micrographs, acquired at different magnifications, of 3D porous elastomeric scaffolds obtained starting from a mixture of 50% decane/2-butanol.

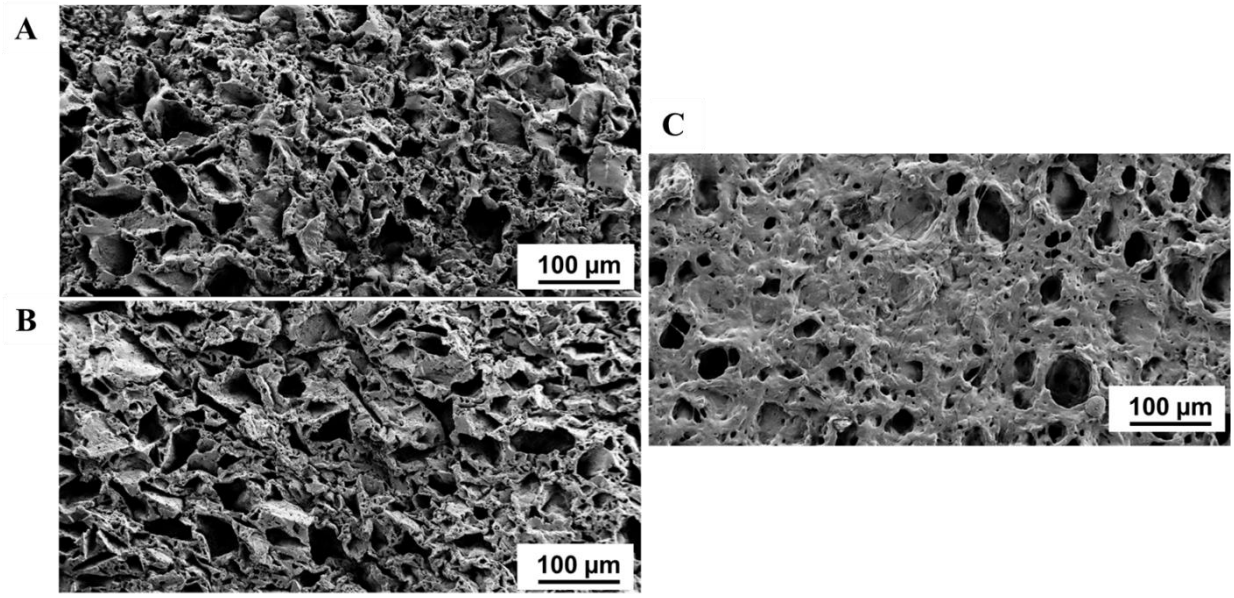

Figure 7. SEM micrographs of 3D porous elastomeric scaffolds obtained starting from decane and with different PDMS Sylgard® 184 and Sylgard® 527 ratios: (A) 3:1, (B) 1:3 and (C) 1:5.

Moreover, in order to tune the mechanical properties of the realized PDMS-based structures, we have blended together elastomers with different stiffness (see Methods). In particular, we have adopted 3 different blending conditions of Sylgard® 184 (elastic modulus of about: 1.72 MPa) and Sylgard® 527 (elastic modulus of about: 5 kPa): 3:1, 1:3 and 1:5, respectively. Figure 7 points out a more definite porous structure for scaffolds obtained with blending ratios of 3:1 and 1:3 (Figure 7-A and 7-B) with respect to 1:5 samples (Figure 7C), ascribable to the low mechanical properties of Sylgard® 527 PDMS. At the same time, it is possible to note also a bending of the side walls for both 3:1 and 1:3 constructs, indicating a partial collapse of these two structures. We retain that with an optimization of both the drying

process, by employing a critical point dryer, and the slicing procedure, by opportunely setting the velocity together with the oscillation frequency of the micro-tome cutting blade, these issues could be overcome.

1.4 Compression Test

We have collected, via uniaxial loading tests, the elastic modulus of both bulk and porous PDMS formulations for all the tested conditions (i.e. blending of Sylgard® 184 and Sylgard® 527 or Sylgard® 184 alone). A significant reduction of the mechanical properties, in terms of elastic modulus, was observed for the porous scaffolds (up to 80%) with respect to the bulk formulations [8] (Figure 8). The elastic modulus values of the analyzed elastomeric constructs were 0.3 MPa for the porous scaffold made by the stiffer elastomer (Sylgard® 184 alone) and 5 kPa for the softer elastomeric composition (1:5 Sylgard® 184 to Sylgard® 527 ratio). Due to the restricted number of samples tested, these values have to be considered as preliminary result. At the same time, the possibility to tune the mechanical properties of a (bio)scaffold opens new scenarios in the perspective to control the material/cell interaction and thus the biological response in a 3D frame.

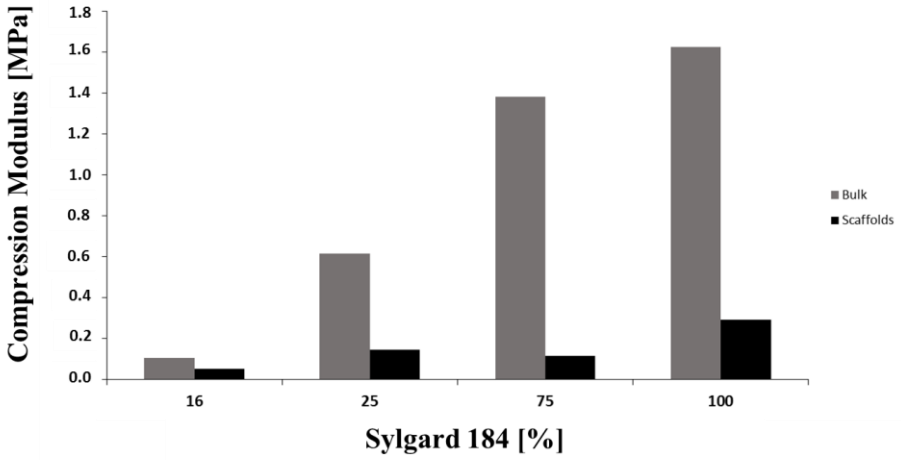

Figure 8. Compression modulus values of both bulk and porous PDMS formulations for all the tested conditions

1.5 Cotton candy sugar

The major challenge in the field of 3D scaffolds remains the difficulty to sustain cells metabolically active when they colonize a large 3D scaffold or, the entire thickness of an extremely thick construct. To prevent this problem it is crucial to provide to the cells sufficient exchange of soluble compounds (e.g., oxygen, nutrients and, of course, waste products removal) further than a few hundred microns from the scaffold/media interface. To achieve this result, I engineered 3D artificial vascular systems, potentially enabling active perfusion of large scaffolds [9]. I proceeded toward the problem with a novel easy and inexpensive strategy, starting from cotton candy sugar as mold template and following the same procedure described for the porous PDMS-based scaffolds previously described (see Methods). X-ray microcomputed tomography on these elastomeric constructs was performed (see Methods) in order to analyze the general architecture and characterize the pores size distribution of the final elastomeric scaffold.

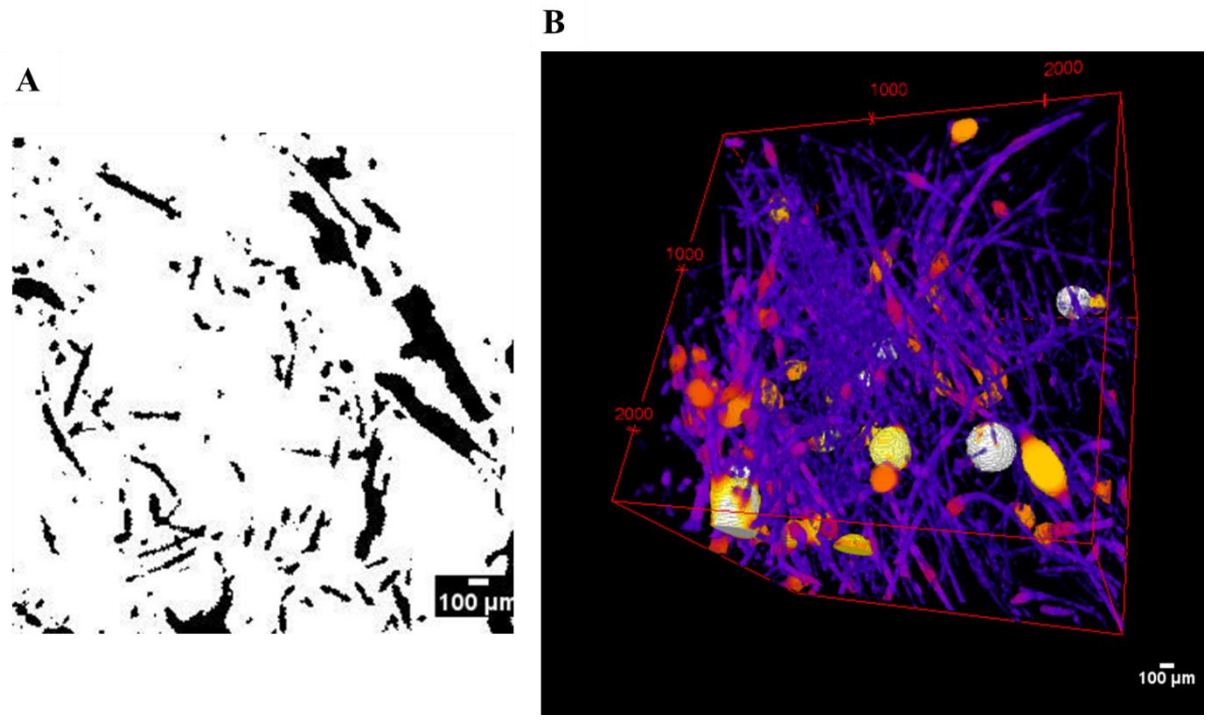

Figure 9. (A) Typical single slice image and (B) 3D slice reconstruction of PDMS scaffolds obtained via X-ray microcomputed tomography. In (A) brighter voxels are assigned to the more absorbing phase and the darker voxels to the less absorbing one, PDMS and air in our case. In (B) the color (form blue to white) is related to pore size: the larger the pore size the more the color approaches the white.

Image elaboration involved the individuation of the different materials constituting the specimen (in our case PDMS and air) through the analysis of the voxel color intensity: white voxels are assigned to the more absorbing phase and the dark voxels to the less absorbing one. Figure 9 reveals the aspect of a reconstructed single slice and the final 3D reconstruction obtained for our scaffolds *via* X-Ray microcomputed tomography. Overall, the scaffold consists of both pores and channels characterized by diameters spanning from 30 to 200 μm. Despite further studies are necessary to optimize the architecture of the scaffold, the size distribution of pores and channels together with their interconnectivity, our simple and low-cost approach is very encouraging in the perspective to realize a 3D perfusable microvascular system embedded inside a porous 3D scaffold to keep cells alive and functional, thus giving rise to an artificial cell/scaffold construct better representing the real physiological condition of the native tissues.

References

[1] K. L. Schmeichel, M. J. Bissell, *Modeling tissue-specific signaling and organ function in three dimensions*, J Cell Sci, 116 (Part 12), 2377–2388, 2003.

[2] R. Edmondson, J. J. Broglie, A. F. Adcock, L. Yang, *Three-Dimensional Cell Culture Systems and Their Applications in Drug Discovery and Cell-Based Biosensors*, ASSAY and Drug Development Technologies, 12 (4), 2014.

[3] C. Py, M. W. Denhoff, M. Martina, R. Monette, T. Comas, T. Ahuja, D. Martinez, S. Wingar, J. Caballero,S. Laframboise, J. Mielke, A. Bogdanov, C. Luk, N. Syed, G. Mealing, *A Novel Silicon Patch-Clamp Chip Permits High-Fidelity Recording of Ion Channel Activity From Functionally Defined Neurons*, Biotechnology and Bioengineering, Vol. 107, No. 4, November 1, 2010.

[4] R. Paul, V. Etacheri, V. G. Pol, J. Huc, T. S. Fisher *Highly porous three-dimensional carbon nanotube foam as a freestanding anode for a lithium-ion battery*, RSC Adv., 6, 79734, 2016.

[5] J. W.Han, B.Kim, J.Li, M. Meyyappan, *Flexible, compressible, hydrophobic, floatable, and conductive carbon nanotube-polymer sponge.* Applied physics letters 102, 0519031–0519034, 2013.

[6] J. Si, Z. Cui, P. Xie, L.Song, Q. Wang, Q. Liu, C. Li. *Characterization of 3D elastic porous polydimethylsiloxane (PDMS) cell scaffolds fabricated by VARTM and particle leaching*. Journal of Applied Polymer Science 133.4, 42909-42918, 2016.

[7] E. Pedraza, A.C. Brady, C.A. Fraker, C.L. Stabler. *Synthesis of macroporous poly(dimethylsiloxane) scaffolds for tissue engineering applications*. Journal of Biomaterials, Science, Polymer, 24 (9), 1041–1056, 2013.

[8] R. N. Palchesko, L. Zhang, Y. Sun, A. W. Feinberg, *Development of Polydimethylsiloxane Substrates with Tunable Elastic Modulus to Study Cell Mechanobiology in Muscle and Nerve*. PLoS ONE7(2012), e51499, 2012

[9] J. B. Lee, X. Wang, S. Faley, B. Baer, D.A. Balikov, H. Sung, L.M. Bellan, *Development of 3D microvascular networks within gelatin hydrogels using thermoresponsive sacrificial microfibers*, Adv Healthc Mater., 5(7), 781–785, 2016.